

Alma Mater Studiorum – Università di Bologna

**DOTTORATO DI RICERCA IN
CHIMICA**

Ciclo XXVIII

Settore Concorsuale di afferenza: 03 / B1

Settore Scientifico disciplinare: CHIM / 03

**LUMINESCENT AND PHOTO-RESPONSIVE
GOLD NANOPARTICLES FOR
BIO-APPLICATIONS**

Presentata da: Andrea Cantelli

Coordinatore Dottorato

Prof. Aldo Roda

Relatore

Prof. Marco Montalti

Esame finale anno 2016

Luminescent and photo-responsive Gold nanoparticles for bio-applications

Contents

Abbreviations and symbols	VI
1 Introduction	1
1.1 Emerging of luminescent Gold nanotechnology	1
1.2 Molecular photo-responsive actuators and their combination with nanomaterials	2
1.3 Aims of the study	4
1.4 Gold nanoclusters and ultra-small Gold nanoparticles	6
1.5 Nomenclature	6
1.6 Synthesis	7
1.6.1 <i>Gold salts reduction in presence of thiols, amines or phosphines</i>	9
1.6.2 <i>Macromolecule templated synthesis</i>	12
1.7 Most commonly used characterization methods for GNCs	16
1.8 Origin of luminescence	18
1.8.1 <i>Core structural arrangements and size confinement quantum effects</i>	18
1.8.2 <i>Surface effects</i>	23
1.8.3 <i>Auophilic interactions and aggregation induced emission (AIE)</i>	26
1.8.4 <i>Combined effects</i>	28
1.9 Magic numbers, superatoms, electronic shells closure effects and some theoretical models	33
1.9.1 <i>Jellium model</i>	34
1.9.2 <i>Jellium model limits and Superatom complex model</i>	37

1.9.3	<i>Superatom model limits, Super Valence Bond and superatom-network models</i>	38
1.9.4	<i>Kinetic factors and models limits</i>	41
1.10	Stability of thiols protected gold clusters	42
1.11	XPS and HRTEM Lattice spacing determination of thiols protected GNCs	44
1.12	Applications in imaging and theranostic	47
2	Apparent effect of nanomaterials on photoisomerization....	65
2.1	Introduction	65
2.2	Materials	66
2.3	Photoirradiation experiments	66
2.4	Conventional approach to PI rate determination	67
2.5	Results and discussion	72
2.6	Conclusions	82
3	Effects on photoisomerization caused by interactions with nanomaterials	83
3.1	Introduction	83
3.2	Materials	84
3.3	Photoirradiation and NMR experiments	84
3.4	Results and discussion	86
3.5	Conclusions	108
4	Photoswitchable NIR emitting Gold nanoparticles	109
4.1	Introduction	109
4.2	Materials and experimental procedures	110
4.3	Results and discussion	110
4.4	Conclusions	120

5	Silica nanoparticles gathering luminescent glutathione protected Gold nanoclusters	121
5.1	Introduction	121
5.2	Materials	123
5.3	Methods	123
5.4	Results and discussion	124
5.5	Conclusions	146
6	Conclusions	148
7	Experimental section.....	150
7.1	Synthesis of 8-(4-((4-methoxyphenyl)diazenyl) phenoxy)octyl-thiol	150
7.1.1	<i>Synthesis of 4-((4-methoxyphenyl)diazenyl)phenol</i>	150
7.1.2	<i>Synthesis 1-(4-((8-bromooctyl)oxy)phenyl)-2-(4-methoxyphenyl)diazene</i>	151
7.1.3	<i>Synthesis of 8-(4-((4-methoxyphenyl)diazenyl) phenoxy)octyl)thiol</i>	151
7.2	Synthesis of azobenzene derivative functionalized GNPs (<i>tA-GNPs</i>)	153
7.3	Instrumentations and techniques	154

Abbreviations and symbols

11-MUA = 11-mercaptoundecanoic acid
A549 cell line = lung carcinoma cell line from human
antiSAIgG = antistaphylococcal immunoglobulin
Au-Ft = Au-Ferritine
BSA = bovine serum albumin
Caco-2 cell line = human colorectal carcinoma cell line
COS-1 cell line = african green monkey kidney cell line
CPP = cell penetrating peptides
Cy5 = cyanine-5
DPA = D-penicillamine
 ε = molar absorption coefficient
 Φ = photoisomerization quantum yield
FA = folic acid
Ft = ferritine
GES-1 cell line = gastric epithelial cell line
GNCs = gold nanoclusters
GS = glutathione without its thiolic proton
GSH = glutathione
HeLa cell line = human epitheloid cervix carcinoma cell line
HepG2 cell line = human hepatoma cell line
HEK 293 cell line = human Embryonic Kidney cell line
His = histidine
HOAc = acetic acid
HMDA = hexamethylenediamine
ICP-MS = inductively coupled plasma mass spectrometry
ISC = inter system crossing
LA = lipoic Acid
LCC = Lewis lung carcinoma
LMCT = ligand to metal charge transfer
LMMCT = ligand-to-metal-metal charge transfer
LO2 cell line = immortal hepatic cell line

MCF7 cell line = human breast adenocarcinoma cell line
MGC-803 cell line = human gastric cancer cell line
MRSA = Methicillin-resistant Staphylococcus Bacteria
MSSA = Methicillin-sensitive Staphylococcus Bacteria
MTT = 3-[4,5-dimethylthiazol-2-yl]-2,5-diphenyltetrazoliumbromide
MUA = 11-mercaptoundecanoic acid
NC = nanocluster
NP = nanoparticle
P = poly(maleic anhydride-alt-1-octadecene) (Mn=30 000–50 000)
PDI = Polydispersity index
p.i. = post injection
PEG = poly(ethylene glycol)
PEGDA = O,O_-bis(2-aminopropyl)poly(propylene glycol)-block-(polyethylene-glycol)-block-poly(propylene glycol) (Mr=600; PEG-diamine)
PPIX = protoporphyrin IX
PS = aluminium phthalocyanine
QY = quantum yield
TEOS = tetraethyl orthosilicate
X = halogen atom

1 Introduction

1.1 Emerging of luminescent Gold nanotechnology

Ever since antiquity Gold has been the noble element par excellence. Artefacts made of this metal can retain their property and their brilliant luster for thousands of years without deterioration.¹ It is still called “noble” because it reacts in few rare cases, so that only after the 1300 mankind found chemical ways to dissolve it.² In the 1857 Michael Faraday reported for the first time a synthesis of gold colloids from dissolved gold chloride defining them “fine particles” resulting in a “beautiful ruby fluid”. Faraday immediately understood that those particles were smaller than the visible light wavelengths, which is comprised between 450 and 650 nm,³ but the technology of that period was not sufficient to characterize them on the nanometers scale. Recent advances allow scientists to manipulate matter at the atomic level and nanosized materials are today globally produced, characterized and integrated in markets. Science focusing on the matter that is structured in the order of less than 100nm⁴ is called nanotechnology, a recently well established field which offers new possibility to tackle unresolved issues and answer fundamental questions.⁵ In fact these materials possess very different properties compared to their bulk or molecular counterparts often overcoming them.⁴ In the last decades scientists managed to create materials particles so small to be made of just few atoms. Usually called “nanoclusters” they can be considered as a bridge between molecules and nanoparticles. Differently from larger particles, under certain sizes, these species start to be governed by molecular like quantum mechanics behaviours and their properties become quantized.⁶

Recent concerns about the potential toxicity of, at least, some categories of nanomaterials accelerated the research for highly biocompatible nanostructures. According to recent literature gold nanoclusters (GNCs) and small nanoparticles (GNPs) promise to combine low toxicity and interesting optical and electronic properties. Gold size reduction to few atoms or few nanometer units can lead to luminescent nanospecies that find application in several fields as sensing, optoelectronic, energy storing, imaging and catalysis.⁷

In particular this work focuses on GNCs whose luminescent properties are of interest in the fields of bio-medical imaging, theranostics, photo-controlled drug delivery and sensing. As main advantage, compared to other diagnostic approaches, fluorescence or more in general luminescence based techniques are poorly invasive. In order to exploit such attractive feature, the search of highly biocompatible contrast agents with spectral controllable features and good photostability is necessary. Gold nanoclusters (GNCs) based probes promise to merge all of these characteristics and their tunable emission from the visible to the NIR coincide with the ideal spectral window for *in-vivo* applications.

1.2 Molecular photo-responsive actuators and their combination with nanomaterials

Molecular photo-responsive actuators are those molecules capable of converting light into mechanical work. Azobenzene derivatives are the most studied class of photoactuators and they can convert electromagnetic radiation energy through a reaction called photoisomerization. In this photochemical reaction the absorption of a photon by a molecule can induce the switch of a molecule from the trans to the cis isomer, with the consequent motion of a molecule portion relatively to the other (Fig. 1)

The opposite reaction can be induced by a photon of another wavelength or by heat. When linked to other molecules, also of larger sizes, azobenzene photoswitching has been proven to be capable of inducing motion also on larger scales (Fig. 2).⁸ Together with the actuation of mechanical work at a molecular level, conformational switch of azobenzene derivatives determines changes in their chemical-physical properties. In the case of simple trans azobenzene, its dipole moment turns from 0 D to 3 D during its photoisomerization⁹ (Fig. 1). Changes of the photoswitcher chemical and conformational properties can be exploited for example to induce conformational changes in larger molecules.¹⁰

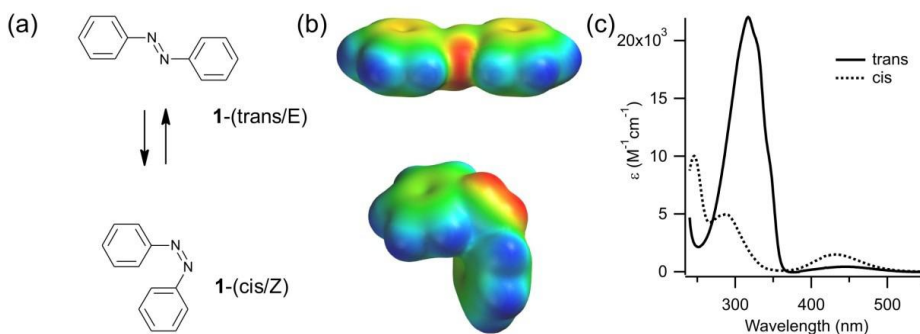


Fig. 1: (a and b) Structures of trans and cis isomers of azobenzene. Spacefilling models are coloured by electrostatic potential (red—negative to blue—positive). (c) Electronic absorption spectra of the trans and cis isomers of azobenzene dissolved in ethanol.¹¹

The same effect can be also used to control AB repartition between nanomaterials and their external environment, or vice versa to control the adsorption of drugs molecules onto azobenzene functionalized nanostructures. Photoswitchable dyes have often been combined to supramolecular nanostructures for several different purposes as to create photocontrollable nanomachines,^{12,13} phototunable membrane ions channels¹⁴ or devices for light triggered drug release.¹⁵

In this framework, photochemical properties of complex light driven systems combining photoactuators and nanomaterials arise increasing attentions.

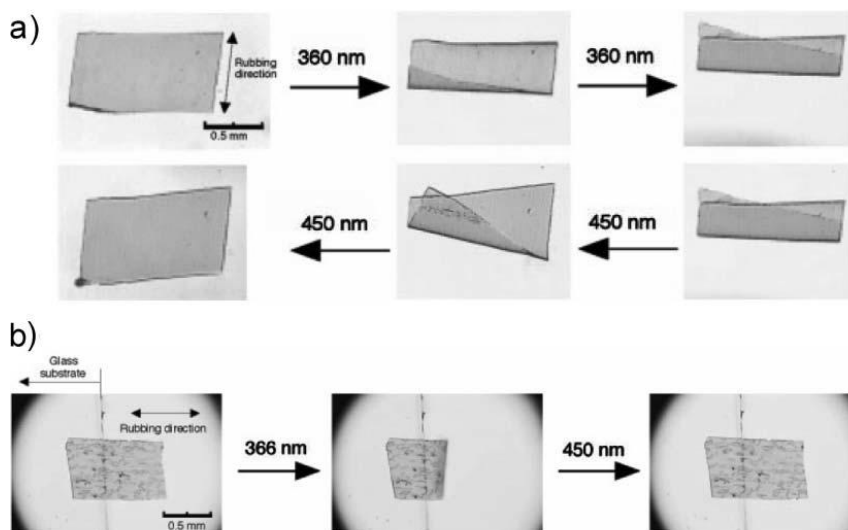


Fig. 2: a), b): Bending and unbending behaviour of azobenzene-containing materials upon irradiation.⁸

1.3 Aims of the study

This work mainly focus on the development of luminescent Gold NCs and NPs based probes for sensing, imaging, theranostics and photocontrolled drug delivery. Gold nanostructures have been combined with different photoactuators in order to fabricate light responsive nanomaterials and investigate their photochemical behaviour. The work described in Chapter 2 aimed at developing a convenient approach to precisely quantify the photoisomerization (PI) quantum yields (QY) of photoswitchable dyes in

presence of nanosized materials. In Chapter 3 and 4 this method has been applied to study GNPs effect on PI QYs of azobenzene (AB) derivatives, in two general families of systems. In the former, AB derivatives were covalently bound to the Gold's surfaces, while in the latter, partially water soluble AB molecules were simply adsorbed by repartition between the particles coating monolayers and the solvent.

In the last case, particles with different affinity for the photoswitcher have been employed to study its repartitions in different monolayers, to assess possible changes on photoisomerization efficiencies caused by its interactions with the nanoparticles, and to investigate the effects of photoisomerization on AB repartition (Chapter 3). A further objective of this work has been the investigation of potential effects on GNPs luminescence, resulting from the *trans* → *cis* photoisomerization of AB derivatives covalently linked on Gold surface. Moreover this work focused on the synthesis of a complex nanoprobe for NIR fluorescence imaging, composed by luminescent glutathione (GSH) functionalized GNCs encapsulated inside ≈20nm silica mesoporous nanoparticles, coated by a Poly Ethylene Glycol (PEG) layer. An extended NIR characterization of this system has been performed to assess the in-silica inclusion effects on gold clusters properties and, finally, the suitability of such probe for NIR luminescence imaging has been tested directly on living cells (Chapter 5).

In the next section, an introduction to luminescent GNCs and ultra-small GNPs will give an overview of the recent advances in their synthesis, characterization and bio-medical applications.

1.4 Gold nanoclusters and ultra-small Gold nanoparticles

The boundary between Gold nanoparticles and nanoclusters have been identified to be around 2.2 nm but this is still debated in literature.^{16,17}

1.5 Nomenclature

Gold nanoparticles is a commonly accepted and understood term which refer to gold colloids with sizes under 100 nm.¹⁷ In the case of Gold nanoclusters nomenclature appear more confused in literature. So far, there is no consensus on how to call small metallic clusters characterized by molecular properties and new names still continue to be proposed. Here we report a list of expressions that can be commonly found in literature referring to metallic clusters, with particular focus on the Gold one (Table 1).

This excess of new names is the first obstacle for the production of a coherent literature which is still a critical point of nanotechnology in general.

In this work, gold nanoclusters (GNCs) have been adopted as a common name, also if in some cases it has been used referring to particles with diameter slightly larger than 2.2 nm. Vice versa, in some cases, the term GNPs could have been used to indicate Gold structures which may be considered as GNCs. In every case the sizes of the species in question have always been explicated.

Name	Abbreviation
Au nanocluster/crystal	AuNCs
Au nanodots	AuND
Gold nanodots	GND
luminescent gold nanoclusters/crystal	FGNCs
Luminescent Au nanocluster/crystals	FANC
Luminescent Gold clusters	FGC
Nano-molecule	NM
Monolayer protected clusters ¹⁸	MPC
Ligand-stabilized clusters ¹⁸	LSC
Clusters ¹⁸	
Nanoclusters ¹⁸	NC
Quantum clusters ¹⁸	QC
Superatoms ¹⁸	
Faradaurates ¹⁸	
Luminescent nanoparticles ¹⁸	FN
Molecular clusters ¹⁸	MC
Atomic clusters ¹⁸	AC
Aspicule (proposed in ref. ¹⁸ as unifying name)	

Table 1: Common expressions referring to Gold or, in general, metallic clusters.

1.6 Synthesis

Gold clusters of few atoms, with interesting optical properties, were already known in 1987. Initially, they were prepared by sputtering Gold with an ions beam and studied in a noble gas matrix^{19,20}. Due to the difficulties related to the scale up of this synthesis method, solution techniques become the most employed for GNCs production.²¹

Information on their production and study in gas phase can be found, for example, in ref ⁶ and ²² but this text will focus only on solution methods. Depending on the synthesis strategy, GNCs and luminescent GNCs (LGNCs) can be obtained as species characterized by a controlled number of atoms and a precise structural formulas, or as populations of clusters with certain size distributions. Clusters having atomically controlled structures present several advantages, mainly in terms of results reproducibility and of possibility to design and characterize their properties. Clusters obtained as monodisperse populations, instead, present more issues in terms of results comparability, but their synthesis is generally easier if compared to the first case. Furthermore, as it will be described later, dispersity of cluster size, if limited to a narrow range, does not preclude their usefulness.

Most of the methods to synthesize GNCs in solution rely on three principal strategies: the reduction of a Gold salt in presence of thiols, the reduction of a gold salt in presence of macromolecular templating agents or the etching of larger gold particles and clusters.

The first two methods are bottom-up and they generally start from an Au(III) salt and employ a reductant to convert it into Au⁰. In this oxidation state, gold atoms have the strong tendency to aggregate, in order to generate Gold in its bulk form, which is one of the most stable and inert material known. According to the crystallization theory, the first step of the process is the nuclei generation in solution, followed by their growth. Molecules that efficiently bond to the clusters surface can passivate it, preventing the aggregation of different nuclei and the formation of bulk Gold. To this end, the best candidates are the molecules containing at least a functional group which can strongly bind the gold surface, such as thiols, phosphines,²¹ amines and citrates. The ability of preventing aggregation is generally proportional to the strength of the bond between the capping agent and the Gold surface. In this work we will focus only on thiols, because they provide the strongest affinity thus being the most employed and the easiest to work with.

1.6.1 Gold salts reduction in presence of thiols, amines or phosphines.

Almost all of the synthesis relying on the gold salt reduction strategy use HAuCl_4 as starting reagent, while some of them use (HAuX_4) . Different combinations of thiols, solvents and synthesis conditions have been largely explored and, in this text, we will describe just some of the works reported in literature as examples.^{23,24,25}

Typically the Gold salt is dissolved in water or in organic solvents and the subsequent addition of the thiol induces a partial reduction of Gold from Au^{3+} to Au^{1+} . This happens with the simultaneous formation of polymers composed by alternating thiolates and Au^{1+} atoms²⁶ (Fig. 3).

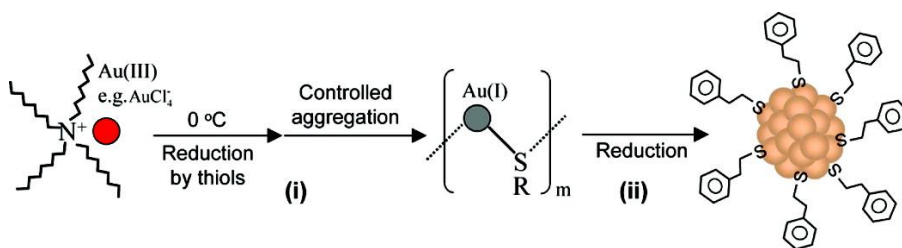


Fig. 3: GNCs formation reaction mechanism from ref²⁶.

These polymers are insoluble in water and some other solvents, and they can be solubilised by adjusting the pH of the solution, before the addition of the reducing agent.²⁷ After the addition of a reductant, Au^+ is converted to Au^0 and its complete aggregation is prevented by the excess of thiols present in solution. The reduction, typically with NaBH_4 , is generally performed under vigorous stirring, to achieve uniform cluster nucleation and growth. Reduction kinetic and size dispersion of the product strongly depend on the reaction conditions²⁷ and on the thiol employed. The importance of thiolate polymers formation step, in order to produce monodisperse or atomically controlled cluster, was already clear

in 1997.²⁸ For example, some years later, Zhu and co-workers found that performing this reaction step at 0°, with low stirring speed, allowed to better control the kinetic of thiolate polymers formation, leading to an higher yield of atomically controlled Au₂₅ clusters.²⁶ Successively, other methods have been developed to achieve high yields of atomically monodisperse Au₂₅ cluster, even at room temperature.²⁷ This account for the fact that parameters as pH, reduction kinetic,²⁷ concentrations and ligands molecular formula,²⁹ also play a major role in the control of clusters formation.

Despite most of the procedures use a strong reducing agent such as NaBH₄, in some cases, weak reducing agents have been shown to be effective as well.^{30,31,32} For example, Xu et al. developed a 15 minutes synthesis at 120°C in H₂O, where homocysteine is employed both as capping and reducing agent.³⁰ Similarly, histidine³¹ and glutathione³² were proven to be capable of performing both functions at the same time. Also Palmal and co-workers developed a synthesis where different thiols act as capping and weak reducing agents.³³ Despite their method does not provide control at the atomic level, with some modifications of the classical procedures, they have found a way to synthesize clusters with tuneable emission wavelengths from blue to NIR independently on most of the thiols employed. In order to explain their observations, the group also proposed a variant of the reaction mechanism which involve the disproportion of Au¹⁺ into Au⁰ and Au³⁺.³³

A strategy to control the surface chemistry of GNCs has been developed by Aldeek and co-workers. They developed a methodology to create clusters which can be functionalized with controllable amounts of different surface ligands. Their procedure allowed to synthesize circa 1,2 nm red emitting GNCs, with emission quantum yield (QY) between 10% and 14%, using different derivatives of lipoic acid. By simply varying the ratio between these derivatives it has been possible to obtain clusters with a controlled amount of different reactive groups, and which can be conjugated to other ligands by conventional protocols.³⁴

Most of synthetical routes lead to populations of clusters which are not atomically monodisperse, and clusters with different size can be separated

through two methods which are the most commonly employed. The simplest technique is the solvent precipitation where different proportions of solvent/non-solvent in the solution can induce the selective precipitation of cluster with different size ranges.³⁵ Another technique is Polyacrylamide gel electrophoresis (PAGE), which allow to separate GNCs³⁶ with atomic resolution as demonstrated for glutathione protected GNCs in the works of Negishi and co-workers.^{37,38,29} Findings and protocols developed in these works tremendously contributed to the understanding of Gold clusters chemistry and have been extensively applied in the following years. As confirmed also by Negishi et al., in a polydisperse sample of gold clusters, discrete structures with a well defined formula can be resolved. Some of these structures are characterized by particular numbers of Au atoms and have been identified to occur more frequently and in much higher concentration than the others (Fig. 17). Numbers corresponding to these structures have been called magic numbers³⁷ and the reasons and the implications of this phenomenon will be discussed in the “theoretical models” section.

1.6.2 Macromolecule templated synthesis

Luminescent GNCs have been synthesized employing as templating agents several kinds of macromolecules such as proteins, DNA, dendrimers and polymers. In this synthesis strategy the templating agent can act as nucleation center and play a role in the gold salt reduction and in clusters confinement.

1.6.2.1 Proteins

Xie and co-workers synthesized Bovine Serum Albumine (BSA) protected luminescent GNCs (Fig. 4), using BSA as templating and reducing agents, in water at pH ~12.³⁹ Their BSA protected Au₂₅ cluster emitted ~640 nm red light with an emission quantum yield (QY) of 6%. This green chemistry reaction has then been extensively reproduced and studied also by varying the synthesis parameters^{40,41,42} and employing different proteins as Insulin,⁴³ Lysozyme,^{44,45,46} Apo-Ferritin,³¹ Transferrine,⁴⁷ DNase 1,⁴⁸ RNase-A,⁴⁹ Pepsine,⁵⁰ cytochrome c, myoglobin, milk holo α -lactalbumin (type I), milk β -lactoglobulin and pancreas α -chymotrypsin.⁴² It has been shown that also Au₂₀⁴⁰ and Au₈⁴¹ clusters can be synthesized inside BSA, and that by adding a reductant and by changing pH, concentrations and temperature, clusters with different emission wavelength,⁵⁰ sizes and size distributions can be obtained with the same protein.^{41,50}

As some aminoacids contain gold coordinating functional groups, the first hypothesis on the reaction mechanism attributed to these aminoacids a role similar to thiols in the thiols-directed synthesis (briefly outlined in the previous section). In particular, the 35 cysteines of BSA have been thought to be fundamental for the stabilization of gold clusters.³⁹

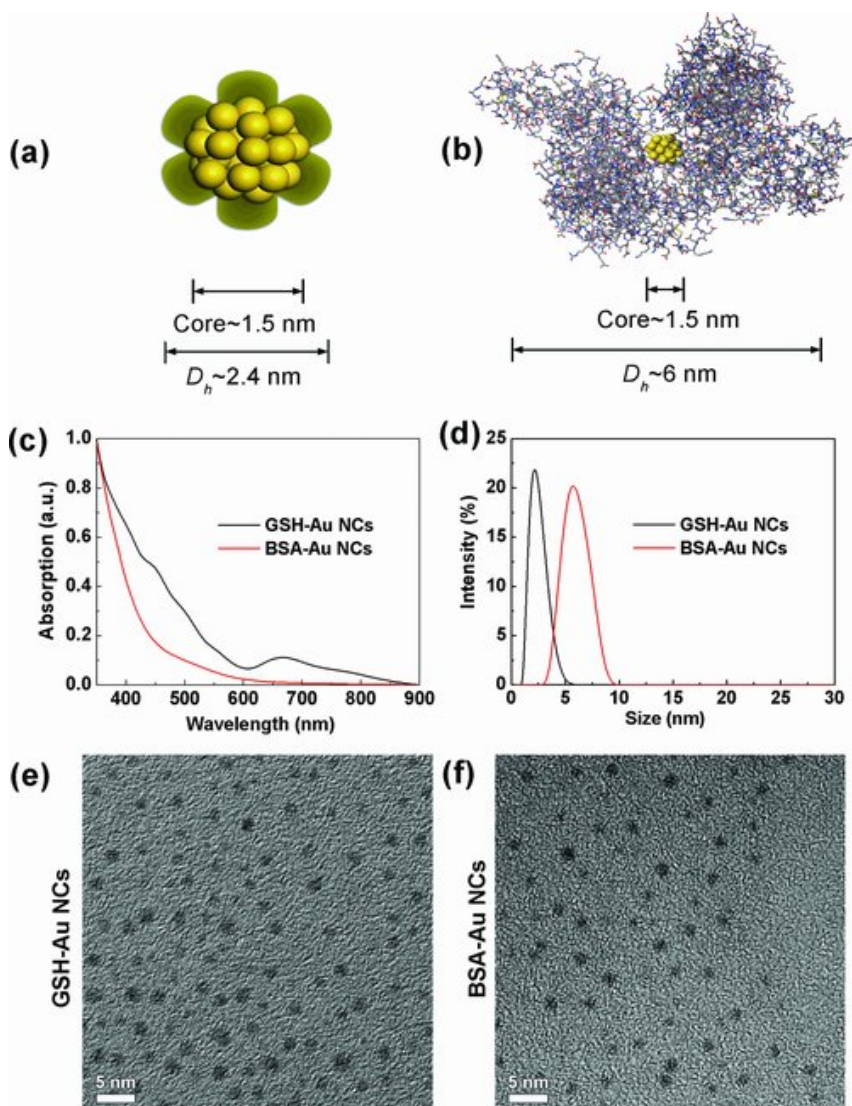


Fig. 4: Schematic illustration of the core-shell structure of a) GSH-Au₂₅ NCs and b) BSA-Au₂₅ NCs. c) UV-vis and d) DLS spectra of the as-prepared GSH-Au₂₅ NCs (black line) and BSA-Au₂₅ NCs (red line). Representative TEM images of the as-prepared e) GSH-Au₂₅ NCs and f) BSA-Au₂₅ NCs.⁵¹

Most of the proteins listed above, at basic pH, are capable of reducing gold to Au⁰, with no need for further reductants. This ability has been initially hypothesized to be due to the phenolic function of tyrosine, whose reducing power is enhanced above their pKa.³⁹

Successive studies also identified a role of histidine as reductant, showing that it can generate gold colloids also when mixed with HAuCl₄ in absence proteins.³¹ Other accurate investigations on protein templated mineralization by mass spectrometry, XPS, photoluminescence and X-ray crystallography substantially confirmed the first findings and provided further details on its mechanism and kinetic^{52,53} which, however, are still not completely understood. In another study by Volden et al. different proteins have been compared and it has been shown that the presence of thiolic aminoacids function is not necessary for protein templated GNCs formation and stabilization. This work findings led the group to propose a slightly different generalized reaction mechanism, in which anionic aminoacid residues have a fundamental function in stabilizing the formed nuclei, and in determining the influx of Au(III) ions from outside the protein.⁴² Interestingly, protein templated synthesis allow to produce GNCs with emission wavelengths spanning from blue to NIR,^{50,31} with QYs typically of some units percent, and in some cases above the 10%.

For application purposes it is important to notice that in some cases, during clusters synthesis, evidences of protein unfolding have been reported.⁴² Despite this, interestingly, some cluster-protecting proteins, have been demonstrated to retain their biological function both *in-vivo*^{43,31} and *in-vitro*.^{54,31} This is particularly important in nanomedicine and in bioimaging, where proteins may be exploited to address clusters toward specific targets and functions in organisms.

Mimicking nature's strategy, an attempt to rationally design a peptide sequence capable of templating atomically controlled luminescent GNCs has successfully been performed by de la Rica et al.⁵⁵

1.6.2.2 DNA, dendrimers and polymers

Poly(amidoamine) (PAMAM) dendrimers templated synthesis developed by Zheng et al.⁵⁶ Produces very highly luminescent GNCs. They have been reported to have the highest luminescence QY and, for this reason, they have generated a lot of excitement. After this report, other studies suggested that most of the light emission observed in ref.⁵⁶ can be attributed to chemical modifications of the dendrimers during the synthesis, instead of being generated from GNCs.^{57,58} However, successive papers, have clearly demonstrated the importance of gold clusters role in generating this luminescence: first, by demonstrating that the emission wavelength is correlated with the cluster mass following the Jellium free electron model^{59,60,61,62} and second, by showing that the emission intensity at a specific wavelength is directly proportional to the concentration of the GNC, which has the specific mass related to that particular wavelength (where concentrations have been quantified considering the intensity ESI MS peaks for each mass).^{60,61,62} Also with this synthesis strategy, reaction parameters can be varied to obtain PAMAM-GNCs composed by different number of atoms and tunable emissions from UV to NIR, with QY ranging from 70% to 10% respectively.⁶⁰

Another method to template and control GNCs growth rely on the use of polymers. For example, Beatriz Santiago González and co-workers, with an electrochemical reaction, synthesized Au₁, Au₂ and Au₃ GNCs protected by poly(*N*-vinylpyrrolidone) PVP, from a gold electrode and a PVP solution. This monodisperse cluster population emitted blue light with a luminescence QY of about 12,5% and showed a remarkable stability.⁶³ Li and co-workers used photoreduction to induce blue emitting Au₅ GNCs formation in solutions containing multidentate thioether-terminated polymers and gold salt. In the same study, they investigated the effects of changing polymer nature, concentration and structural parameters on NCs growth providing additional insights in understanding their luminescence mechanism. Blue emitting Au₈ GNC has also been obtained starting from larger GNPs by Duan and Nie.⁶⁴ They used Hyperbranched multivalent

polyethylenimine (PEI) which acted etching bigger colloids and templating the small Au₈ clusters, leading to a system with optical properties similar to the Au₈ cluster⁶⁴ of ref. ⁶⁰. For the synthesis of larger species, thiol-terminated PMMA based polymers have been shown to be useful templating agents. They allow the generation of Gold colloids ranging from large plasmonic gold nanoparticles to ~1 nm luminescent clusters.^{65,66,67}

In the last years, DNA has also been employed as templating agent for GNCs synthesis^{68,69,70,71} and recent advances led to the production of highly luminescent clusters with different color emissions⁷² and controlled number of atoms.⁷³

1.7 Most commonly used characterization methods for GNCs

In this work are reported only the most commonly employed techniques to characterize ligand protected GNCs from solution phase. For the analysis of these species, many other techniques can be applied. Here we report only the examples we encountered more often (Table 2).

Technique	Purpose
Dls	Measure of the hydrodynamic volume
Esi TOF MS	Determination of clusters molecular formula or mass distribution.
MALDI quadrupole time-of-flight (Q-TOF) MS	Determination of clusters molecular formula or mass distribution. ⁷⁴
ICP MS for evaluation in tissues	Quantitative determination of gold content in tissues <i>ex-vivo</i> , ^{24, 75} with a detection limit of 18 parts per trillion. ⁷⁶
XPS	Assessment of binding energies and gold atoms valence states. ^{40,30,77,74,31}
NMR	Assessment of ligands molecular formula, protonation state and conformation on cluster surface, and cluster magnetic properties.
UV-Vis spectrophotometry	Assessment of clusters optical properties and electronic structure [all ref.]
UV-Vis spectrofluorimetry	Assessment of clusters optical properties, electronic structure, and cluster concentration in tissues during the <i>in-vivo</i> trials
Single crystal X-ray crystallography	Structure determination ⁷⁸
Electronic microscopy (TEM, SEM)	Determination of size distributions, clusters morphology and clusters distribution in cells and in tissues <i>ex-vivo</i> .
EDX (energy dispersive X-ray spectroscopy)	Evaluation of cluster elemental composition and distribution in cells and tissues <i>ex-vivo</i> .
XAS (X-ray absorption spectroscopy) with its variants XANES ⁷⁴ and EXAFS ^{7c} .	Determination of some structural information on Gold and Sulphur atoms of the clusters ^{74,7c}

Table 2: List of the most commonly used techniques to characterize luminescent GNCs for bio-imaging applications.

1.8 Origin of luminescence

One of the most attractive properties of GNCs is luminescence, which find applications in several fields as sensing,⁷⁹ optoelectronic, energy storing, imaging and catalysis. They attracted great attention in the last years because of their superior photochemical stability⁷⁷ compared to common organic fluorophores. This is associated with satisfying emission QYs, long luminescence lifetimes,⁷⁷ interesting chiral and non-linear optical properties, large cross-section, tunable emissions and luminescence sensitivity to the environment. Moreover gold is characterized by good biocompatibility. Emission wavelength from gold nanoclusters can span from the UV to the IR with lifetimes in the range between tens of femtoseconds and tens of microseconds. Luminescence is thought to be generated through different mechanism and despite their photophysics is not completely understood, some general principles governing the phenomenon have been clarified. Emission from gold clusters has been identified to be due to three principal causes, which will be described more in details in the next paragraphs. The first is related to the core size confinement effect, that generate discrete electronic levels, which shapes and energies depend also on the core structure. The second cause are superficial phenomena, while the third are interactions generated by aggregation of gold species and aurophilic interactions.

1.8.1 Core structural arrangements and size confinement quantum effects

According to the free electron model, in bulk conductive metals valence electron are free to move in the lattice through the conduction band. As the size of the metal start to become comparable to the Fermi wavelength of an electron, until it diminish to few atoms, quantized electronic states and energy levels start to emerge^{60,61} (Fig. 7) and (Fig. 16).

As a consequence, a large part of the optical properties of these clusters are determined by electrons light induced transitions between these electronic states, analogously to what happen in molecules. For this reason, the computation of their geometric and electronic structure is crucial in characterizing their interaction with the electromagnetic radiations.^{6,7b,80} Some theoretical models and computational methods developed since today, to describe metal nanoclusters properties and structures, are described in the apposite section. Jellium model (JM) is one of the simplest that has been adopted to account for size confinement quantum effects on metal NCs photochemistry. Despite its simplicity it has a remarkable predicting power.^{6,60,61} It describe metal clusters valence electrons as confined in orbitals which have the same symmetry of the atomic ones (for spherical clusters) and that are filled according to similar roles (more details in the models section). JM predict the scaling of spherical metal NCs transitions energy, in function of their radius (Fig. 5), according to the simple relation

$$Eq. 1: \quad h\omega_0 \cong E_f N^{-\frac{1}{3}} = E_f r_s / R$$

where h is the Plank constant, ω_0 is the frequency of the transition, E_f is the Fermi Energy of bulk Gold, N is the number of metal atoms of the cluster, r_s is the Wigner-Seitz radius of the metal and R is the radii of the cluster.^{81,61} The model was initially developed for gas phase metal cluster but its efficacy has been demonstrated also in solution phase by Zheng, Dickson and coworkers, who demonstrated that PAMAM dendrimer encapsulated GNCs, with fewer than 40 atoms,^{60,61} have both excitation and emission energies scaling as $E_f/N^{(1/3)}$. JM also predict that when N increase, the energy level spacing decrease until it become smaller than k_bT (Fig. 7), allowing plasmonic collective motions of the electrons.^{60,61} Jellium constitute an excellent basic model also to describe larger particles plasmonic absorption and emission behavior, constituting a useful bridge to explain the transition between molecular-cluster and metallic optical properties.⁶⁰

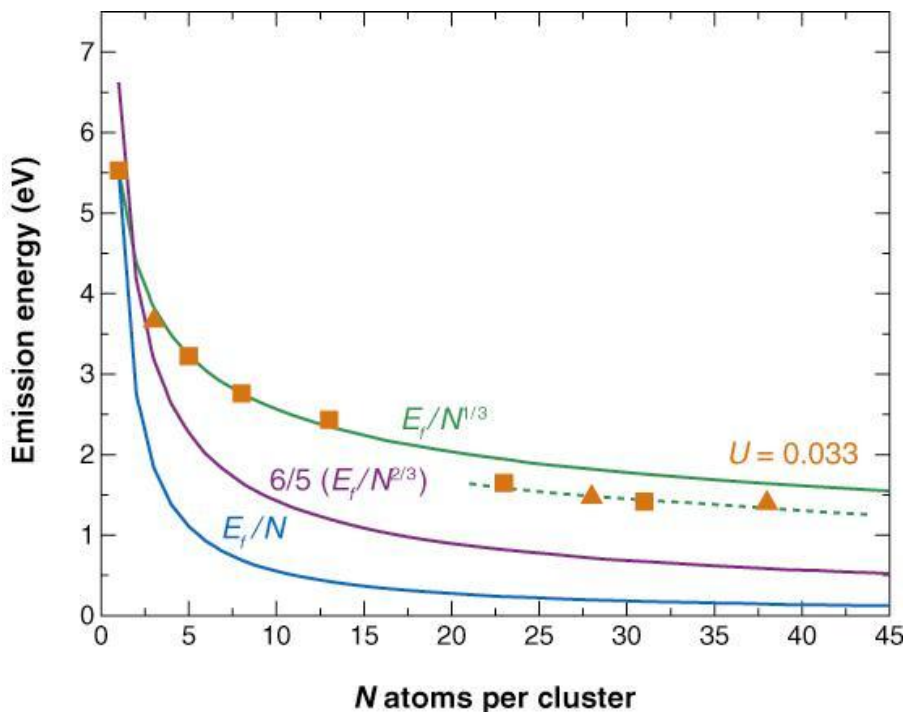


Fig. 5: Correlation of the number of atoms (N) per cluster with emission energy. Emission energy decreases with an increasing number of atoms. The correlation of emission energy with N is quantitatively fit with $E_{Fermi}/N^{1/3}$, as predicted by the jellium mode. When N equals 1, the energy of the valence electron is equal to the Fermi energy because the valence electron is at the highest occupied molecular orbital level. Emission energies of Au23 and Au31 exhibit slight deviations from the $E_{Fermi}/N^{1/3}$ scaling. Consistent with the narrow excitation and emission spectra, the potential confining the free electrons flattens slightly for Au23 and Au31, with the anharmonicity parameter $U = 0.033$. The experimental values for the emission energies of Au3, Au28, and Au38 are 3.66, 1.55, and 1.44 eV, respectively (represented by triangles), which are all consistent with the observed scaling relations. Kubo's predicted model E_f/N and the square-potential-box model $(6/5)E_f/N^{2/3}$ are also shown in the figure. Obviously these models cannot accurately fit the emission-energy scaling of the Au clusters.⁶¹

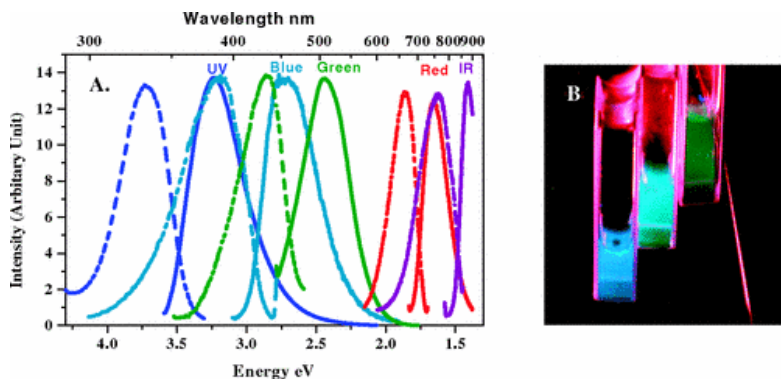


Fig. 6 UV-VIS emission and excitation profiles of different sized GNCs from ref.⁶⁰

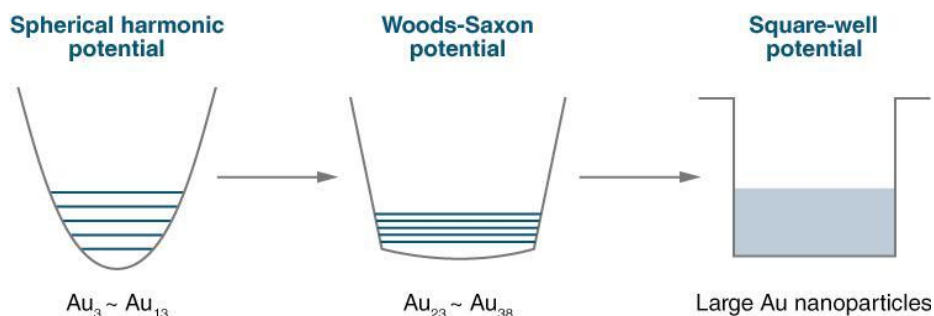


Fig. 7: Schematic of size-dependent surface potentials of Au clusters on different size scales. For the smallest Au clusters (Au_3 to Au_{13}), cluster-emission energies can be well fit with the energy-scaling law $E_{Fermi}/N^{1/3}$, where N is the number of atoms in each cluster, indicating that electronic structure transitions of these small Au clusters are well-described by a spherical harmonic potential. With increasing size, small anharmonicities distort the potential well, which at larger sizes gradually distorts into a Woods-Saxon potential surface, and eventually becomes a square-well potential, characteristic of electrons in large metal nanoparticles.⁶¹

However, core size is not the only parameter that has to be considered. Clusters with the same N but with different core structural arrangements can have different electronic structures leading to different absorption and emission features. A clear example of how absorption spectra depend on cluster geometric and electronic structure is given in (Fig. 18) which shows three clusters with the same N=25 ($[\text{Au}_{25}(\text{PPh}_3)_{10}(\text{SC}_2\text{H}_5)_5\text{Cl}_2^{2+}][(\text{SbF}_6)_2^{2-}]$, $\text{Au}_{25}\text{SR}_{18}$ and $\text{Au}_{25}(\text{SR})_{11}$) undergoing different transitions. A brief explanation about how their absorption spectra is related to their electronic structures is given in sections 1.9.2 and 1.9.3, and relies on advanced models derived from the Jellium one.

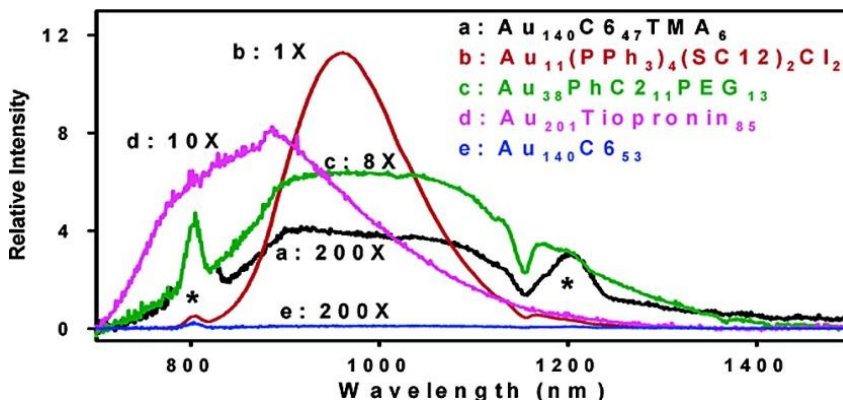


Fig. 8: Au MPCs with different core sizes and monolayers. C6, C12, PhC2, PEG, and PPh₃ represent hexanethiolate, dodecanethiolate, phenylethanethiol, poly(ethylene glycol) (MW 350) thiolate, and triphenylphosphine, respectively. The spectrum of tiopronin MPC was measured in D₂O; the others were measured in methylene chloride. All spectra were excited at 400 nm. The quantum efficiencies (relative to Q-switch 5 and DTTC) of the Au₁₁, Au₃₈, Au₁₄₀TMA, and Au₂₀₁ MPCs are 0.08, 1.2×10^{-2} , 1.8×10^{-4} , and 9×10^{-3} , respectively. Asterisks indicate artefacts from second- and third-order excitation peaks (800 and 1200 nm); the dip at 1165 nm is partly due to solvent/ligand absorption.⁸²

1.8.2 Surface effects

Surface ligands have undoubtedly been proven to play a fundamental role in GNCs photochemistry.⁸³ This emerges clearly in the work of Wang et al. which demonstrated that GNCs ranging from Au₁₁ to Au₂₀₁ and protected by different ligands, showed similar NIR emissions, which did not scale accordingly to their number of atoms.⁸⁴ One year later, the same group reported that this NIR emission intensity linearly increases with the amount of polar thiolate introduced on the clusters surface by ligand exchange (conserving core sizes). They also showed that the luminescence enhancement was proportional to the electron withdrawing capability of the ligand inserted and to the charge shift of the cluster core toward more positive values.⁸² These results have been confirmed by Wu and co-workers, who studied the photophysical properties of Au₂₅(SR)₁₈ clusters. They proved that changes in the core charge state can cause variation in the NIR emission, QYs, lifetimes, absorption and emission bands shape (Fig.7), while changes in the thiol nature influence only emission QY and lifetime.⁸⁵

Zhou and co-workers synthesized yellow and orange emitting gold nanoparticles with mean core sizes of 2,1 and 1,7 nm respectively.⁸⁶ These emission wavelengths are in contrast with the ones predicted by the jellium model and scale with the size in the opposite way. The authors found that higher valence states of cores' gold atoms, probably due to the presence of Au(I) on its surface, is a fundamental factor for GNCs luminescence. Furthermore they found that Au(I) further reduction to Au(0) lead to a slight size increase, to the disappearing of luminescence and to the appearing of a weak plasmon resonance.⁸⁶ The importance of Au(I) content for the luminescence of Red-NIR emitting GNCs has been identified in several studies.^{87,33} Palmal and co-workers found that blue, green and yellow GNCs composed by only Au(0) have emission QYs in the order of 10⁻¹ and lifetimes in the order of nanoseconds (comparable with Zheng and Dickson's PAMAM dendrimer encapsulated clusters), while the ones containing also Au(I) have QY of 10⁻² and lifetimes in the order of

microseconds.³³ Despite these results, Devadas et al. observed a dramatic effect of thiols nature on $\text{Au}_{25}(\text{SR})_{18}$ NIR emission wavelength (also if it has to be noticed that different solvent were used).⁸⁸ Similar long luminescence decay components, in the order of the microsecond, are often observed in studies on GNCs ligand dependent emissions, but the nature of the surface states from which they are generated is not completely understood. In literature, it is commonly hypothesized that GNCs interaction with the ligands could result in the generation of triplet states, whose population through ISC is aided by the strong spin-orbit coupling effect of Gold.⁸⁹

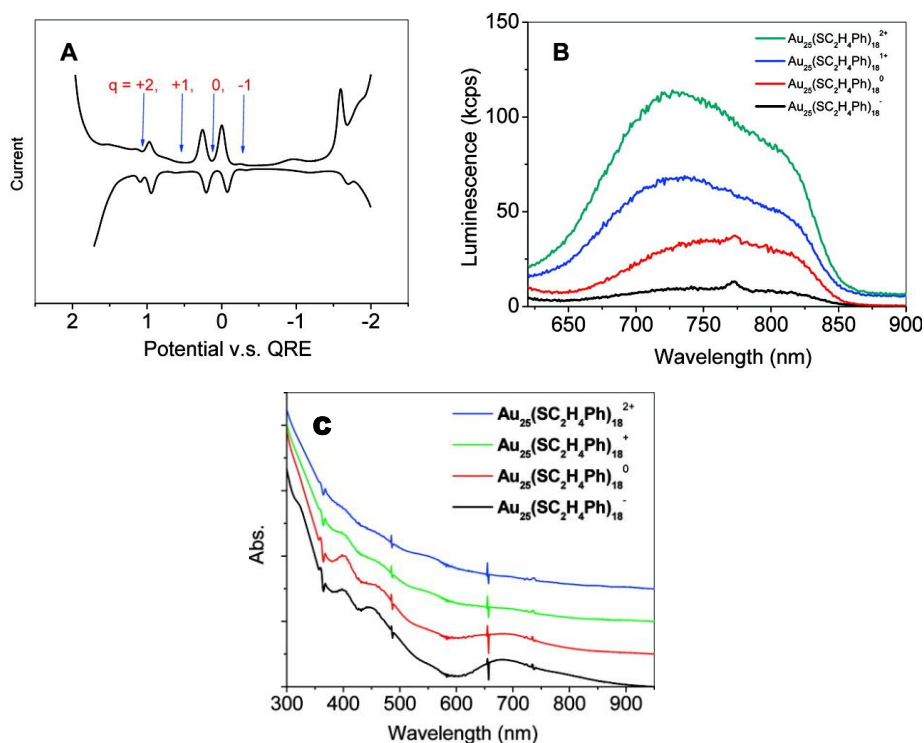


Fig. 9: Charge states of $\text{Au}_{25}(\text{C}_2\text{H}_4\text{Ph})_{18}$ probed by differential pulse voltammetry (DPV). (B) Luminescence spectra of $[\text{Au}_{25}(\text{SC}_2\text{H}_4\text{Ph})_{18}]^q$ ($q = -1, 0, +1, +2$). (C) Comparison of the UV-Vis spectra of different charge states of Au_{25} species. For clarity, the spectra are vertically shifted.⁸⁵

Another diffused hypothesis⁸³ is that luminescence could be ascribed to charge transfer from the ligands to the metal core, which affect the excited state relaxation dynamic. These charge transfers that happen in the excited state, are analogous to the LMCT or LMMCT transitions typical of metal complexes⁸⁵ and which have been also observed for luminescent Au(I)-thiolate monomeric species.^{90,85} Wu and Jin hypothesized that the charge transfer from the ligand (RS) to the core can happen through Au-SR bond or directly from the R group to the Gold (Fig. 10).

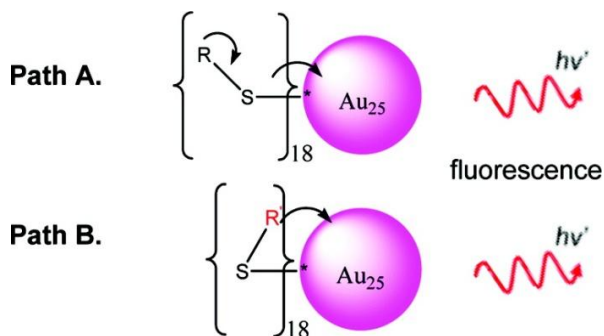


Fig. 10: Two possible pathways for the charge transfer from the ligand to the Gold core from ref.⁹⁰.

1.8.3 Auophilic interactions and aggregation induced emission (AIE)

As outlined in the previous sections, luminescent GNCs are often synthesized starting from Au(I) thiolate polymers. These species have been proven to be often present on clusters surfaces and to considerably affect their electronic structure and emission. However, it has been observed that Au(I) thiolate oligomers, in absence of NCs, can emit light when in aggregated states (Fig. 11).

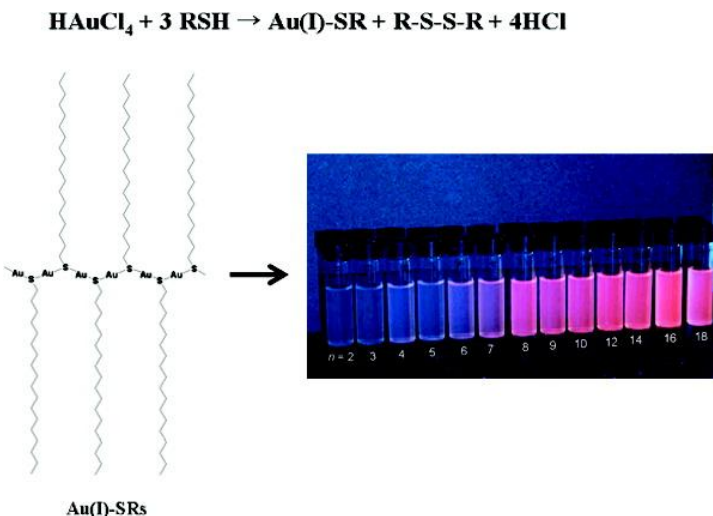


Fig. 11: Emission from aggregated form of Au(I)-thiolate polymers of different thiols $\text{HS}-(\text{CH}_2)_n-\text{H}$ bearing different sized alkylic chains, where n is the number of the methyl units which compose them.

Analogously to Au(I) thiolate monomeric complex,⁹⁰ their emission have been hypothesized to be originated from Au---Au aurophilic interaction and LMCT⁹¹ or LMMCT.^{85,92} Aurophilic interactions in the aggregates depend on the thiolate polymer side chain nature and its electron withdrawing capability, which both have been proven to effect the optical

properties of the system.^{91,92} Luo and co-workers found that glutathione gold thiolate polymers aggregation could be induced by solvent precipitation or by cation-induced aggregation, with the concomitant generation of strong microseconds lived luminescence (Fig. 12)⁹². They identified this phenomenon as “aggregation induced emission” (AIE), by analogy with the behavior of other fluorophores classes.⁹³ The research group has taken advantage of this phenomenon to synthesize GNCs with an high ratio Au(I)/Au(0) and with high emission QYs around 15%.⁹² The emission of these Au(0)Au(I)-SG GNCs was found to be very similar to that observed for gold thiolate oligomers in terms of peaks position, shape, intensity and lifetime. For this reason, the authors suggested that the observed luminescence resulted from the AIE of Au(I) thiolates on nanoclusters surface.⁹² Also in this is the case, the involved electronic state would be located on the surface, and it would have a lifetime in order of the microsecond, typical of triplets states.

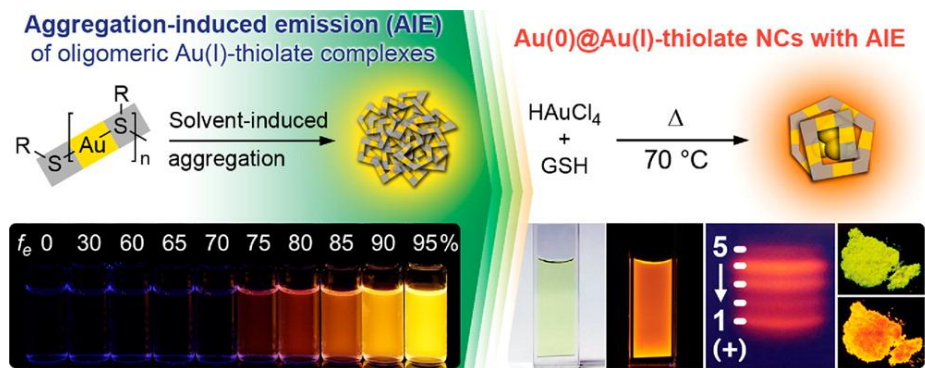


Fig. 12: from ref ⁹², at the top left, a scheme of polymeric Au-thiolate AIE emission generation, at the top right a scheme of the generation of AIE emitting polymeric-thiolate protected GNCs, at the bottom left the emission from the same Au-thiolate-polymer in aqueous solution with an increasing fraction of ethanol, at the bottom right a photo of GNCs fractionation by PAGE and their emission from solutions and solids.

1.8.4 Combined effects

In gold nanoclusters, visible emission is generally associated to transitions located into the core,^{94,95,60,61} while NIR emission is attributed to the interactions of the core with the ligands.^{94,95} Core transition are short lived (from nanoseconds for few atoms clusters,⁶⁰ to tens of femtoseconds^{94,95} for few nanometers sized nanoparticles) while surfaces transitions are long lived, in the order of microseconds. Core transitions probably result from the generation of a hole in the ground state when an electron is promoted to an excited state, while the emission would be generated by their fast recombination. The recombination in few atoms clusters is slower compared to that of larger particles presumably due to the presence of discrete energy levels and higher energy gaps.⁹⁵

Long lived NIR emission are commonly thought to involve a charge transfer process, and have been observed to be almost independent on the core size but more sensible to its oxidation state and to the ligands nature.^{88,96,85} Both GNCs NIR and visible emission quantum yields, in many cases, are very low, around 10^{-4} and 10^{-5} respectively. That suggests that, sometime, non-radiative decay pathways can dominate on the radiative ones, depending on the particular electronic structure of the cluster. In any cases, the values are much lower than that of Dickson's PAMAM dendrimer encapsulated GNCs, which are around some tens percent.⁶⁰ The higher QY of PAMAM encapsulated GNCs could be explained by the absence of non-radiative decay pathway, and by the impossibility to transfer the excited state energy to surface localized states, probably due to the absence of superficial thiolate ligands and Au(I). This could explain the size dependent visible emission, in contrast with the size independent NIR emission reported by Wang and co-workers.⁸² As suggested by Zheng et al., also the Short lifetime of PAMAM encapsulated GNCs suggest that there is no charge transfer between core and surface states.⁹⁶

Conversely GNCs protected by thiolate ligands are capable of emitting in the NIR region, probably thanks to the possible energy and/or charge transfer between the core and the Au(I) thiolate ligands.

This process can happen with decreasing emission QY, over a broad size range, up to some nanometers. This is evident for cluster larger than 1,5 nm, where the complete reduction of the superficial gold to A(0) led to the disappearance of the luminescence.⁸⁶

According to the charge transfer interpretation, some strategies to enhance the far-red/NIR emission QYs have been proposed by Wu et al.⁸⁵ and Luo et al.,⁹² but it has to be taken into account, that the different luminescence mechanisms listed above does not necessarily exclude each other, and they can act at the same time contributing to the cluster luminescence.

For example, in an ultrafast spectroscopic study on thiolate protected Au₂₅(SR)₁₈ clusters, for which the X-ray crystallographic structure has been determined, Devades et al. found two different emissions occurring simultaneously in the red and in the NIR region. The authors of this study suggested that: "... the 500 nm emission fundamentally arises from the electron-hole recombination in the Au₁₃ core with little perturbation from surface ligands, but NIR emission at 700 nm originates from the recombination of holes in the ground core state and electron decay from core excited states to S-Au-S- Au-S semi rings" (Fig. 13).⁸⁸ As confirmed by Zheng and co-workers, according to the superatom theory, "... if we just assume that the Au₁₃ core behaves like an isolated cluster, the observed short-wavelength emission at 500 nm (2.48 eV) from the Au₁₃ core of Au₂₅ clusters is very close to the 2.43 eV emission from dendrimer coated Au₁₃ ..." ⁹⁶ found by the Dickson's group.^{60,61}

Two simultaneous emission mechanisms have been identified also for BSA protected Au₂₅. Wen et al. found that BSA-Au₂₅ far-red/NIR emission is composed by two bands, one at 639 nm and the other at 704 nm which can be resolved by lowering the temperature. These two overlapped bands showed opposite peak shifts and bandwidth variations upon temperature changes, which suggest their different nature. Furthermore, luminescence lifetimes of this system measured at 600 nm showed two decay components one of 3.2 ns and another of 1.5 μ s.⁹⁷

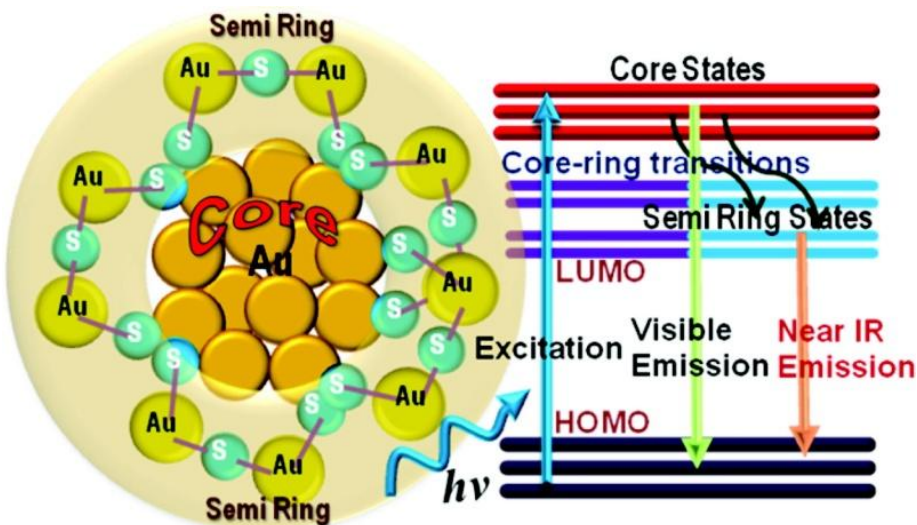


Fig. 13: Cartoon showing the relaxation pathway for $Au_{25}SR_{18}$ proposed in ref. ⁸⁸.

In a later study, these two bands have been proven to be due to prompt luminescence and delayed luminescence resulting from efficient ISC and thermally activated reverse ISC, between a singlet and a triplet states whose populations are in thermal equilibrium (Fig. 14).⁸⁹

Despite both bands are red shifted, compared to that for thiolate protected Au_{25} , BSA- Au_{25} has not been demonstrated to be composed by an Au_{13} core.

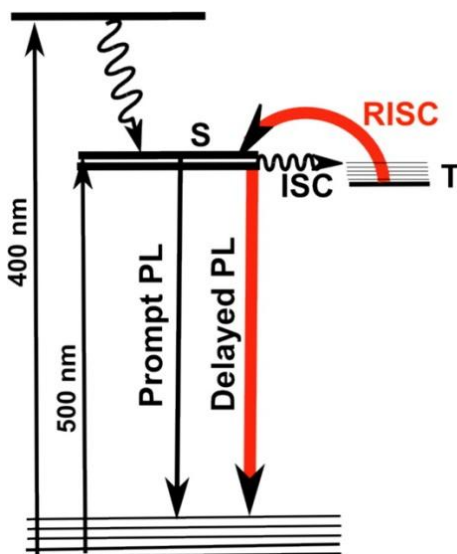


Fig. 14: Luminescence mechanism for Au_{25} -BSA GNCs proposed in ref. ⁸⁹

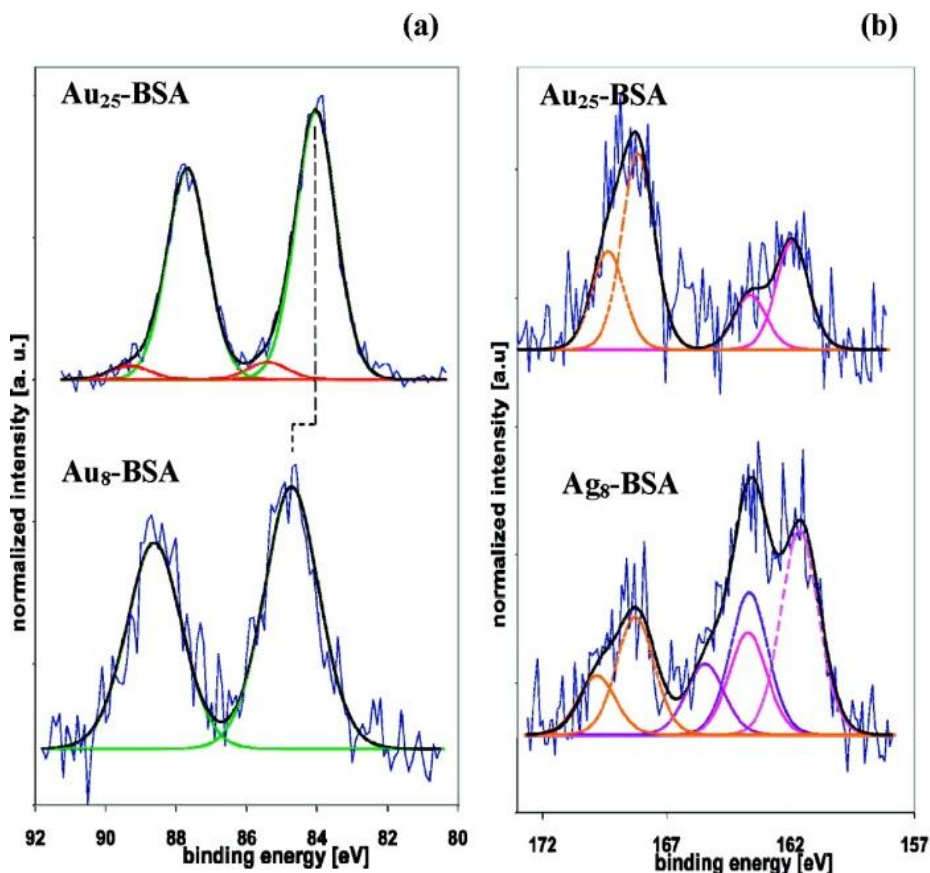


Fig. 15: XPS spectra: (a) Au 4f_{7/2} of Au₂₅-BSA shows two peaks, one peak at 84.1 eV (green curve) and the other at 85.4 eV (red curve), which are attributed to Au(0) (90%) and Au(I) (10%), respectively. The shift to the higher binding energy of Au(0) at 84.7 eV for the small clusters Au₈-BSA is related to the reduction of the core size. (b) S 2p_{3/2} confirms the presence of gold bound to sulphur (pink curve) for Au₂₅-BSA and Au₈-BSA samples with peaks at 161.9 and 161.4 eV, respectively. Unbound sulphur (purple curve) and oxidized sulphur (yellow curve) are present in both samples.⁴¹

Moreover, the XPS analysis revealed an Au(I) content of only 10% (Fig. 15),⁴¹ which is significantly lower than in Au₂₅SR₁₈. Thus, considering an Au(0) core larger than Au₁₃, the lower energy emission measured by Wen et al. could be in discrete accordance with the size dependency predicted by the JM, and its relative lifetime could match the one of Zheng's PAMAM dendrimer protected GNCs.^{60,61} Despite the superatom theory considers the ligands and the gold core as separate entities, an effect on the gold core electronic structure caused by the ligands shell, it is likely to exist.^{95,96}

Depending on the core size and on the ligand structure and natures, the core and the surface electronic states can have different relative positions on the energy diagrams. This leads to different optical properties, decay pathways and emission mechanisms. In this context, despite some trends have been identified, all of these mechanism and their complex interplays have not been fully understood.^{96,79,71,21} Further advances in photophysical studies, detailed structural characterizations and theoretical efforts are still necessary to complete our knowledge on gold nanoclusters and small Gold nanoparticles.

1.9 Magic numbers, superatoms, electronic shells closure effects and some theoretical models

As already mentioned, Gold Clusters composed by particular numbers of gold atoms, which have been named "magic numbers", have been found to be particularly stable and they are commonly called "magic clusters".^{22,98,99,100,37,38,29,6} At the beginning, this particular stability has been observed for ligand-free alkali metal clusters in gas phase,^{101,61,6} and one of its manifestation is the recurrence of particularly pronounced and periodically spaced peaks in the mass spectrum of metal clusters.^{22,98,99,100,37,38,29,101,61,6} After the exclusion of other parameters involved in MS measures, the major intensity of some peaks have been attributed to the relatively higher abundance of clusters with certain numbers of atoms, explained by the major stability.⁶

In the MS of ligand free Gold clusters, periodic patterns appear with the simultaneous alternation of the relative abundance of clusters with an even or odd number of atoms.^{102,22,98,6} These phenomena become more evident as the clusters dimensions decrease, and they are related to the emerging of quantum-mechanical behavior when their size approaches to few atoms. At this order of magnitude, several properties such as ionization energies, electron affinities, electronic polarizabilities, magnetism and reactivity become quantized. Their values, in function of the number of atoms, follow patterns that are similar to that found for MS abundances.^{102,6} Notably magic numbers as 2, 8, 18, 20, 34, 40, 58, ... correspond to the number of electrons necessary to fill in sequence the $1s < 1p < 1d < 2s < 1f < 2p < 1g$ orbitals...

1.9.1 Jellium model

Jellium is a model to describe the electronic structure of Gold clusters which explain “molecular like” clusters optical properties and the existence of magic numbers.^{61,6,22} This model come from nuclear physic and it has been originally developed to describe atomic nuclei.^{6,61} The name “Jellium” was introduced by Conyers Herring and represent the fusion of “Jelly” and “um” which is a suffix for metal names as natrium or sodium.¹⁰³ In the model, the positive charge due to the nuclei are considered as uniformly smeared all over the volume of the crystal in a uniform positive background, generating a sort of metallic “jelly”, in which electrons move.^{103,102}

Considering a spherical cluster, the potential experienced by electrons has a spherical symmetry and it acts from the center of the sphere.⁶ For this kind of potential the one-electron Schrödinger equation can be solved analytically. Analogously to an hydrogen atom, the Schrödinger equation for this system can be separated into a radial, and an angular part.¹⁰⁴

$$\text{Eq. 2: } \Psi_{n\ell m_\ell}(r, \theta, \phi) = R_{n\ell}(r) \cdot Y_{\ell m_\ell}(\theta, \phi)$$

The numbers n and l and m_l are respectively the principal, angular momentum and magnetic quantum numbers whose values are restricted to:

$$\begin{aligned} n &= 1, 2, 3, \dots \\ l &= 0, 1, 2, \dots && \text{(no restriction on } l) \\ m_l &= -l \dots 0 \dots +l && \text{(} 2l+1 \text{) values} \end{aligned}$$

Clusters orbitals, computed in this way, have the same symmetry of atomic orbitals and they are identified by the same letters (1s, 1p, 1d, 2s, 1f etc.). Differently from atomic orbitals, quantum number l have no restrictions and the principal quantum number n is calculated differently from the one

relative to atomic orbitals n_{at} . For jellium orbitals $n = n_{at} - 1$ and the number of nodes of a wavefunctions is equal to $n - 1 = n_{at} - 1 - 1$. In the case of metals of the first and eleventh group, each Gold atom contributes to fill the jellium orbitals with the single unpaired electron in their s valence atomic orbital. These electrons fill jellium orbitals according to Pauli exclusion principle and following Hunds rule.⁶

In terms of this picture, the odd and even oscillation of few-atoms-clusters properties are explained in terms of spin pairing within the single Jellium orbital, while magic numbers are explained in term of electronic shells closure.^{80,22,102,61,6} In other words magic numbers arise when the number of valence electrons (which for alkali and noble metals is equal to the number of atoms N) is such that the $1s < 1p < 1d < 2s < 1f < 2p < 1g \dots$ Jellium electronic shells are exactly and completely filled. Of course, for charged clusters, magic number are shifted; for example, for mono-cations and mono-anions, they are all shifted by $+1$ and -1 respectively.⁶

Due to their atom like features, often Jellium orbitals are called "superatomic orbitals", and the scientific community often refers to NCs as "superatoms" or, in the case of completely filled shells, as "noble gas superatoms". Experimental evidences, in effect, suggest that these systems behave as a single quantum entity.⁶¹

Magic numbers calculated using this model are dependent on the Jellium orbitals sequence in the energy diagram, which depends on the kind of potential chosen to describe the system. The last jellium orbitals sequence we mentioned was originated from a Woods-Saxon potential (Fig. 7) which is one of the most used and successful. It generated the magic numbers sequence $N^* = 2, 8, 18, 20, 34, 40, 58 \dots$ ^{6,61} The jellium model is substantially the same of the Free Electron model (which is the quantum mechanical evolution of the classic Drude model) and it is based on the same assumptions;⁶¹ the appearance of discrete energy levels is due to the boundary conditions imposed by the potential.⁶ In its simplest empirical form, the radial potential can be assumed to be simply "3-D harmonic" and, in this way, the model can be already sufficient to explain several magic numbers and clusters properties.

However, in order to completely interpret the experimentally observed phenomena, more complex formulations of the potential have to be considered. Potentials can be formulated empirically or can be evaluated, *ab initio*, by Density Functional Theory (DFT) or Hartree-Fock molecular orbital calculations.⁶ A visual representation of some metallic clusters superatomic orbitals based on the description of the Jellium model and computed using DFT can be found in ref.¹⁰⁵

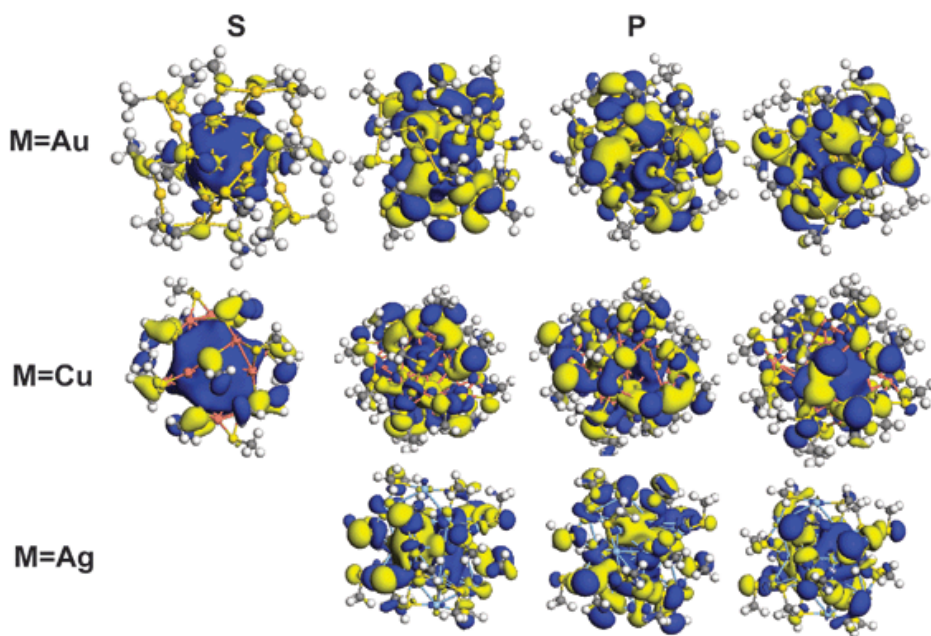


Fig. 16: The shape of the superatoms' orbital wavefunction for $M_{25}(SR)_{18}^-$, calculated by DFT according to the Jellium Model description.¹⁰⁵

More detailed information on computational methods and different models to describe clusters electronic structures, both in gas and in solution phase, can be found in^{61,106,22,102,6} and in the reviews of Häkkinen^{107,7b} and Pyykkö.^{80,108,109}

1.9.2 Jellium model limits and Superatom complex model

Jellium model explains several ligand-free-clusters properties and it has been extensively validated in gas phase, but the adaption of its mathematic for molecule protected cluster has been challenging.^{106,110} In solution, in fact, often happens that “magic core sizes” does not correspond to “magic numbers” predicted for ligand-free gas phase clusters (Fig. 17).^{111,37,38,29,110}

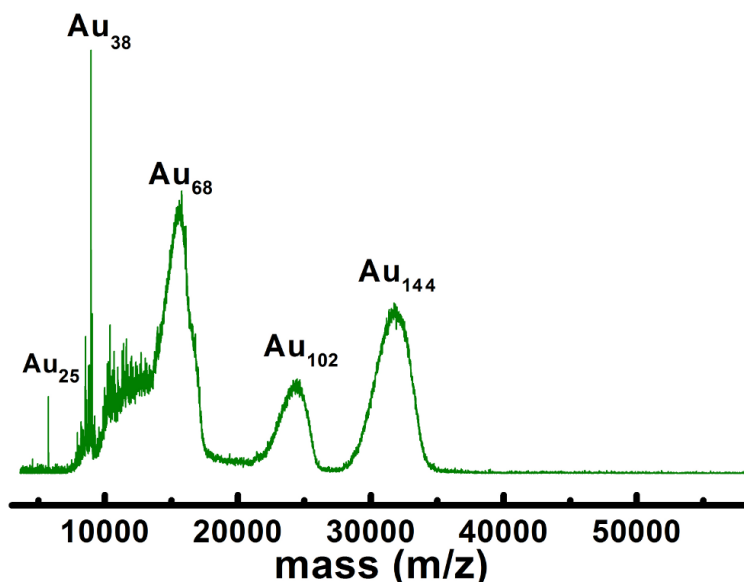


Fig. 17: MALDI-TOF mass spectrum of magic numbered hexanethiolate coated gold nanoclusters ($d < 2$ nm, < 250 atoms per nanocluster).¹¹¹

A slight idea of how things can get more complicated can be given by considering the X-ray crystallographic structures of two 25 atoms gold clusters published in 2007 and 2008. The two structures correspond to the formulas $[\text{Au}_{25}(\text{PPh}_3)_{10}(\text{SC}_2\text{H}_5)_5\text{Cl}_{22+}][(\text{SbF}_6)_{22-}]$ ¹¹² and $[\text{TOA}^+][\text{Au}_{25}(\text{SCH}_2\text{CH}_2\text{Ph})_{18-}]$ ⁷⁸ and have been shown to be characterized by two different Gold atoms arrangements.

Despite 25 does not correspond to any magic number according to the rules given above, shell closure concepts helps anyway in explaining the particular stability of both structures:

- the first is composed by two icosahedrons of 13 atoms, each with a $8e^-$ closed shell, which share one vertex.^{112,113,114,115}
- The second is an icosahedrons of 13 atoms, with a $8e^-$ closed shell, protected by six thiolate staples with formula $-Au_2(SR)_3^-$.^{78,7b}

In order to unify the description of solution phase ligand protected clusters, Häkkinen introduced the "divide and protect" concept¹¹⁰ and the unifying "superatom complex" model.^{106,116,7b} According to this model the shell closing number n^* can be calculated as $n^* = Nv_A - M - q$, where N is the number of core metal atoms, v_A is their atomic valence, M is the number of electron-localizing (or withdrawing) ligands (assuming, to simplify, that each ligand can withdraw just one electron) and q is the overall charge of the complex.^{106,7b}

In the case of $[TOA^+][Au_{25}(SCH_2CH_2Ph)_{18}^-]$, this model correctly predicts $n^*=25*1-18+1=8$, a closed shell of eight electrons, while for $[Au_{25}(PPh_3)_{10}(SC_2H_5)_5Cl_2^{2+}][[SbF_6]_2^{2-}]$ it predicts $25*1-7-2=16=2*8$.

1.9.3 Superatom model limits, Super Valence Bond and superatom-network models

Even if the superatom model has a really broad predicting power, it cannot explain all the experimental evidences. For example, Nishigaki et al. synthesized $Au_{25}(SR)_{11}$ which shows experimental evidences of the absence thiolate staple motives on the surface.¹¹³

To model clusters that cannot be described as superatomic complexes, it has been introduced the Super Valence Bond (SVB) model,¹¹⁷ which use the concepts of valence bonds (VB) theory applying them to superatoms.

According to its principles, analogously to atoms, superatoms can bind together by sharing valence electrons and/or nuclei in order to reach the shell closure.

Au₂₅(SR)₁₁: **A** can be modeled as two Au₁₃⁶⁺ sharing a vertex and two electrons to fill both their 8e⁻ shells and to generate Au₂₅¹⁴⁺. On the other hand, the cluster [Au₂₅(PPh₃)₁₀(SC₂H₅)₅Cl₂²⁺][(SbF₆)₂²⁻]: **B** can be modeled as two icosahedral 8e⁻ closed shell superatoms Au₁₃⁵⁺ which share one vertex generating biicosahedral Au₂₅⁹⁺.¹¹³

SVB model can explain the major stability of A compared to B and the lost of the single icosahedra optical properties in cluster A (Fig. 18-C vs Fig. 18-A1) compared to their large retention in cluster B (Fig. 18-A2 vs Fig. 18-A1):

- in B, the electronic shell of the two icosahedra are already filled, resulting in a weak bond between the two units and the almost complete retaining of their native electronic levels;
- in A, the two icosahedra share two electrons in order to complete their shells. That results in a stronger bond and in the generation of electronic levels different from the native ones.^{112,113}

SVB can also explain the stability of Au₃₈(SR)₂₄ and the structure of its Au₂₃ core^{118,113} which has been experimentally confirmed¹¹⁹ also for Au-Ag alloys.¹²⁰ In this case, two Au₁₃⁶⁺ icosahedra interact by sharing three atoms (a face) and two electrons to complete both their 8e⁻ closed shell, and generating an Au₂₃⁹⁺ core which is surrounded by staple motives.^{118,113}

Soon after the SVB, it has been proposed the superatom-network (SAN) model.¹¹⁶ It describes some clusters as network of closed shell superatoms, which can be interconnected and held together by Au(I) thiolate staples motives.

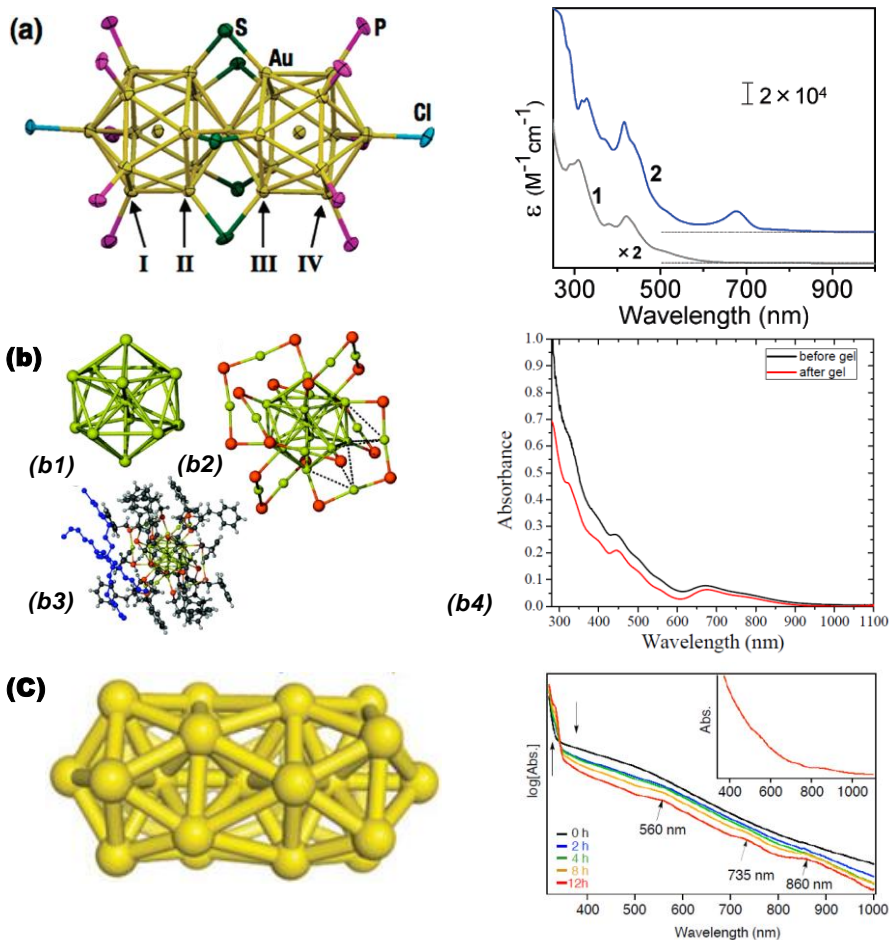


Fig. 18: a) crystallographic structure of bi-icosahedral $[Au_{25}(PPh_3)_{10}(SC_2H_5)_5Cl_2]^{2+}[(SbF_6)_2]^{-}$, 1) absorption spectra of its precursor $[Au_{11}(PPh_3)_8Cl_2]^+$, 2) absorption spectra of $[Au_{25}(PPh_3)_{10}(SC_2H_5)_5Cl_2]^{2+}[(SbF_6)_2]^{-}$ ¹¹²; b) crystallographic structure of b1) icosahedral Au₁₃ core at the center of Au₂₅SR₁₈⁻, b2) Au₁₃ core surrounded by S and Au atoms of the Au₂₅SR₁₈⁻ superficial staple motifs, b3) [TOA⁺][Au₂₅SR₁₈⁻] complete structure,⁷⁸ b4) Absorption spectra of Au₂₅SR₁₈⁻ before (black) and after (red) its PAGE purification, c) Twisted bi-icosahedral core structure proposed for Au₂₅(SDpp)₁₁ and its absorption spectra during 12h of size focusing. The inset shows the absorption spectrum after 12h.¹²¹

SVB and SAN models describe superatoms as building-blocks which can be combined together in atoms like fashions. and even if they are not definitive, both of them can provide useful descriptions of GNCs structures and predict empirical properties.¹²²

1.9.4 Kinetic factors and models limits

It has to be said that, another case study on $\text{Au}_{25}(\text{SR})_{18}$ showed that the addition or the removal of one electron from its metallic core leads to a cluster which is relatively stable. This phenomenon prove that shell-closure condition is not necessary for clusters stability.¹²³ suggesting that other factors, probably of kinetic nature,²⁹ play major roles.⁶

Negishi et al. found that, in their reaction conditions, thiolate nature dependent kinetic trapping and stabilization was the principal phenomenon governing their GNCs size distribution, with no appearance of magic numbers.²⁹ Also in gas phase at low temperature (<100 K), when cluster are produced by laser ablation and rapidly cooled by supersonic expansion, magic numbers have not been observed. An explanation is that the magic numbers appear only when quasi-equilibrium conditions are established, while in such low temperature procedure cluster production could be dominated by kinetic factors. This is in accordance with the observation that magic numbers appeared again augmenting the intensity of the laser beam.⁶ A confirmation of this hypothesis come from the recent findings of two different structural isomers of $\text{Au}_{38}(\text{PET})_{24}$ which has been identified with the letters Q and T.¹²⁴ The form T has been thought to be the kinetically favoured specie resulting from the synthesis condition employed, and which can be irreversibly converted, via thermal route, to the thermodynamically more stable form Q,¹²⁴ which has the same structure described above for $\text{Au}_{38}(\text{SR})_{24}$ observed by Quian.^{119,124}

1.10 Stability of thiols protected gold clusters

One of the main aspects to take into account during the GNCs synthesis is their tendency to aggregate in order to constitute larger colloids or bulk Gold. As introduced before, this phenomenon can be prevented if there is a passivating layer of thiols coating them, which also play a role in GNCs stabilization against etching.¹⁸ Gold colloids have optical properties which vary remarkably, depending on their size, in a range from few atoms to particles of hundreds of nanometers. For this reason, aggregation and etching phenomena are usually associated with detectable changes in clusters optical properties and it makes the UV-Vis spectroscopy the most commonly employed technique to test Gold NPs and NCs stability.

The studies on Gold nanoclusters stability showed that some of them are remarkably stable in different conditions. Some of these successful examples are reported below.

PVP protected Au₁, Au₂ and Au₃ GNCs synthesized by Beatriz Santiago González et al. not only displayed a remarkable stability upon exposure to H₂O₂ and NaBH₄, but they also have shown negligible changes after two year of exposure in ambient conditions.⁶³ Aldeek and co-workers prepared 1,2 nm GNCs functionalized with different derivatives of lipoic acid and they tested their long-term colloidal stability in different conditions, reporting a strong resistance in presence of high electrolyte concentrations, in the presence of reducing agents as glutathione and over a wide range of pHs (2–13).³⁴ Duan et al. synthesized extremely stable mercaptoacetic acid functionalized GNCs, starting from Au₈ precursor, and observed no obvious effect on their luminescence properties even in 1 M HCl or 1 M NaOH.⁶⁴ Au-BSA GNCs made by Zhang et al. have been shown to retain their optical properties in physiological conditions⁴⁰ and also the orange-yellow emitting 1,6 nm GNCs produced by Xu and co-workers have shown good stability in the physiologically relevant pH range and ionic strength.³⁰ Bian Pingping et al. observed that Au₁₇ GNCs capped with MUA and Histidine mixed together were stable in

atmospheric conditions over a period of two months.⁷⁴ Oh et al. used bidentated thiols to synthesize PEGylated NIR emitting GNCs and proved their stability in pure water, DMSO, tissue culture growth media, high salt concentrations (5X PBS) and in different storage and reaction conditions. Photophysical stability of their system in cytosolic environment has also been demonstrated directly inside cells.¹²⁵ Palmal and co-workers synthesized GNCs with tuneable emission wavelengths from blue to NIR and tested their stability in imaging conditions.³³ While blue, green and orange emitting clusters were found to be stable, the authors reported the instability of red emitting GNCs under light irradiation.³³

The results from ref. ¹²⁵ and ³³ may seem conflicting, but their difference simply reflect the strong dependence of GNCs stability on their protecting ligand and on their features. The importance of capping agents nature is confirmed also by the results of Santosh Kumara and Rongchao Jin who compared two different $\text{Au}_{25}(\text{SR})_{18}$ clusters coated by captopril or glutathione and found that their thermal stability is strongly depend on the substituent.¹²¹

Here we reported some cases to show that it is possible to obtain GNCs which are stable in different conditions and we also reported a couple of examples that account for the impossibility of generalizing observations for all kind of GNCs. The stability of these species is governed by the interplay of quantum mechanics effects, briefly outlined in the "theoretical models" section, and the parameters which also affect the stability of larger colloidal gold particles, such as steric protection, concentration, Z-potential surface charges and tight packing of the passivating ligands.

1.11 XPS and HRTEM Lattice spacing determination of thiols protected GNCs

Most of the assessments of thiols protected GNCs electronic structure by XPS reveal that the binding energy between the sulphur atom and the gold surface is located between that found for Au(0) metallic films (84 eV) and Au(I)-thiolate complexes (86 eV), suggesting the presence of both Au(I) and Au(0) (Fig. 19 B).^{40,30,77,126,127,74}

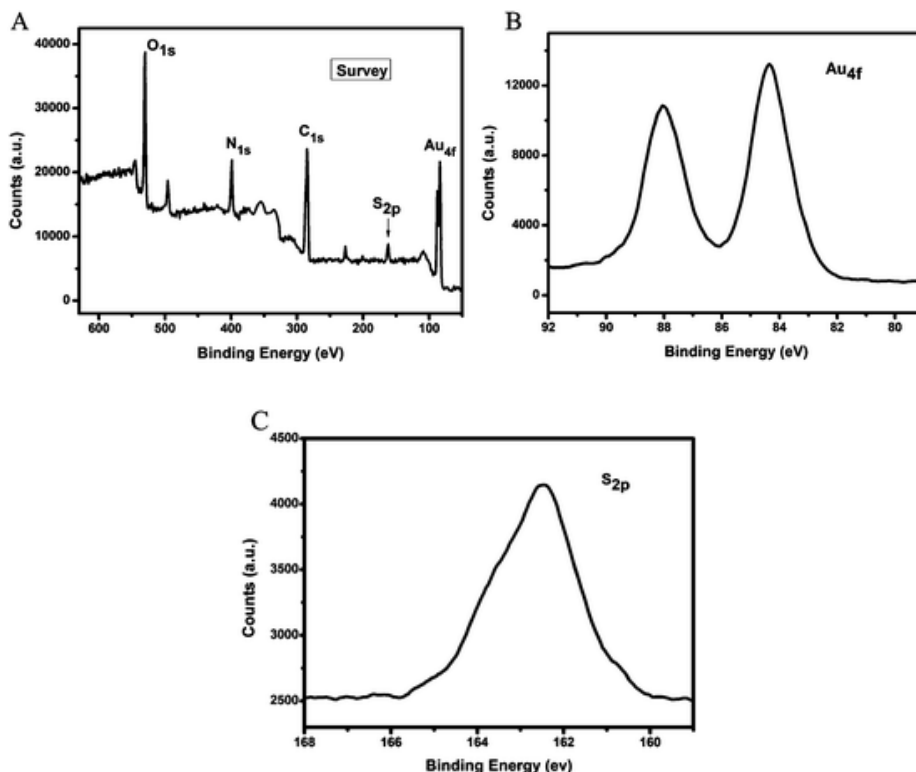


Fig. 19 XPS analysis of the AuNCs@GSH: (A) survey scan; (B) Au 4f; (C) S 2p.¹²⁷

The presence of Au(I) on cluster surface has also been observed using different techniques as X-ray crystallography,⁷⁸ in the study of Heaven et al. on Au₂₅(SR)₁₈, and XANES spectroscopy, in the work of Sun et al. on apoferritin templated GNCs. XANES helped the authors to confirm that these protein templated red emitting Gold clusters are composed mainly by Au⁰ mixed with little percentages of Au ions, most likely Au¹⁺ and excluding Au³⁺.³¹ X-ray crystallography allowed to determine that Au¹⁺ can be present on Gold surface as staples of gold thiolate polymers, which are a very recurrent motive in GNCs chemistry.⁷⁸ As found by Le Guével et al., XPS analysis of BSA-Au₂₅ revealed substantial similar features to that of thiolate protected clusters with percentages of Au(I) respect to Au(0) that are generally lower (Fig. 15).⁴¹ Palmal and co-workers observed the same features for red emitting clusters composed by more than 12 atoms, but they found that their blue, green and yellow emitting clusters, composed by less than 12 atoms, contained just Au⁰. They proposed that gold oxidation state, on clusters surface, depends on the synthesis condition and they correlated the presence of Au¹⁺ thiolate to longer luminescence lifetime, higher emission QY and lower photostability.³³

In HRTEM measures, the lattice spacing found for most of GNCs is approximately the same found for bulk Gold. For example 0,23 nm has been found by Xu et al. for d=1.96 nm⁷⁷, 0,24 nm has been found by Zhang et al. for d=1,9 nm and¹²⁷ 0,22 has been found by Sun et al. for 1,2 nm GNCs using Cryo-EM (Fig. 20).³¹

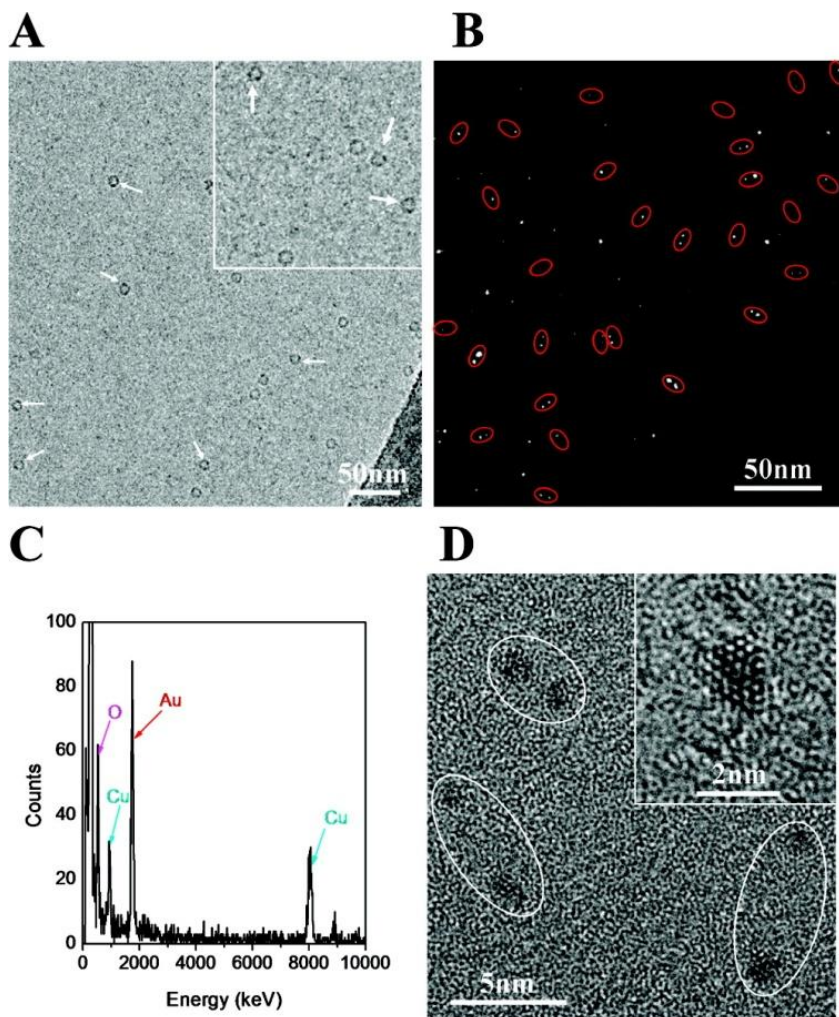


Fig. 20: Characterization of far-red Au-Ft. (a) Cryo-electron microscopy (Cryo-EM) image. Paired Au clusters were observed within the ferritin nanoreactor (indicated by arrows). (b) HAADF-STEM image of far-red Au-Ft. There are about 40 paired Au clusters (indicated by ovals) within every 8 nm zone. (c) EDS of far-red Au-Ft showing the presence of elemental Au, but not iron in the nanostructure. (d) HRTEM image showing Au clusters at higher resolution. The crystal lattice spacing is about 0.22 nm (inset), and the 111 face of Au is evident.³¹

1.12 Applications in imaging and theranostics

Zhengyong Zhang et. al produced 11-MUA and DPA functionalized 1-2 nm GNCs with emissions tunable in the range 530-630 nm. These clusters have been successfully employed for HeLa cells imaging *in-vitro* and they have been shown to bond mainly the cellular membranes. In some extent, this system was also ingested by cells, but MTT assay, after 3h of incubation, has shown very low toxicity toward the HeLa line also at concentration of 200 μ g/ml.¹²⁶

Similar results have been obtained by Palmal et al. who, using several different thiols, synthesized GNCs with hydrodynamic diameter of about 5-12 nm and with tunable emissions from blue to NIR. They showed that the emission wavelength can be tuned with some exceptions and some limitations, for the majority of the thiols studied in this work by modifications in the synthetic strategy. They also proposed a strategy to functionalize their Gold clusters with polymers to improve their water solubility, and to easily conjugate them with targeting ligands. In this study different GNCs have been successfully employed to perform cellular luminescence imaging systematically assessing their stability during the measure under irradiation conditions.³³

HeLa cells line has been used, again, from Bian Pingping et. al for testing Au₁₇ GNCs capped with a mix of MUA and Histidine. This system was uptaken by cells via endocytosis and it has been shown to have a negligible cytotoxicity at concentration lower than 40 μ M. Incubation of this nanoprobe in cell culture, at a concentration of 20 μ M, allowed luminescence imaging of the cytoplasm, where these GNCs tend to localize in the biological sample.⁷⁴

Also Cysteine GNCs have been employed as marker for cancer cells and they have been tested on HeLa and A549 lines. They showed an efficient

uptake from these cells and a strong luminescence signal once internalized. Interestingly, the probe retained its emission properties even after 90 minutes of continuous LASER irradiation. This is particularly significant, since they showed a superior photochemical stability, also if compared with CdTe QDs and FITC. Furthermore, the lifetime of these GNDs is an order of magnitude greater than that of CdTe and two orders greater than common fluorophores, leading to a better applicability of GNCs, for applications such as gated imaging.⁷⁷

Luminescent GNCs have been tested even *in-vivo*. Poon et al. administered *in-vivo*, via tail vein injection, Tiopronine capped 2,7nm GNPs to image a Lewis lung carcinoma (LLC) induced in a mice model. The mouse organs have been analyzed after dissection using NIRF, PA imaging and inductively coupled plasma mass spectrometry (ICP-MS) (which is the gold standard for the quantitative detection of gold in tissues⁷⁶). The study showed that the accumulation of the GNPs occurs mainly in tumor, spleen, Liver and Kidney with a Good accordance between NIRF, PA and ICP-MS results. The slight discrepancy in the inner particles distribution values measured by NIRF and PA, has been attributed to the different intrinsic limitations of the two techniques. Interestingly, these GNPs have been shown to be still accumulated in the same organs after 24h, but further information on their clearance and toxicity have not been provided as the mice have been sacrificed for single organ analysis.²⁴

In the study of Nair and co-workers, mice with well-defined tumor margins were injected intravenously with PFL-AuC NPs, they were monitored by NIRF imaging and treated with green LASER for photodynamic therapy. 3h p.i., these NPs mainly accumulated in tumor sites, allowing a clear detection of the tumor position. A low signal was detected also in liver and kidneys, organs involved in the clearance pathways. After 24h, NPs concentration in liver and kidneys was more than doubled, while the in-tumor concentration was reduced of about 43%. The same NPs lacking the protoporphyrin IX (PPIX) and Folic Acid (FA) components, showed the complete inability of staining the tumor, probably due to the combination

of a lower luminescence QY of the particles and the absence of the FA targeting function. The LASER irradiation led to a successful phototherapy, combined with the possibility of its real time follow up by NIRF imaging. Tumors volumes and biomarkers have been monitored for seven days by a vernier caliper and by fiber-optic luminescence spectroscopy. The seventh day, mice have been sacrificed for the histopathological evaluation of the interested tissues in order to verify the *in vivo* results. All of these techniques showed tumor regression in the PFL-AuC treated mice, in contrast with a tumor increase in the control mice. Tumor volume decreased in treated mouse only for the first five days and then reached a plateau, while tumor biomarkers showed considerable changes until the seventh day. Finally histopathology confirmed the results obtained with the other two techniques.²⁵

Eunkeu Oh et. al synthesized PEGylated GNCs by using PEG derivatives with a double thiolic function which provides a stronger bond between Gold and the capping agent. These derivatives had PEG chains terminating with three different functional groups, leading to the formation of nanoparticles that display carboxylate, ammonium, azide or methyl ester group on surfaces. Luminescence imaging experiments have been performed incubating cells in presence of GNCs, functionalized by PEG-COOH, PEG-NH₂ and PEG-NH-CPP (CPP cells penetrating peptide). CPP functionalized GNCs were uptaken by COS-1 cells, and displayed a mostly endosomal and perinuclear localization with a strong overlap with the signal of a labeled transferrin, used to monitor the endocytic pathway. On the other hand, PEG-COOH and PEG-NH₂ seemed to be unable to cross the cellular membrane. In the same work, imaging with these non-penetrating NCs has been achieved by microinjecting them into cells. By using this administration method, PEG-NH₂ NC was still unable to cross the nuclear and the cellular membrane, but it can diffuse through the cytosol, giving an almost uniform staining pattern. PEG-NH₂ NCs photo-stability have been tested directly in the cytosol and this system showed an high signal to noise ratio and a very strong

resistance to photobleaching, even under intense continuous illumination.¹²⁵

Cuiji Sun et al. tested apoferritin protected GNCs on human colorectal carcinoma cell line, Caco-2 and on human hepatoma cell line HepG2. These protein coated GNCs have been shown to be not toxic to both cell lines and to be uptaken only by the Caco-2 specie. The uptake is probably mediated by apoferritin specific receptors which are not expressed by the HepG2 line. In this case the uptaken clusters tend to localize in proximity of the plasma membrane and in few vesicles dispersed in the cytoplasm. Apoferritin-GNCs have then been tested on mice and their distribution has been assessed *in-vivo* by whole body luminescence imaging (Fig. 21). The study showed that the protein-gold complex, after tail vein injection, initially accumulates in the kidneys, liver and spleen. Then Its concentration starts to diminish rapidly in the spleen after only 1h from the injection, while the same effect is slower in liver and kidneys. In fact, luminescence signal was detectable *in-vivo* at least up to 7h in these major organs, and *in-vivo* results have been confirmed by *ex-vivo* evaluations, performed by ICP MS and luminescence imaging. It is worthy to notice that the approximate size of this nanosystem is around 12 nm, more than the double of the cut off size for kidneys filtration. For this reason, its penetration in this mayor organ has been hypothesized to be mediated by specific receptors which regulate ferritin metabolism. The luminescence signal from the kidneys was mainly localized around proximal tubule cells and further localization assessments found the presence of ferritin-GNCs in both renal cortex and renal medulla.³¹

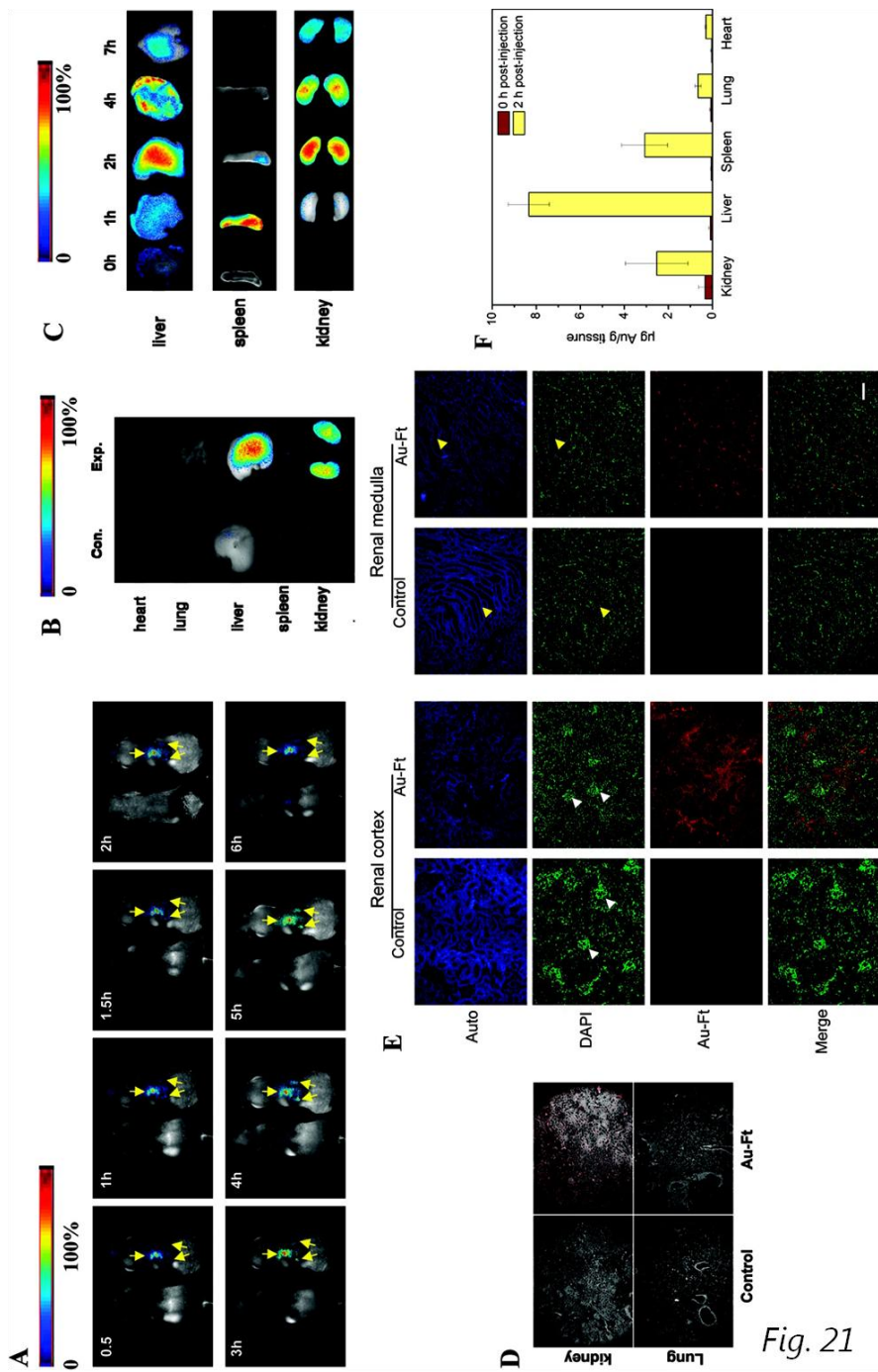


Fig. 21

Fig. 21: In vivo and ex vivo imaging of far-red Au-Ft with female nude mice and ICP-MS analysis showing the distribution of Au in various tissues. (a) Whole body dorsal luminescence images of nu/nu female mice at different time points after far-red Au-Ft injection into the tail vein. The final concentration of Au-Ft was 0.8 nmol/g body weight. For each panel, the Au-Ft injected mouse is shown on the right and a saline injected control is shown on the left. Ex vivo imaging of Au-Ft in mouse organs (b and c). (b) Luminescence images of nu/nu female mouse organs 6 h after Au-Ft injection. Control mice were injected with physiological saline, and organs from these animals are shown on the left. (c) Luminescence images of nu/nu female mouse organs at different time points after Au-Ft tail vein injection. The final concentration of far-red Au-Ft was 0.8 nmol/g body weight. Tissue distribution of far-red Au-Ft in both kidney and lung in Au-Ft injected mice or the control mice (d and e). (d) Organ distribution of far-red Au-Ft in both kidney and lung of Au-Ft injected mice or the control mice. (e) The detailed tissue distribution in kidney of Au-Ft injected and control mice. The first row showed the tissue background luminescence (autoluminescence), which indicated the kidney tissue structure. The distribution of Au-Ft luminescent probe in different kidney regions was shown in the second row. The DAPI staining in the third row indicated the nuclei of kidney tissue. The bottom row was an overlay of the second and third rows. The white arrow showed the glomerulus, and the yellow arrow showed the renal tubular. Scale bar = 200 μm . (f) ICP-MS analysis showing the distribution of Au and specific tissue accumulation in various tissues at 2 h after injection of Au-Ft. Kidney and liver are the major sites of Au accumulation.³¹

Zheng and coworkers synthesized Au-BSA GNCs, slightly modifying the method of Xie,³⁹ and confirmed the suitability of this system for cells and whole small animal luminescence imaging. The probe, with an emission QY of 9.4%, displayed almost no toxicity on MCF-7, HeLa, and L02 cell lines, and it was internalized during the incubation, enabling good cells imaging. On a mice model, the probe was directly injected in induced subcutaneous tumoral mass of MCF-7 and HeLa cells to perform whole body luminescence live imaging. The system was tested using an excitation and an emission wavelength of 520 nm and 710 nm respectively and allowed the recording of clear tumor images also *in-vivo*. The best imaging condition were achieved 60 min post injection, after which, the probe is gradually cleared from the tumor. After 12h histopathological

analysis of excised organs showed almost no luminescence signal, except from the tumor mass. No sign of clear toxicity has been observed on the mouse during the overall treatment.⁴⁰

Also Gao and colleagues synthesized red emitting BSA protected GNC, and they tested it *in-vivo*, on mice, in order to perform whole body luminescence imaging and 2D/3D computed tomography imaging (Fig. 22). As suggested in previous studies, they found that this probe mainly concentrates in kidneys and liver within two hours after tail vein injection and it can be excreted with urine. In the conditions chosen for this study, mayor organs visualization through whole body luminescence imaging was impossible using this BSA protected AuNCs. This is probably due to the poor penetration of light in tissues. A detailed whole body visualization of the urinary organs has been achieved with CT, for which it was demonstrated a much higher contrast compared to commercial iopromide. In the same experiment, weak signals allowed also the visualization of other mayor organs (Fig. 22). Ex-vivo luminescence imaging to quantify gold amount in dissected mayor organs was successfully achieved. In effect, the luminescence emission intensity was consistent with the signal observed from the same organs in whole body CT, with strong signals collected from kidneys and liver and a weak signals from lungs and spleen.¹²⁸

The combination of the results of ref.¹²⁸ and ⁴⁰ suggest that, in the order of 24h, BSA-GNC is cleared by kidneys.^{128,40}

Dongyun Chen et. al used orange emitting 1nm GSH coated GNCs to functionalize 120 nm polymeric self-assembled pH-labile NPs. This system has been designed for the delivery of hydrophobic drugs, triggered by the mildly acidic environment experienced by the probe once uptaken in targeted cancerous cell expressing FA receptors.

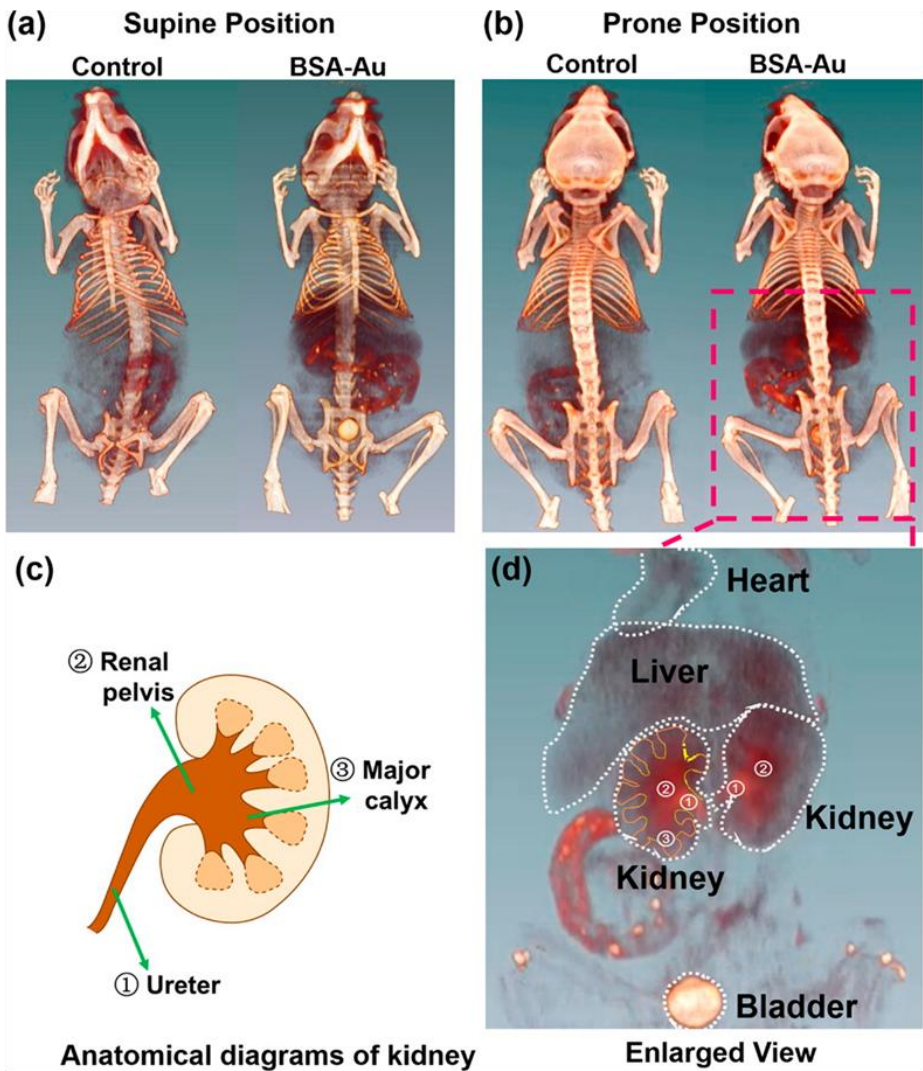


Fig. 22: *In vivo* 3D CT images of saline and BSA-Au clusters-injected mice at 2 h post injection in the (a) supine and (b) prone positions. (c) An anatomical diagram of the kidney. (d) An enlarged view of the major organs of the BSA-Au cluster-injected mouse (bone is subtracted out). The heart, liver, kidneys, and bladder are outlined with white dashed curves. The orange and yellow dash curves marked the ureter, renal pelvis, and a major calyx.¹²⁸

Thanks to the presence of GNCs, the distribution of this multifunctional probe has been assessed by luminescence microscopy, both on cell culture and in mice excised tissues after *in-vivo* administration.¹²⁹ An Au-BSA-IGG-Porphyrine nanosystem has been developed for targeting, imaging and light induced suppression of Staphylococcus Aureus bacteria in PDT applications. *In-vitro*, both Methicillin-resistant (MRSA) and Methicillin-sensitive (MSSA) strains were targeted thanks to the antiSAIgG, and the light-driven suppression mediated by Porphyrine generation of singlet oxygen has been shown to be efficient. In fact, after 30 minutes of red light irradiation, the number of colony-forming units (CFU) of both strains was reduced of about 90%, while the control (bacteria in absence of the nanosystem) only showed a diminution of about 30 % in the same conditions. The presence of the gold nanocluster inside the BSA structure allows to clearly visualize the targeting process with luminescence, upon green light irradiation and red light observation. Test on S. Aureus and E. Coli mixed together, showed a great selectivity of the nanosystem toward S. Aureus of both strains. The toxicity of the nanosystem on the bacteria was negligible in dark condition and it has been shown to be greatly enhanced upon red light irradiation, with killing effects slightly superior against MRSA compared to MSSA. These results show the potentialities of this nanosystem as theranostic agent, as it can selectively target S. Aureus and allow its detection irradiating with green light and its treatment by PDT using red light. Unfortunately no additional information on its applicability *in vivo* are provided in the same work.¹³⁰

Pu Zhang and co-workers synthesized Au₂₀BSA GNCs functionalized with Folic and Hyaluronic acids as probes for active *in-vivo* targeting, detection and imaging of tumours. These nanoprobables have been tested *in-vivo* and *in-vitro*, and have shown no sign of toxicity. The study demonstrate that for the first 1-3h these protein-GNCs species can diffuse through almost the whole mice and that they are subsequently metabolized and cleared overtime via renal or hepatic pathways. *In-vivo* experiments demonstrated the effective possibility of selectively image tumor sites using these probes, thanks to their retention and slower clearance from tumoral

tissues. The luminescence signal from the stained tumors was from 4,5 to 6 time stronger than the one detected from the rest of the body. The In-tumor probe accumulation has been demonstrated to happen mainly thanks to the receptor mediated uptake of the probe, while the EPR phenomenon contribute only slightly to the retention of these nanosystems in the targeted area.¹³¹

J. Wang et. al noticed that tumoral cells can selectively synthesize AuNCs from gold precursor in vivo. BALB/c athymic nude mice were implanted subcutaneously with HeLa cells and the tumor reached 7mm size after 10 days. They found that a 10 mmol L⁻¹ AuCl₄⁻ solution prepared in PBS (100 mL) administered to BALB/c athymic nude mice via tail vein injection, allows the precise localization of the tumor via whole body NIRF imaging. Tem analysis and ICP MS of dissected organs confirmed the presence of AuNCs inside cells of tumoral tissue, while in the normal tissue the gold content was relatively low and NCS were not detectable. A quite large amounts of gold were found in the excretory organs after 48h from the injection, and some clues on the biocompatibility and possible clearance of these in vivo generated Au-NCS consists on the unchanged behaviour of the injected mice and the finding of Au-NCS in their urethra.⁷⁵

Zhou et al. discovered that 2-nm GSH-coated luminescent AuNPs (GS-AuNPs) can be easily cleared out of mice organism via renal pathway, with efficiency one or two orders of magnitude higher than other GNPs with similar size but different surface functionalization. This has been hypothesized to be due to the small size of the particles and to its reduced interaction with serum proteins. The research group used particles luminescence to track their renal excretion and urine were also analyzed with ICP-MS to control the clearance kinetic. Renal excretion started 2h post injection (p.i.) and proceeded with the clearance of more than the 50% of injected cluster after 24h p.i., up to 75% 72h p.i. The retention of particles luminescence properties, after their *in-vivo* circulation and excretion, accounted for the stability of this probe in physiological conditions.^{132,133}

Zhang et al. successfully employed GSH and BSA protected Au₂₅ GNCs as radiosensitizer for cancer radiotherapy, obtaining promising results.^{51,7d} The study compared *in-vivo* radiotherapy enhancement efficacy, toxicity, biodistribution, tumor accumulation (via EPR) and clearance kinetic of both clusters. For comparative biodistribution assessment by the whole body luminescence imaging, clusters were labeled with Cys5. Authors found faster renal clearance, higher in-tumor accumulation and lower collateral in-organs retention for Cys5-GSH-Au₂₅ than for Cys5-BSA-Au₂₅. 20 days p.i. of non labeled clusters, pathological data from major organs showed a good biocompatibility of both BSA and GS protected ones. However, some evidences of liver toxicity and reduction of red blood cell count have been reported for the BSA protected one. (Fig. 23).⁵¹

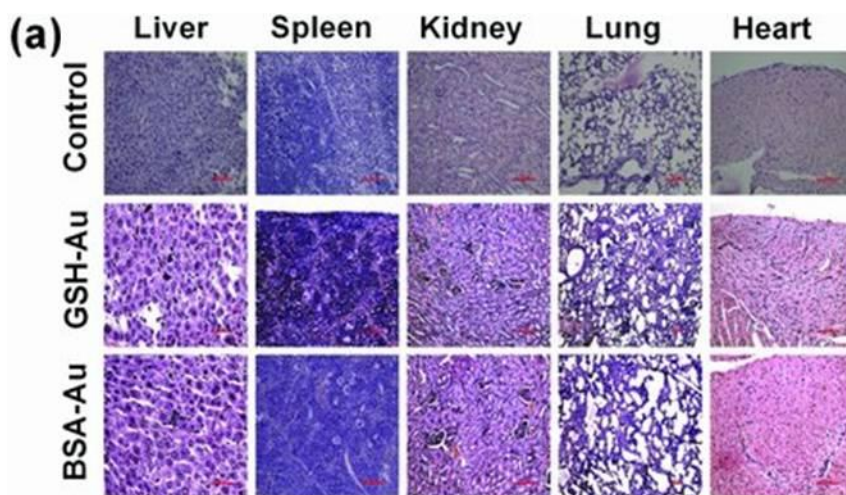


Fig: 23: a) Pathological data from the liver, spleen, kidney, lung, and heart of mice treated with GSH- and BSA-Au₂₅ NCs at the concentration of 10 mg-Au kg-body⁻¹.⁵¹

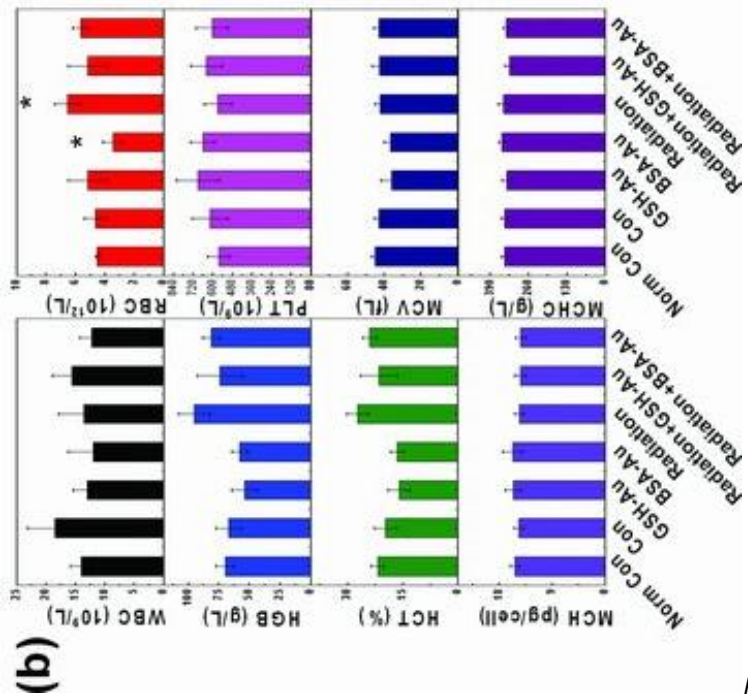
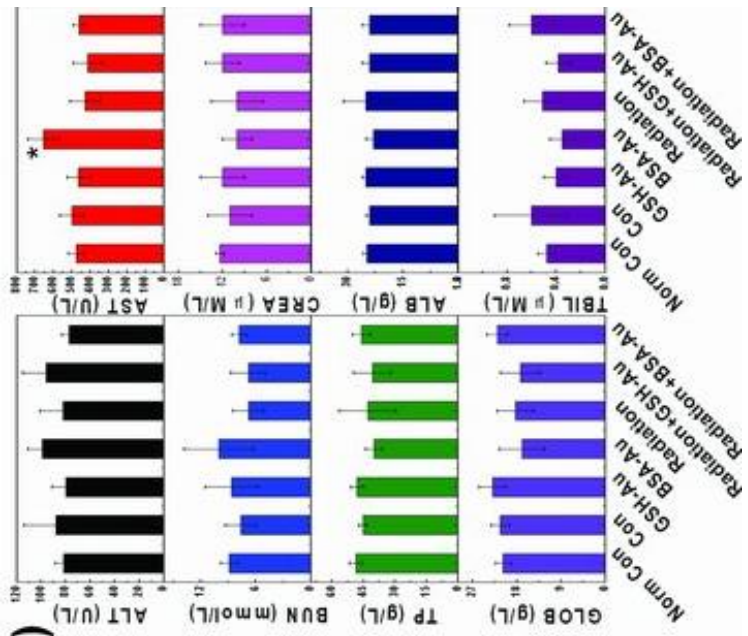


Fig:23

Fig. 23 b) Haematology data of mice treated with GSH- and BSA-Au₂₅ NCs at day 20 after injection. The results show mean and standard deviation of white blood cells (WBC), red blood cell (RBC), hematocrit (HCT), mean corpuscular volume (MCV), haemoglobin (HGB), platelets (PLT), mean corpuscular haemoglobin (MCH), and mean corpuscular haemoglobin concentration (MCHC). c) Blood biochemistry analysis of mice treated with GSH- and BSA-Au₂₅ NCs at day 20 after injection. The results show mean and standard deviation of alanine aminotransferase (ALT), aspartate aminotransferase (AST), total protein (TP), albumin (ALB), blood urea nitrogen (BUN), creatinine (CREA), globulin (GOLB), and total bilirubin (TB). Data were analyzed by Student's t-test and * in b) and c) indicates $P < 0.05$.⁵¹

Glutathione and cysteamine capped FGCs have been shown to exhibit pH-dependent adsorption on live cell membranes.³³

On a mice model, using GS-GNPs functionalized with FA, Chunlei Zhang et. al confirmed the possibility to image cells *in-vitro*, and to selectively image induced tumors *in-vivo*. This system has been proven to be almost not toxic to tested cells (human gastric cancer MGC-803 and gastric epithelial GES-1) and showed good biocompatibility *in-vivo* as well. Histological assessment of mice tissues over 14 days, after a single injection of the probe, showed no necrosis, suggesting its suitability as injectable imaging agent. Multimodal imaging of the induced tumor has been successfully performed on mice, using NIRF and X-ray computed tomography (CT) imaging. These particles have been administered to mice via intratumor injection and have been shown to diffuse inside the tumor mass and to allow its detection even 4h post injection.¹²⁷

Jinbin Liu et al. compared *in-vivo* the tumor targeting efficiency of both IRDye 800CW dye and 2,5 nm GSH functionalized NIR emitting GNPs. A mice, used as a model, has been subcutaneously injected with human breast cancer cell line MCF-7. When the tumor reached a palpable size of 6-8 mm GNPs and the IRDye were injected intravenously for the imaging study. In an initial stage the two species have similar distribution kinetic, but 12h post injection, GNPs accumulated at tumor site at a concentration 10

times higher than the molecule, and they had been cleared from normal tissues 3 times faster. In this process, GNPs reached the detection threshold three times faster than the Dye. The authors demonstrated that GNPs with size below the renal filtration cutoff can be effective in passive tumors targeting as they are still capable of accumulating in those tissues by EPR effect. In the same study they also demonstrated that this kind of GNPs can distribute rapidly in the mouse tissues and that they can be excreted with the urine.

If compared with inorganic QD, despite their lower QY, in the case of passive tumor targeting this emitting Gold specie allowed to achieve a better contrast, thanks to their distribution kinetic profile.¹³⁴

Ligands [Molecular Formula]	Core size (nm)	HD d (nm)	Abs. (nm)	Em. max (nm)	Qy (%)	τ (ns)	Toxicity	Biosystems tested and methods
GSH+Fe ₃ O ₄ NPs	2.0 ±0.2	-	$\lambda < 600$	650	4.3	-	The system has been tested on cells in combination with Fe ₃ O ₄ NPs and it is out of the purposes of this article.	-
Cysteine	1.96	-	300 < λ < 380	635	4.1	2510	90% after incubation with Cys-Au dots in the concentration range of 0–500 mM for 24 h. Very low.	MTT assay on HeLa and A549 cells ³⁷
Single BSA	1–2	?	$\lambda < 520$	710	9.4	463	In vitro: Very low. In vivo: no sign of evident toxicity but further evaluation is required.	MTT assay on MCF-7, HeLa and L02 cell. Mice ⁴⁰
Homocysteine	1.6 ±0.2	2.3 ±0.3	$\lambda < 475$	560	3.01	-	Low. Cell viability was greater than 75% after 48 h incubation with a concentration of NCs in the range of 0–400 mg/mL.	MTT assay on HeLa cells in vitro ⁴⁰

Tiopronin	2.7 ± 0.9		$\lambda < 750$	780	0.162	-	Not evident toxic effect on mouse in vivo 24h after tail injection (100 μ L solution of 100 μ M gold NP).	C57/BL6 mice. ²⁴
1)LA 2)LA-HMDA 3)LA-FA 4)LA-FA-HMDA-PPIX	1.4	-	$400 < \lambda < 650$	720	5,1 (10% without PPiX)	5.68 ps (37 μ s without PPiX)	Not toxic.	MTT assay on L929 mouse fibroblasts. ²⁵
PS- (SingleBSA)- (antiSAIgG antibody)	1.8 ± 0.4	-	$\lambda < 520\text{nm}$	650	14	-	Minimally toxic to Bacteria in dark condition. Highly toxic to bacteria under red light illumination.	Staphylococcus Aureus; MSSA and MRSA. ¹³⁰
11-MUA and DPA in different proportions	1.8 - 2.3	-	From $\lambda < 400$ to $\lambda < 500$ Depending on the proportion	Tunable in the range 530-630	$1 < \phi < 1.6$	500 - 1200	Very low	MTT assay on HeLa cells. ¹²⁶
Glutathione (GSH)	1.90 ± 0.6	3.1 ± 0.7	$\lambda < 550$	650	1.6	-	Very low	Human gastric cancer MGC-803, gastric epithelial GES-1 cell lines and Mice. ¹²⁷

Copolymer shell of PEGDA and P	< 1	5 < d < 12	$\lambda < 420$	450	5 < ϕ < 17	3 < τ < 12	Not toxic also at concentration of some mg/ml	MTT assay on Human Embryonic Kidney HEK293 ³³
TA-PEG-NH2 TA-PEG-COOH TA-PEG-N3 TA-PEG-OCH3 TA-PEG-CPP	1.5	6.8 (for TA-PEG-CPP)	$\lambda < 650$	820	4-5;8	780 < τ < 1050	Non toxic except for PEG-CPP NCS, which start to show a slight toxicity at high concentrations.	MTT assay on African green monkey kidney COS-1 cells. ¹²⁵
His MUA [Au ₁₇ MUA ₄ -His ₂₂]	-	-	$\lambda < 450$	600		$\tau_1 = 7110$ (81.21%) $\tau_2 = 2040$ (18.79%)	Very Low	MTT assay on HeLa cells. ⁷⁴
Single apoferritin	1.2	≈ 12	400 < λ < 550	650	8.2	-	Not cytotoxic up to a concentration of 10 ⁻⁶ M in vitro	Human colorectal carcinoma cell line Caco2, human hepatoma cell line HepG2 and Mice. ³¹
GSH	2.5 ± 0.3	3.3 ± 0.4	$\lambda < 450$	810	≈ 0.5	-	-	Mice. ¹³⁴

Single BSA Au ₂₀ -BSA	≈ 2.6	-	$\lambda < 600$	620	15	$\tau_1 = 10.4$ (1.66%) $\tau_2 = 453$ (97.2%)	Not toxic	A549, Hep-2 cell lines and Mice ³³
Au ₂₈ @ Transferrine	2.6 ±0.5	≈ 12	$\lambda < 480$	710	≈ 7.7	172.6 ± 63.9	Not toxic up to a concentration of 80 μM (calculated as Au) in vitro	Hela, HepG-2, 3T3 cell lines and Mice ⁴⁷

Table 3: Features of different luminescent GNCs. In order cluster ligands/molecular formula, Gold core diameter, hydrodynamic diameter (HD d), absorption wavelengths (Abs.), emission maximum (Em. max), emission QY, luminescence lifetimes (τ), toxicity, toxicity assessment method employed and tested organism models are shown.

2 Apparent effect of nanomaterials on photoisomerization

2.1 Introduction

Photoisomerization reaction have been used to prepare photocontrollable and phototunable nanomaterials. In most cases this nanosystems have been prepared by integrating photoreactive molecules into supramolecular architectures or using them to functionalize nanoparticles or other nanostructures. This approach has been exploited to produce nanomachines and nanodevices for imaging as well as for controlled release.¹⁰ The interaction of the photoactive unite with the whole structure is fundamental both for the basic research, to understand the effect of the environment on the photoisomerization process and for the applicative point of view since it affect the actual efficiency of the final materials. Integration in nanoparticles has been often reported to cause a decrease in the photoisomerization efficiency of molecules bound to the surface.^{135,136,137,138} This effect has been typically explained as resulting from the reduced mobility experienced by the molecules.^{135,136}

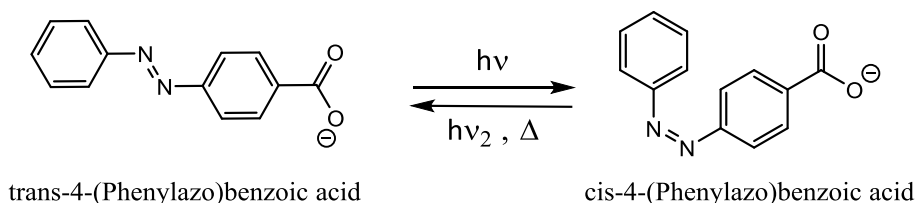
In this Chapter we will show that a significant decrease of the photoisomerization QY, of a derivative of the most widely studied photoisomerizable dye (azobenzene), is observed in the presence of nanoparticles even in the absence of an actual interaction. We will also propose a simple approach to perform quantitative measurement unaffected by this phenomenon. The results will be reported in the cases of two important examples of nanomaterials such as gold nanoparticles¹ and graphene.¹³⁹

2.2 Materials

4-(Phenylazo)benzoic acid (T) 98% has been purchased by Sigma Aldrich. TEG functionalized GNPs have been synthesized by the F. Mancin group of the University of Padova as described in ref. ¹⁴⁰ and ¹⁴¹. Graphene XGNP® grade C powder has been purchased by XG Sciences.

2.3 Photoirradiation experiments

Photoirradiation experiments have been performed in quartz cuvettes, (optical path = 1cm) with a mercury lamp and a bandpass filter to irradiate at 313 nm. 2,5 mL of azobenzene 4-(Phenylazo)benzoic acid (T) solution $4 \cdot 10^{-5}$ M, in carbonate buffer 100mM at pH 10, have been irradiated under vigorous stirring both in absence and in presence of two common nanomaterials. The first cuvette contained only T, the second contained T and TEG functionalized GNPs while the third contained T in presence of graphene. The concentration of T, in the three solutions, has been kept constant as all the other irradiation parameters. TEG functionalized GNPs concentration was $3.89 \cdot 10^{-5}$ M, corresponding to a ligand concentration of $1 \cdot 10^{-4}$ M, while graphene concentration was 13 mg/mL. Irradiation has been performed by steps of 30 seconds, and the absorbance has been measured, after each irradiation step, in correspondence of T's main absorption peak.



Scheme 1: trans-cis 4-(Phenylazo)benzoic isomerisation.

2.4 Conventional approach to PI rate determination

Azobenzene and its derivatives are molecule which contain two benzenic rings linked by an N=N double bond. They exist in equilibrium between their *trans* and *cis* forms and, most of them, in dark condition, at room temperature, are almost at 100% in their *trans* form, the most thermodynamically stable.

The *trans* isomer can be converted into the *cis* by light irradiation (Scheme 1) The reverse reaction, that already occurs spontaneously at room temperature, can be promoted by irradiating at different wavelengths or by heating. Light induced switching between these two isomers is called photoisomerization.¹⁰

For a photochemical reaction such as photoisomerization the quantum yield can be expressed as the number of reactant molecule that disappear per unit of time, divided by the photons absorbed in the same time interval. For the particular case of *Trans* to *cis* PI of azobenzene:

$$\text{Eq. 3: } \Phi = \frac{dn(T)/dt}{q_{as}}$$

Where $dn(T)/dt$ = number of *trans* azobenzene interconverted in the unit of time and q_{as} = absorbed flux of photons, defined as the number of photons absorbed in the reaction cell in the unit of time.

The amount of *trans* azobenzene still present in solution can be determined, with good approximation, by measuring the absorbance in correspondence of its main absorption peak. In fact, at such wavelength, the *cis* specie has an ϵ about one order of magnitude lower than the *trans* and, in thermal equilibrium, it is present in much lower concentration.¹⁴² For these two reasons, the *cis* form contribution to the solution absorbance, at this particular wavelength and at the begin of a

photoirradiation process, can be neglected. Thus, knowing the ϵ of the *trans* specie in correspondence of its absorption maximum and measuring the correspondent absorbance, it is possible to determine its concentration with good approximation. As the light source used in the spectrophotometer is much weaker than the source used for the irradiation, the photoisomerization triggered during the measure is quantitatively negligible.

To calculate the photoisomerization QY, it is also necessary to measure the number of photons absorbed in the reaction cell during the irradiation time. To this purpose, the absorbance of the solution at the irradiation wavelength is related to the ratio between the intensity of incident and transmitted light. When this ratio is known, the number of absorbed photons in the reaction cell at a given time (q_{as}), can be calculated if the number of photons incident on the reaction cell at the same time (q_{in}) is known. These two quantities are defined as

$$Eq. 4: \quad q_{in} = \frac{dn(p_{in})}{dt} \quad ; \quad q_{as} = \frac{dn(p_{as})}{dt}$$

The number of photons respectively incident and absorbed in the reaction cell, in the unit of time. q_{in} can be measured by actinometry as described in ref¹⁴³ and it is generally constant, as it depend just on the lamp used, the wavelength chosen, and the geometry of the irradiation set up. Contrarily, q_{as} vary as the photoisomerization occurs, and this have necessarily to be considered as described later. At every time t , q_{in} and q_{as} are related as:

$$Eq. 5: \quad q_{as} = q_{in} \times f_{as}$$

$$Eq. 6: \quad q_{as} = q_{in} \times (1 - 10^{-A})$$

Where f_{as} and A are respectively the total fraction of light absorbed and the total absorbance of the solution. If the *trans* azobenzene is the only

specie present in solution, according to the Lambert Beer law, A in the last equation can be written as

$$\text{Eq. 7: } A = \varepsilon [T] l$$

Where [T] is the concentration of the *trans* specie.

According to Eq. 5 and Eq. 6, Eq. 3 can be written as

$$\text{Eq. 8: } \Phi = \frac{dn(T)/dt}{q_{in} \times (1 - 10^{-A})}$$

which leads to the differential equation

$$\text{Eq. 9: } \frac{dn(T)}{dt} = \Phi \times q_{in} \times f_{as} = \Phi \times q_{in} \times (1 - 10^{-A})$$

During the irradiation, because of the variation of [T], also the absorbance and the absorbed light fraction change during time, thus making difficult the integration of Eq. 9 except in two limit cases. For highly concentrated ($A > 2$) or highly diluted ($A < 0,1$) solutions, the determination of photoisomerization quantum yields can be simplified by two approximations. In the first case, all of the incident light is considered to be absorbed while, in the second case, the absorbed light fraction f_{as} can be approximated by the relation $f_{as} = A \cdot \ln(10)$.

These two approximations lead to two different solutions of the Eq. 9 which are respectively.

$$\text{Eq. 10: } \Phi = ([T]_0 - [T]_t) \times \frac{V \times N_a}{q_{in} \times t}$$

$$\text{Eq. 11: } \Phi = \ln \frac{[T]_0}{[T]_t} \times \frac{V \times N_a}{2.303 \times q_{in} \times \varepsilon \times l \times t}$$

In the cases of solutions with absorbance comprised between the two listed above, if the variation of A is small and it appear to be linear, the absorbed light fraction can be approximated as constant and equal to the mean between the its values at time t and at time $t=0$.

$$\text{Eq. 12: } (f_{as})_m = \frac{(f_{as})_0 + (f_{as})_t}{2} = \frac{(1-10^{-A_0}) + (1-10^{-A_t})}{2}$$

Where $(f_{as})_0$ = mean absorbed light fraction at time 0, $(f_{as})_t$ = mean absorbed light fraction at time t, A_0 = Absorbance of the solution at time $t=0$ and A_t = Absorbance of the solution at time t.

From this approximation, the integration of Eq. 9 leads to

$$\text{Eq. 13: } \Phi \approx ([T]_0 - [T]_t) \times \frac{V \times N_a}{q_{in} \times t} \times \frac{1}{(f_{as})_m}$$

Where Φ = Photoisomerization quantum yield, $[T]_0$ = Concentration of Trans 4-(Phenylazo)benzoic acid at time 0 [mol/L⁻¹], $[T]_t$ = Concentration of Trans, 4-(Phenylazo)benzoic acid at time t [mol/L⁻¹], V = Volume of the irradiated solution [L⁻¹], N_a = Avogadro number [molecules/mol], q_{in} = Flux of incident photons on the reaction cell [number of photons/s], t = irradiation time [must have the same unit of measure used for q_{in}] and $(f_{as})_m$ = mean absorbed light fraction.

This approximation is more accurate for $t \rightarrow 0$ than for longer irradiation time, when the *cis* form absorption contribution become more relevant.

In Fig. 24 are shown the absorption spectra of T during the photoisomerization and in Fig. 25 it is shown the photoisomerization kinetic. The apparent PI QY, for successive irradiation steps, calculated according to Eq. 9, can be plotted against time and fitted by a line. The real PI QY can be extrapolated from the fitting line intercept on the y axis, which is the best estimate of the PI QY of T (Fig. 26).¹⁴⁴

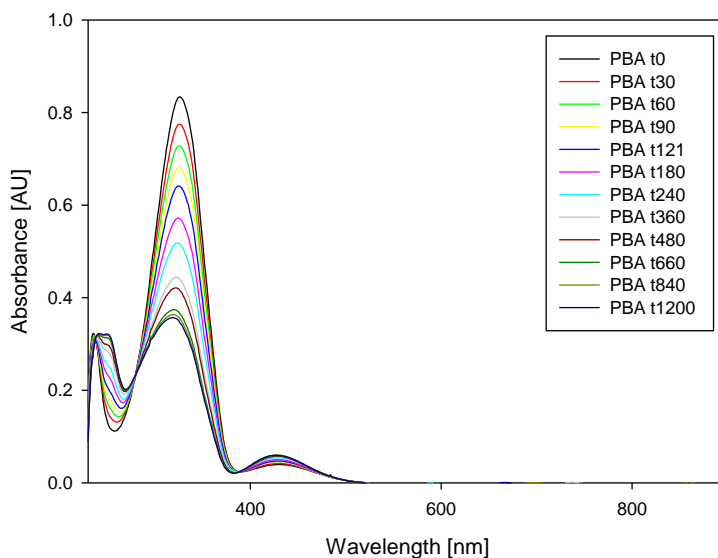


Fig. 24: 4-(Phenylazo)benzoic acid UV-Vis spectra during photoisomerization.

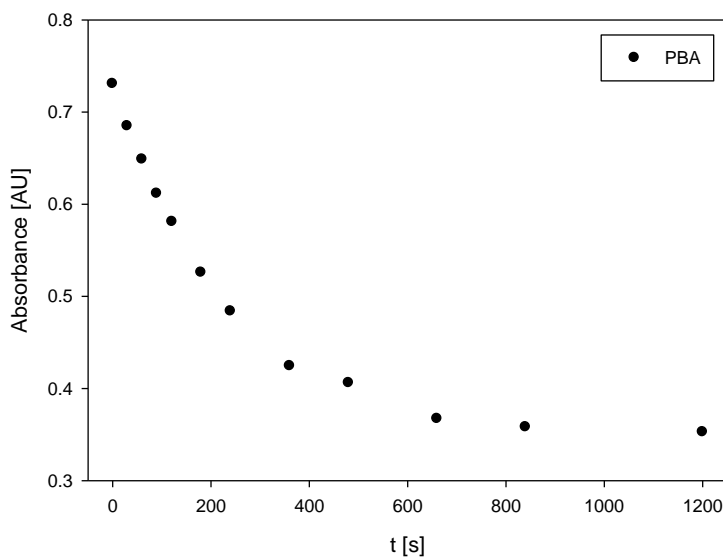


Fig. 25: 4-(Phenylazo)benzoic acid photoisomerization kinetic plotted as absorbance at 326 nm in function of time.

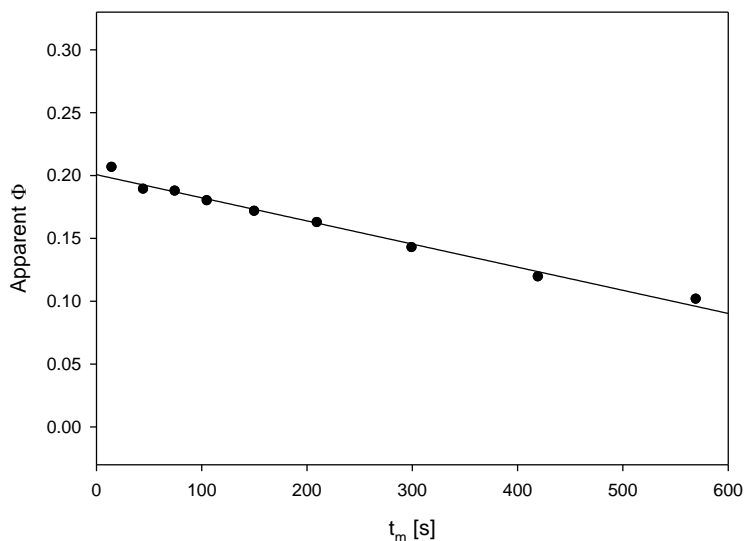


Fig. 26: Apparent photoisomerization QY of 4-(Phenylazo)benzoic acid in function of the irradiation time.

2.5 Results and discussion

In this Chapter we will demonstrate that an apparent decrease of the PI QY of azobenzene (AB) is observed in the presence of GNPs and graphene. Quantitative measures of PI QY and kinetic constants are altered when the optical effects, related to the presence of these particles in suspension, is not properly taken into consideration. To do this, we will investigate with a conventional approach the photoisomerization of the azobenzene derivative (T) which is soluble in water at pH 10 (100mM carbonate buffer) in presence and in absence of GNPs and graphene.

For a photochemical reaction such as photoisomerization, quantum yield can be expressed as the number of molecule of reactants that disappear per unit of time, divided by the photons absorbed by the sample in the same time interval. This measurement hence require the ability to measure

the concentration of the reactant at given times as well as the number of photons adsorbed by the system after each irradiation time interval. Both data are typically determined by measuring the absorbance of the solution at two different wavelengths, the former of which is the irradiation wavelength and the latter a diagnostic wavelength for the reactant (or the product). In Fig. 27 it is shown the typical setup for the PI experiment.

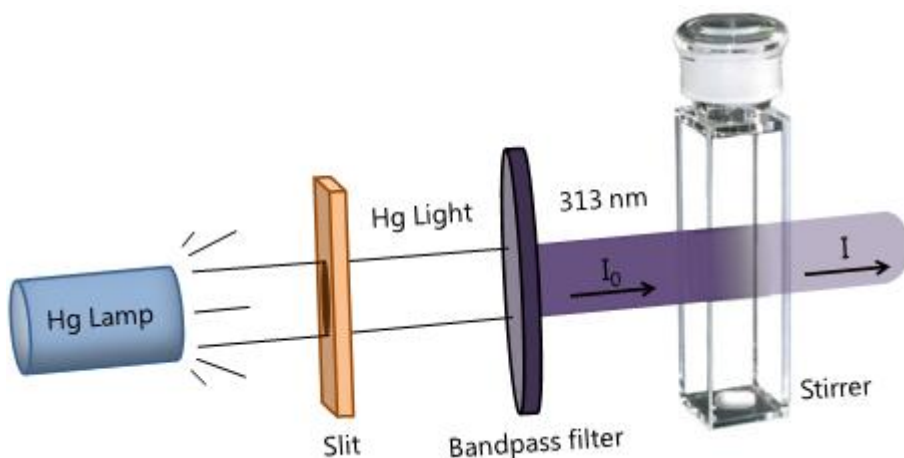


Fig. 27: Experimental irradiation set-up.

The irradiation beam (for simplicity cylindrical and monochromatic) penetrates into the solution and it is progressively attenuated. As a consequence, the photon intensity profile decreases as a function of the depth in the solution x . The decrease in intensity in a given path dx is proportional to the number of excited states formed. So if I is expressed as number of photon for time interval and s is the beam section the excited state concentration is $dl*s*dx/volume=dl$. This means that the concentration of excited state is the highest in the first layer of solution and it decreases exponentially moving along the light propagation axis. If not compensated this would cause a major formation of the product in the first layer of solution and to changes in intensity distribution along x

that would be hardly predictable. In order to avoid this, the solution is continuously stirred to guarantee its homogeneity.

Assuming hence that the concentration of all the species (with the exception of the excited states is constant in the system) the actual number of photons adsorbed per time unit can be simply determined by measuring the absorbance at the irradiation wavelength $A(\lambda_{irr})$ using Eq. 6. To this purpose it is fundamental to determine the number of photons incident on the reaction cell.

In our case, this has been done using potassium ferrioxalate as actinometer, according to the method suggested by Fisher in ref ¹⁴³, and we found an incident photon flux of $8.57 \cdot 10^{14}$ photons/s.

$$\text{Eq. 14: } q_{p,in} = \frac{\Delta A(510)}{t} \times Y(313) \times N_A$$

$$q_{p,in} = 0.0056025 \times 2.54 \times 10^{-7} \times 6.022 \times 10^{23} \\ = 8.57 \times 10^{14} \left[\frac{\text{photons}}{s} \right]$$

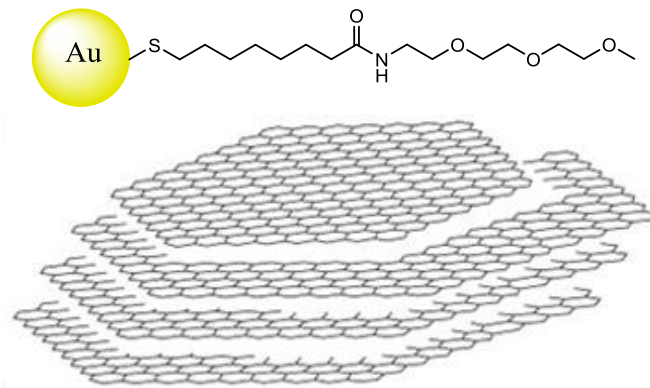


*Fig. 28: Representation of the nanomaterials employed in this study.
Top: TEG-GNPs. Bottom: XG Sciences Graphene XGNP® grade C.*

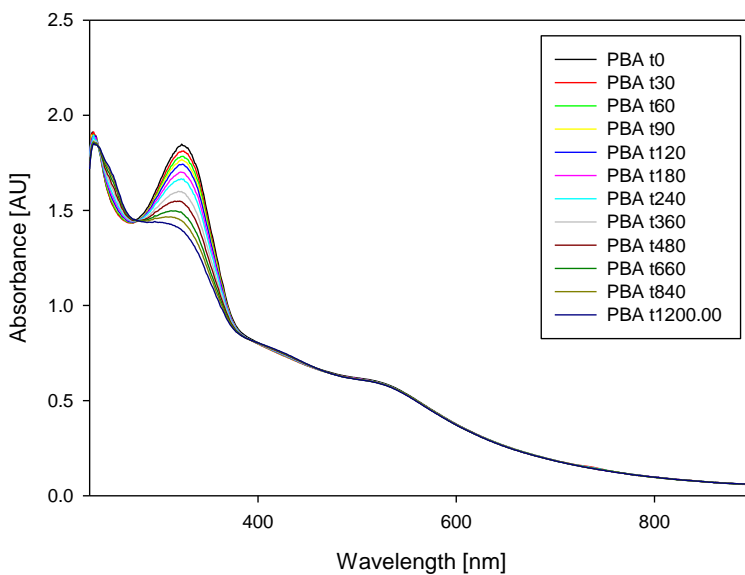


Fig. 29: 4-(Phenylazo)benzoic acid absorption spectrum in presence of TEG-GNPs during photoisomerization.

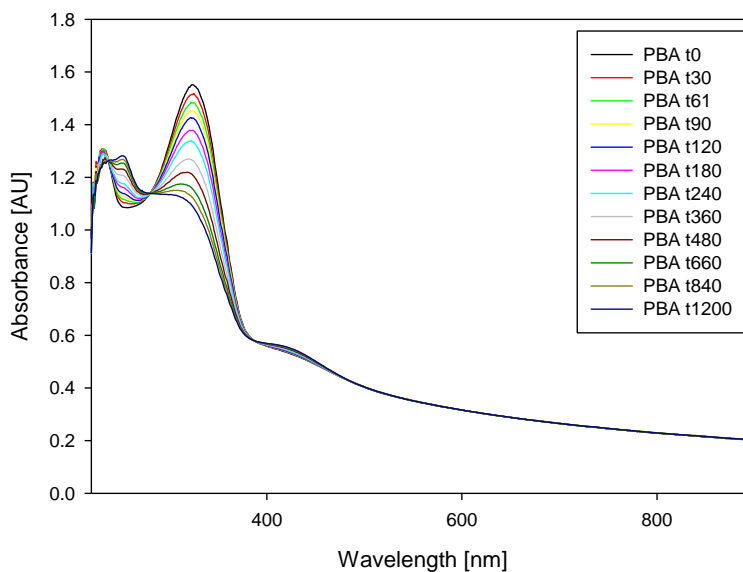


Fig. 30: 4-(Phenylazo)benzoic acid absorption spectrum in presence of graphene during photoisomerization.

Where $Y(313) = 2.54 \times 10^{-7}$ for the 313nm emission band of a common mercury lamp. Other values of Y, for different bands of common mercury lamps can be found in ref. ¹⁴⁴.

In our experiments, 4-(Phenylazo)benzoic acid (T) 4×10^{-5} M, in carbonate buffer 100mM at pH 10, has been irradiated under vigorous stirring at 313 nm using a Mercury lamp with a bandpass filter. Keeping constant the concentration of T, the experiment has been performed on T alone and in presence of TEG functionalized GNPs or Graphene. TEG functionalized GNPs concentration was 3.89×10^{-5} M corresponding to a ligand concentration of 1×10^{-4} M. Graphene concentration was 13 mg/mL.

The absorption spectra of these solutions during the photoisomerization are shown in Fig. 29 and Fig. 30. The photoisomerization kinetics in the three conditions has been compared by plotting the solution absorbance, in correspondence of T's main absorption peak, against time (Fig. 31). Kinetics seem very different resulting in an apparent variation of the photoisomerization QY of T. This phenomenon in some cases, have been attributed to the interaction between the two species and to a quenching effect of nanomaterials on photoisomerization QYs.^{135,136,137} In this study, we will prove that this phenomenon can be observed also in absence of a real interaction between the two components.

We analyzed our data employing a conventional approach for the determination of PI QYs, which has briefly been summarized in a dedicated section. The PI QYs calculated in this way are in fact significantly different between each other Fig. 32.

Above, it has been described how we calculated the flux of incident photons. The total absorbed fraction of this incident photons. at time t, is $(f_{as})_t^{Tot}$ and it can be calculated as.

$$Eq. 15: (f_{as})_t^{Tot} = (1 - 10^{-A_t^{Tot}}).$$

Where A_t^{Tot} = total absorbance of the solution at the time t.

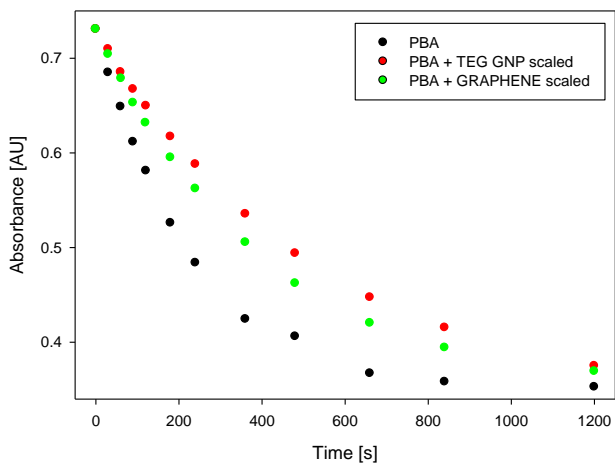


Fig. 31: Photoisomerization kinetics of 4-(Phenylazo)benzoic acid alone (black) and in presence of TEG-GNPs (red) and graphene (green) Points represent the solution absorbance at 326 nm in function of the irradiation time ($\lambda_{ecc} = 313$ nm). The last two spectra have been scaled to superimpose the all the first absorbance values.

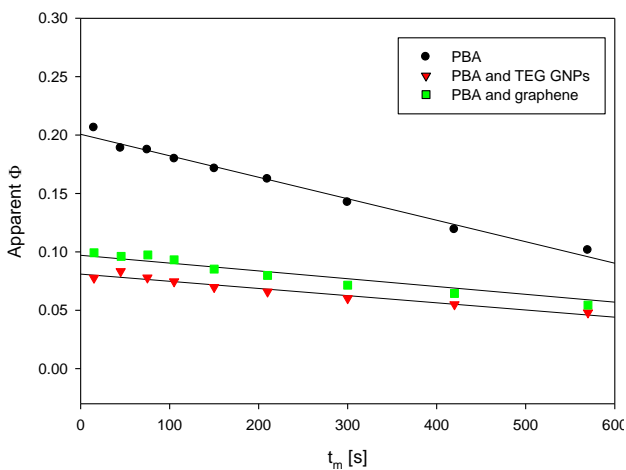


Fig. 32: Apparent photoisomerization QYs of 4-(Phenylazo)benzoic acid alone (black) and in presence of TEG-GNPs (red) and graphene (green), in function of the irradiation time, calculated with the conventional approach.

	PBA	PBA and TEG-GNP	PBA and Graphene
Φ	0.20 ± 0.01	0.08 ± 0.004	0.10 ± 0.005
r^2	0.99	0.98	0.99

Table 4: photoisomerization QYs (Φ) of 4-(Phenylazo)benzoic acid (PBA) alone and in presence of TEG-GNPs and graphene. QYs have been calculated as the intercepts of the apparent QYs plot (Fig. 32) obtained using the conventional approach outlined in Section 2.4.

For a correct data analysis, it should be considered that only a part of the absorbed light fraction is effectively experienced by T, while the remaining part interacts with the nanomaterial.

To determine the flux of photons absorbed by T (q_{as}^T), Eq. 5 becomes:

$$\text{Eq. 16: } q_{as}^T = q_{in} \times f_{as}^T$$

In presence of multiple species, according to the Lambert Beer law, for a given wavelength the absorbance of the solution in function of the depth x is:

$$\text{Eq. 17: } A = \sum_{i=1}^N A_i = \sum_{i=1}^N \varepsilon_i \int_0^l c_i(x) dx$$

Where N = number of species in solution, ε = molar absorption coefficient at the given wavelength, c = concentration, l = light beam optical path length inside the solution.

This means that, for two species, the contribution to the solution absorbance, of each infinitesimal segment Δx , is equal to the sum of the absorbances of the two single components in the same segment (the absorbance of the single components depend only on the product of its ε and its concentration in the particular segment).

Thus, for each Δx , the ratio between the absorbance of one component and the total absorbance of the segment is simply given by $A_1/(A_1+A_2)$. In our case, the concentration of all species has been kept homogeneous during the irradiation. Consequently, the total fraction of light absorbed at time t by the solution $(f_{as})_t^{Tot}$ can be directly weighted on the absorbances at the same time, to obtain the corresponding fraction of light exclusively absorbed by T, $(f_{as})_t^T$:

$$Eq. 18: (f_{as})_t^T = \frac{A_t^T}{A_t^T + A^{Other}} \times (f_{as})_t^{Tot}$$

Where A_t^T = absorbance of T at the time t and at the irradiation wavelength [AU]. A^{Other} = absorbance of the other species except T (nanomaterials), at the time t and at the irradiation wavelength [AU] and $(f_{as})_t^{Tot}$ = fraction of light absorbed by the solution at the time t .

If the nanomaterial contribution to the solution absorbance A^{Other} remains constant during the irradiation, all the values in eq. 16 can be determined: A^{Other} is directly measured using an equal solution but where T is absent, A_t^T is determined as $A_t^T = A_t^{Tot} - A_t^{Other}$ and A_t^{Tot} is directly measured during the experiment.

After these considerations, if with T, other species are present in solution, and these can contribute to the total absorbance at the irradiation wavelength (without changing their contribution during the irradiation) Eq. 13 must be expressed as

$$Eq. 19: \Phi \approx ([T]_0 - [T]_t) \times \frac{V \times N_a}{q_{in} \times t} \times \frac{1}{(f_{as})_m^T}$$

If the nanomaterial does not change its absorbance contribution neither at

the diagnostic wavelength, as in our case, Eq. 19 can be written as

$$\text{Eq. 20: } \Phi \approx \frac{A_0^T - A_t^T}{\varepsilon^T} \times \frac{V \times N_a}{t \times q_{in}} \times \frac{1}{(f_{as})_m^T}$$

Where A_t^T = absorbance of T at the diagnostic wavelength and at the time t, A_0^T = absorbance of T at the diagnostic wavelength and at the time t = 0, ε^T = molar absorption coefficient of T at the diagnostic wavelength, $(f_{as})_m^T$ = mean absorbed light fraction exclusively by Trans 4-(Phenylazo)benzoic acid at λ_{irr} and ε^T = molar absorption coefficient of T at the same wavelength used to measure $A_{(t)}^T$ [$\text{mol}^{-1}\text{cm}^{-1}$].

Where the value of $(f_{as})_m^{Azob}$ can be calculated as

$$\text{Eq. 21: } (f_{as})_{m,t}^T = \frac{(f_{as})_0^T + (f_{as})_t^T}{2}$$

Where $(f_{as})_0^T$ = absorbed light fraction exclusively by Trans 4-(Phenylazo)benzoic acid at time t=0 and $(f_{as})_t^T$ = absorbed light fraction exclusively by Trans 4-(Phenylazo)benzoic acid at time t.

The approach developed in this work is a simple experimental and mathematical method to correct the apparent decrease in PI QYs caused by the presence in solution of common nanomaterials such as graphene and GNPs.

By measuring the absorbance contribution of the single components and then applying the mathematical procedure illustrated above, the data presented in Fig. 32 and Table 4 have been corrected as shown in Fig. 33 and Table 5:

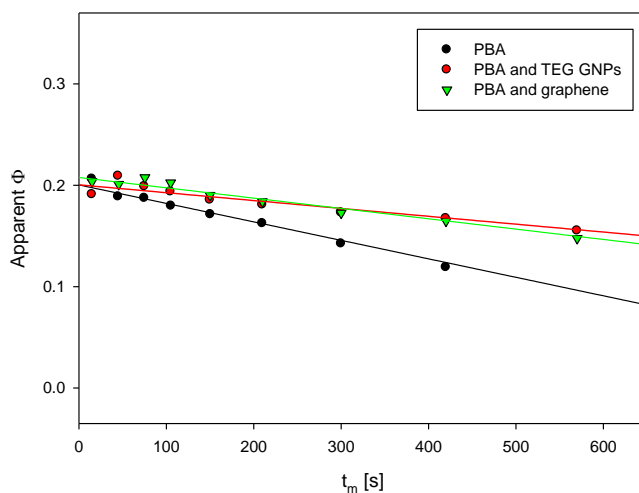


Fig. 33: corrected apparent photoisomerization QY of 4-(Phenylazo)benzoic acid alone (black) and in presence of TEG-GNPs (red) and graphene (green), in function of the irradiation time.

	PBA	PBA and TEG GNP	PBA and Graphene
Φ	0.20 ± 0.01	0.20 ± 0.01	0.21 ± 0.01
r^2	0.99	0.98	0.99

Table 5: corrected photoisomerization QYs (Φ) of 4-(Phenylazo)benzoic acid (PBA) alone and in presence of TEG-GNPs and graphene. QYs have been calculated as the intercepts of the corrected apparent QYs plot (Fig. 33).

The corrected results show that there are no significant differences between the $t \rightarrow c$ PI QY of our azobenzene derivative, in presence and in absence of these nanospecies.

This indicates that the photoswitching efficiency, in the considered cases, is not altered by interaction of the dye with the nanomaterial and that the initially observed variations were just apparent.

2.6 Conclusions

In this study, we proved that the presence of two common nanomaterials in solutions cause a significant apparent effect on the trans to cis PI kinetics and QY of an azobenzene derivative. We proved that also in absence of real interactions between the two species, the apparent decrease on PI efficiency is observed anyway, just because of the optical effects caused by the nanomaterials presence.

We developed an experimental and mathematical method to properly consider this optical effect, determining the flux of photons effectively absorbed by the photoswitchable dye. As our procedure allows to exclude the nanomaterial optical effect, it consists in a valuable and simple method to quantify changes in PI QYs resulting from real interactions of the solutions components. The combination of photoswitchable actuators and nanomaterials has aroused great interest in the last years, due to the potentialities of these systems in fields as sensing, memory storing, nanomachines, energy conversion, optoelectronic, super-resolution microscopy, photo-controlled drug-release, photo-controlled nanomaterials aggregation and many others... For all of these application fields and for basic research, the quantitative assessment of the photo-actuator efficiency on nanostructures it is of fundamental importance.

Considering that this method relies just on photophysical considerations, it is clear that it is not restricted to the specific chemistry of the species employed in this work. Thus, at least in principle, it could be applied also to a huge variety of azobenzene derivatives and nanomaterials for which the assumptions of this method are valid as well.

3 Effects on photoisomerization caused by interactions with nanomaterials

3.1 Introduction

Photoswitchable dyes have often been combined to supramolecular or nanostructures for several different purposes as, for example, to create photocontrollable nanomachines^{12,13} phototunable membrane ions channels¹⁴ or devices for light triggered drug release.¹⁵ The study of the photoactuator efficiency, when it is combined with nanostructures, is thus of paramount importance for the study and the design of such complex light driven systems.

The aim of this study is to assess the effects on *trans* 4-(Phenylazo)benzoic acid (T) PI QYs caused by its interaction with different nanomaterials. We employed $\approx 1,8$ nm GNPs, functionalized with three different ligands whose different affinity for T has been proven by NMR.

We will show that the conventional approach discussed in Section 2.4 is ineffective in probing PI QYs changes resulting from the interaction with GNPs. Then we will apply the correction method outlined in the same section to obtain the real PI QYs in order to assess possible effects induced by actual interactions.

In absence of chemical reactions except photoisomerization, the affinity of T for the particular monolayer is governed by non-covalent interaction, such as the association of hydrophobic segments and net opposite charges.

3.2 Materials

GNPs were synthesized by the F. Mancin group of the University of Padova as described in ref. ¹⁴⁰ and ¹⁴¹ starting from $\text{HAuCl}_4 \cdot 3\text{H}_2\text{O}$.

N,N,N-trimethyl-8-(methylthio)octan-1-ammonium (Am), 11-(methylthio) undecyl (2-(trimethylammonio)ethyl) phosphate (ZW) and N-(2-(2-(2-methoxyethoxy)ethoxy)ethyl)-8-(methylthio)octanamide (TEG) were synthesized by the same group as described in ref. ¹⁴⁰ and ¹⁴¹. $\text{HAuCl}_4 \cdot 3\text{H}_2\text{O}$ and 4-(Phenylazo)benzoic acid (T) has been purchased by Sigma Aldrich.

3.3 Photoirradiation and NMR experiments

For the determination of PI QYs, photoirradiation experiments have been performed in quartz cuvettes (optical path =1 cm) with a mercury lamp and a bandpass filter to irradiate at 313 nm. 2,5 mL of azobenzene 4-(Phenylazo)benzoic acid (T) solution $4 \cdot 10^{-5}$ M, in carbonate buffer 100mM at pH 10, have been irradiated under vigorous stirring both in absence and in presence of GNPs. The first cuvette contained only T, while the other three contained T in presence of TEG-amide, Zwitterion, and ammonium functionalized GNPs respectively (TEG-GNPs, ZW-GNPs and Am-GNPs) (Scheme 2). The concentration of T, in the three solutions, has been kept constant as all the other irradiation parameters. GNPs concentration has been chosen to keep constant the concentration of their ligands at $1 \cdot 10^{-4}$ M. Ligands concentrations have been determined by thermogravimetric analysis (TGA) (Fig. 36, Fig. 40 and Fig. 44). T and GNPs have been mixed in dark condition and experiments have been performed after one hour to wait the establishment of a repartition equilibrium of the dye in GNPs ligands monolayer.

3.4 Results and discussion

Azobenzene derivatives are the most studied class of photoisomerizable dyes. Their photoswitching between the *trans* and the *cis* forms determines a change in their conformation, the actuation of mechanical work and changes in its chemical-physical properties. For example the dipole moment of azobenzene switches from 0 D to 3 D after its photoisomerization to the *cis* form⁹ (Fig. 34¹¹).

Compared to simple azobenzene, the derivative T used in this work has an improved water solubility in both its isomeric forms because of the carboxylate substituents that bear a net negative charge in the experimental alkaline pH conditions. However, also in the case of our compound, the *trans* isomer is less polar than the *cis* and it is only moderately soluble in water at pH 10 (up to ≈ 4 mM). The *trans* isomer has thus a higher affinity for hydrophobic phases if compared to the *cis* which is more soluble in water.

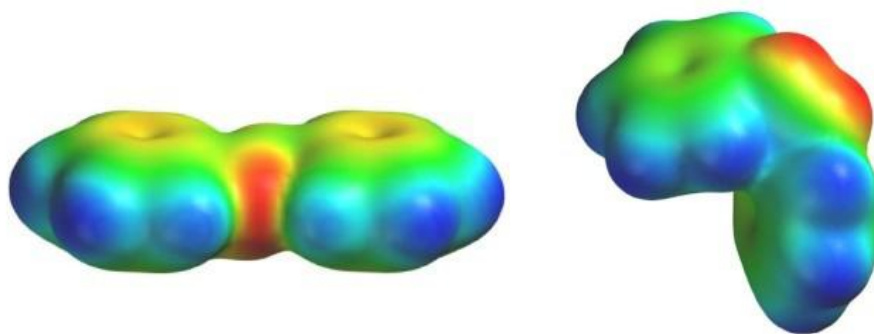


Fig. 34: Structures of *trans* and *cis* isomers of azobenzene. Spacefilling models are coloured by electrostatic potential (red—negative to blue—positive).

We studied the interaction of T with three different kinds of GNPs stabilized with monolayers that contained all a similar hydrophobic portion. As a difference the monolayers of the different particles terminated with different hydrophilic polar groups that conferred to particles adequate water solubility. The three kinds of hydrophilic groups were characterized by the absence of net charge (TEG), a zwitterionic charge distribution (ZW) and a positive charge (Am) respectively.

The repartition of the azobenzene derivative in a GNP monolayer, before and after its photoisomerization can be determined by NMR spectroscopy. Depending on the intensity of the monolayer-dye interaction this can be done, for example, using two complementary NMR techniques: the application of a diffusion filter or the NOE pumping.^{140,141}

For different monolayers, as the magnitude of the interaction between molecule and monolayer increases, the mean residence time of the molecule on the particle increases as well. In the case of very strong, non covalent interactions the mean residence time can be so long that the diffusion coefficient of the molecule starts to be comparable to that of the particles. When this happens, the NMR spectra of the slow diffusing molecules become selectively visible after the application of a diffusion filter. By designing particles monolayers to obtain selective affinities, this phenomenon has been exploited for the specific sensing and resolution of particular species in complex mixtures.^{140,141}

The NOE pumping technique allows to detect molecules close to the particles monolayer also if the interaction is not strong enough to modify the molecules diffusion coefficient. The NOE pumping experiment consists in the application of a diffusion filter to dephase (cancel) signals of slow diffusing species, then a NOE experiment is started immediately after the diffusion filter. In this phase the magnetization can be transferred from the monolayer of the slow diffusing particles to molecules in its close proximity in a fast exchange regime. NOE effect intensity is proportional to $1/R^6$, implying that the magnetization can be transferred only in the range of few Ångström. The higher is the interaction between molecule and nanoparticles, the stronger will be the signal detected in the NOE

pumping experiment. Long residence times are not required for NOE effect to happen, so that it can also be used to probe weak interactions,^{140,141} for which diffusion coefficient changes are generally not observed.¹⁴⁵

Cis and *trans* azobenzene have very different NMR spectra that can be easily distinguished (Fig. 47). Thus, combining the NMR techniques briefly sketched above, it is possible to assess the repartition of both isomeric forms between the solution and the GNP monolayer (Fig. 48, Fig. 49 and Fig. 50). Samples have been irradiated for 30 min at 313 nm as described in the experimental section.

GNPs characterization is shown from Fig. 35 to Fig. 47:

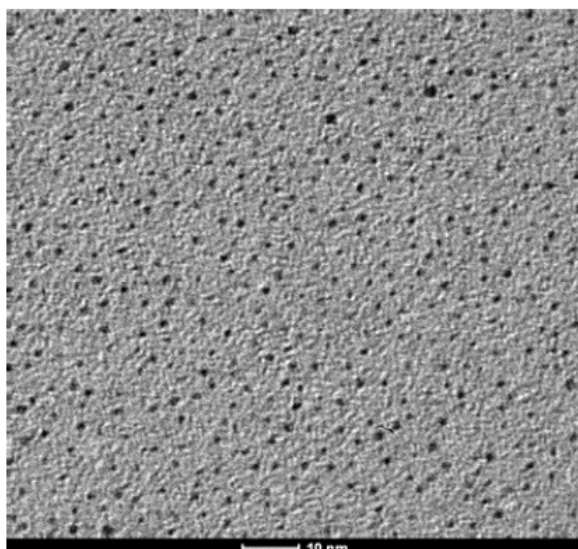


Fig. 35: Am-GNPs TEM image. mean diameter: 1.6 ± 0.2 nm.

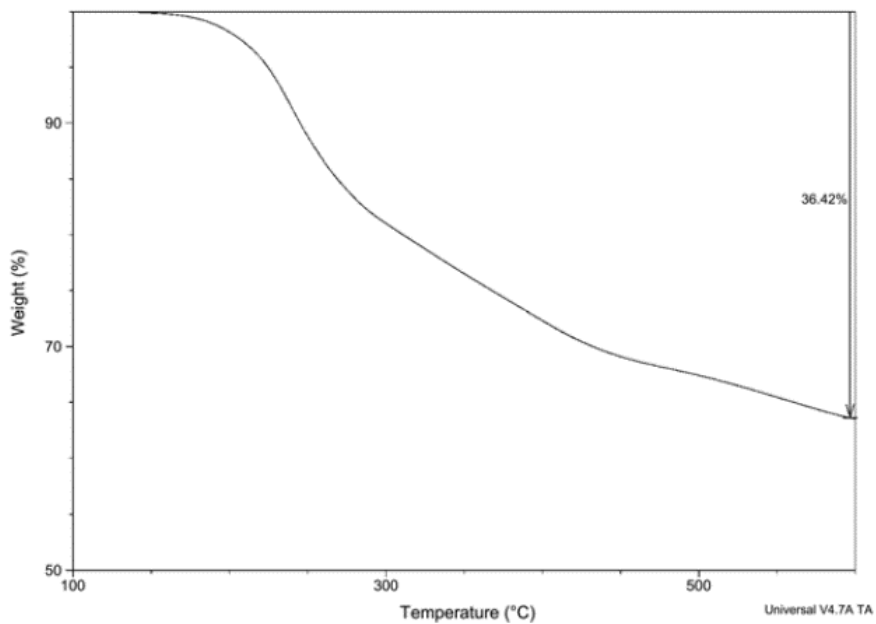


Fig. 36: Am-GNPs TGA analysis, sample acquired in air atmosphere.
Weight loss: 36.42%.

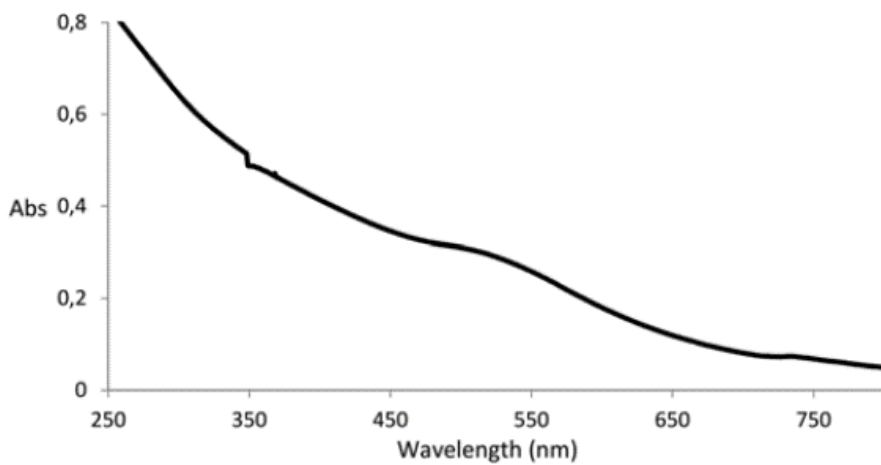


Fig. 37: Am-GNPs UV-Vis spectra, 0.1 mg/mL in water.

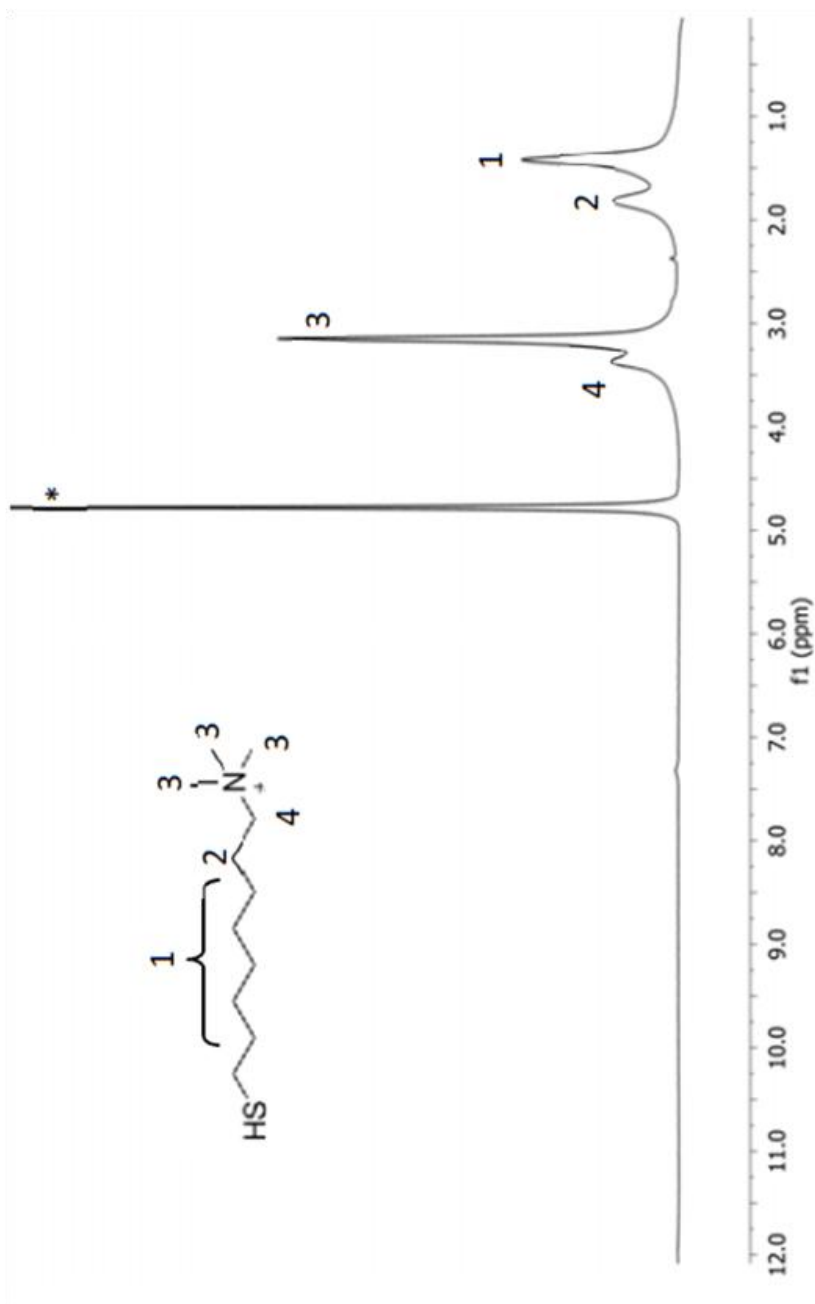


Fig. 38: Am-GNPs $^1\text{H-NMR}$ spectra in D_2O .

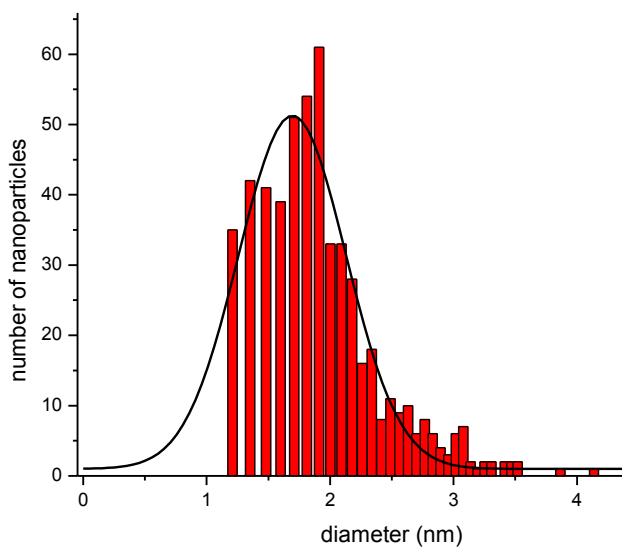
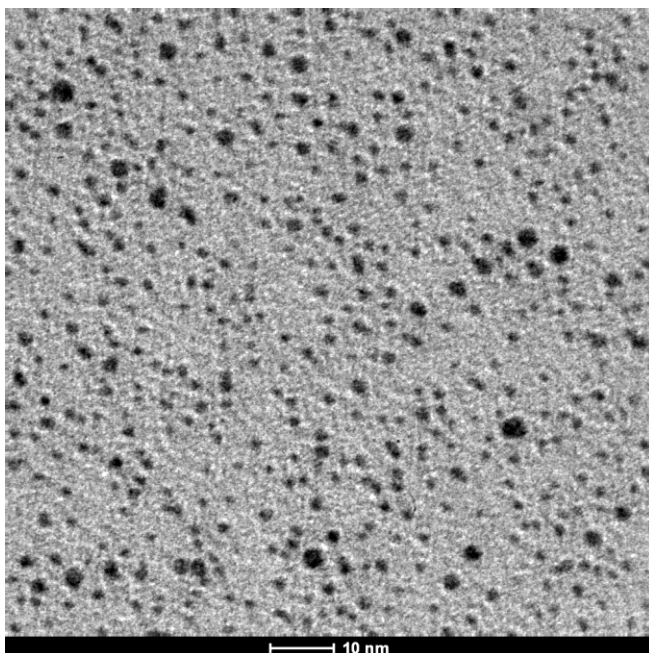


Fig. 39: ZW-GNPs TEM image (top) and size distribution plot (bottom);
mean diameter: 1.7 ± 0.4 .

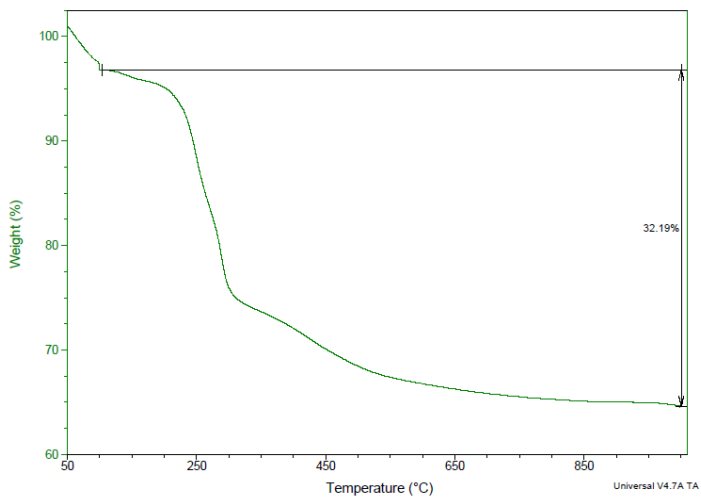


Fig. 40: ZW-GNPs TGA analysis, sample acquired in air atmosphere.
Weight loss: 32.19%.

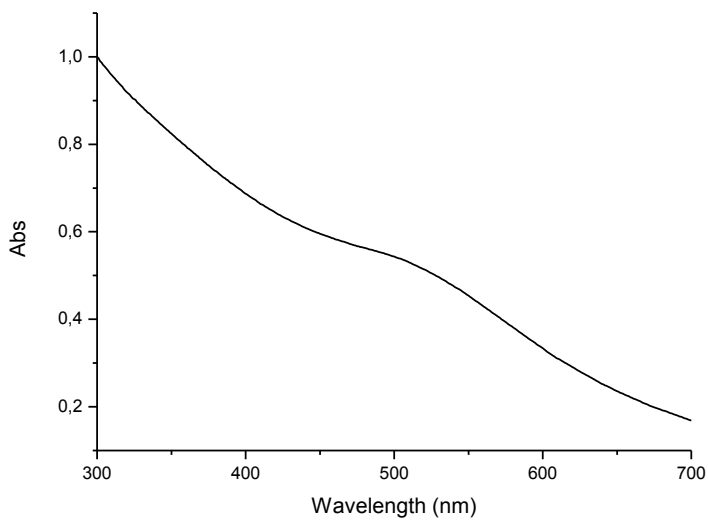


Fig. 41: ZW-GNPs UV-Vis spectra, 0.1 mg/mL in water.

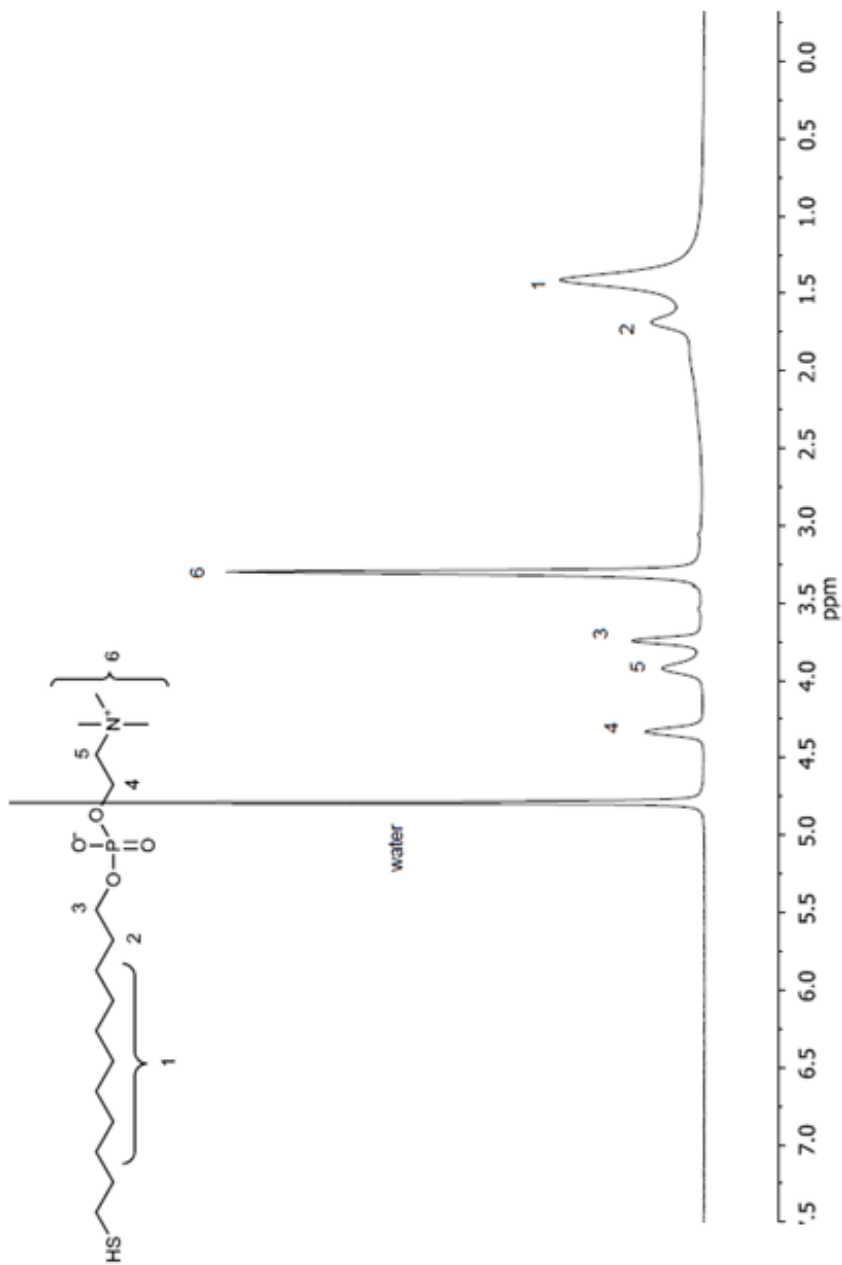


Fig. 42: ZW-GNPs $^1\text{H-NMR}$ spectra in CDCl_3 .

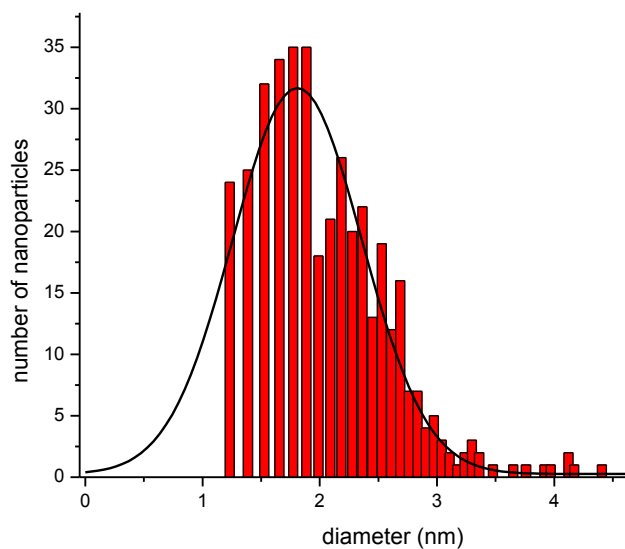
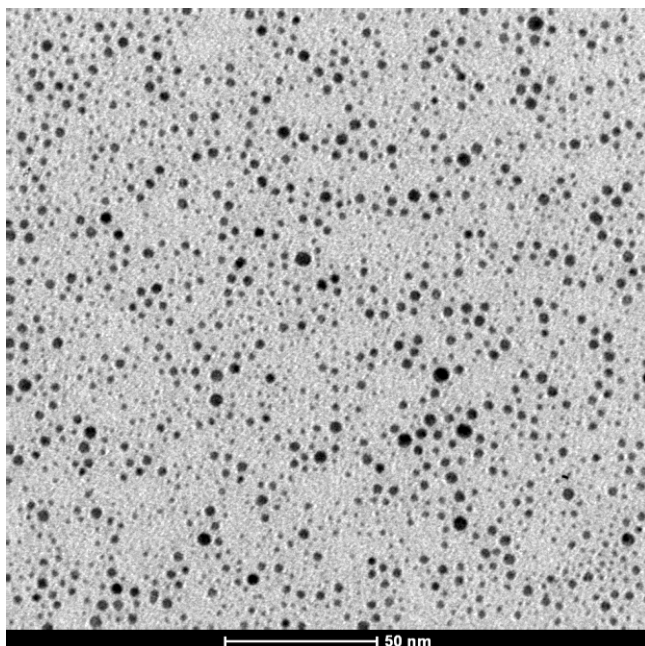


Fig. 43: TEG-GNPs TEM image (top) and size distribution plot (bottom); mean diameter 1.8 ± 0.5 nm.

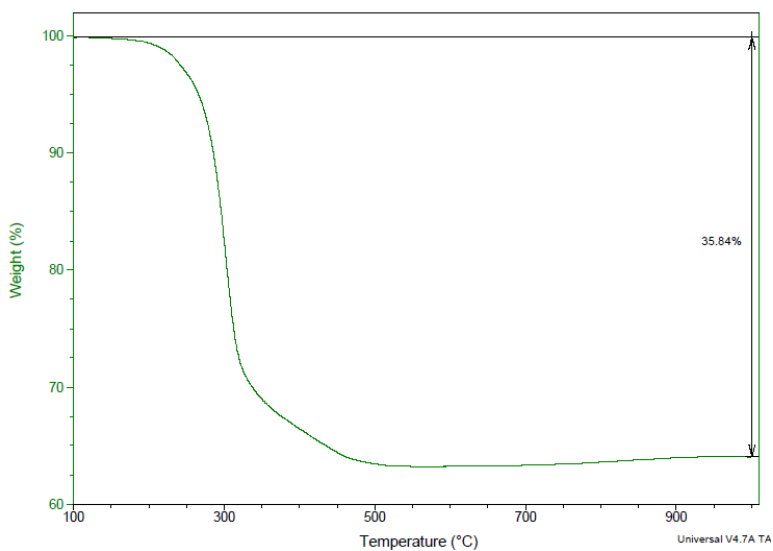


Fig. 44: TEG-GNPs TGA analysis, sample acquired in air atmosphere. Weight loss: 35.84 %.

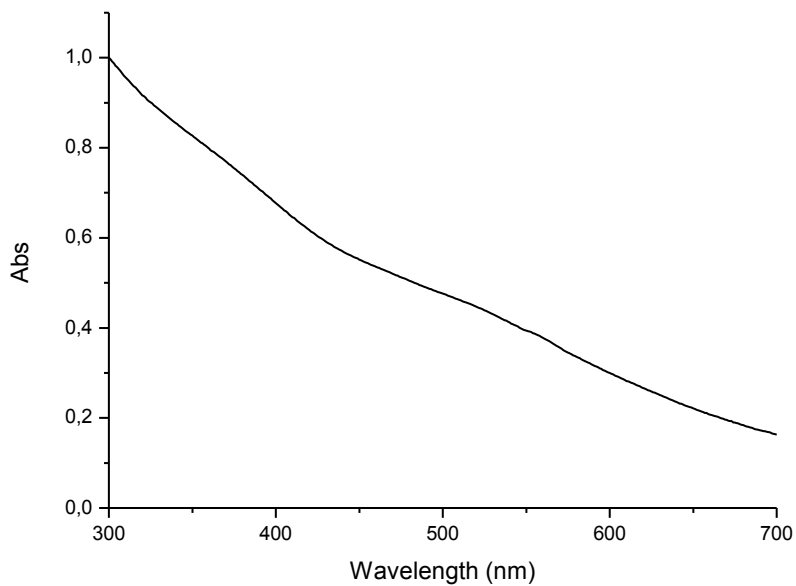


Fig. 45: TEG-GNPs UV-Vis spectra, 0.1 mg/mL in water.

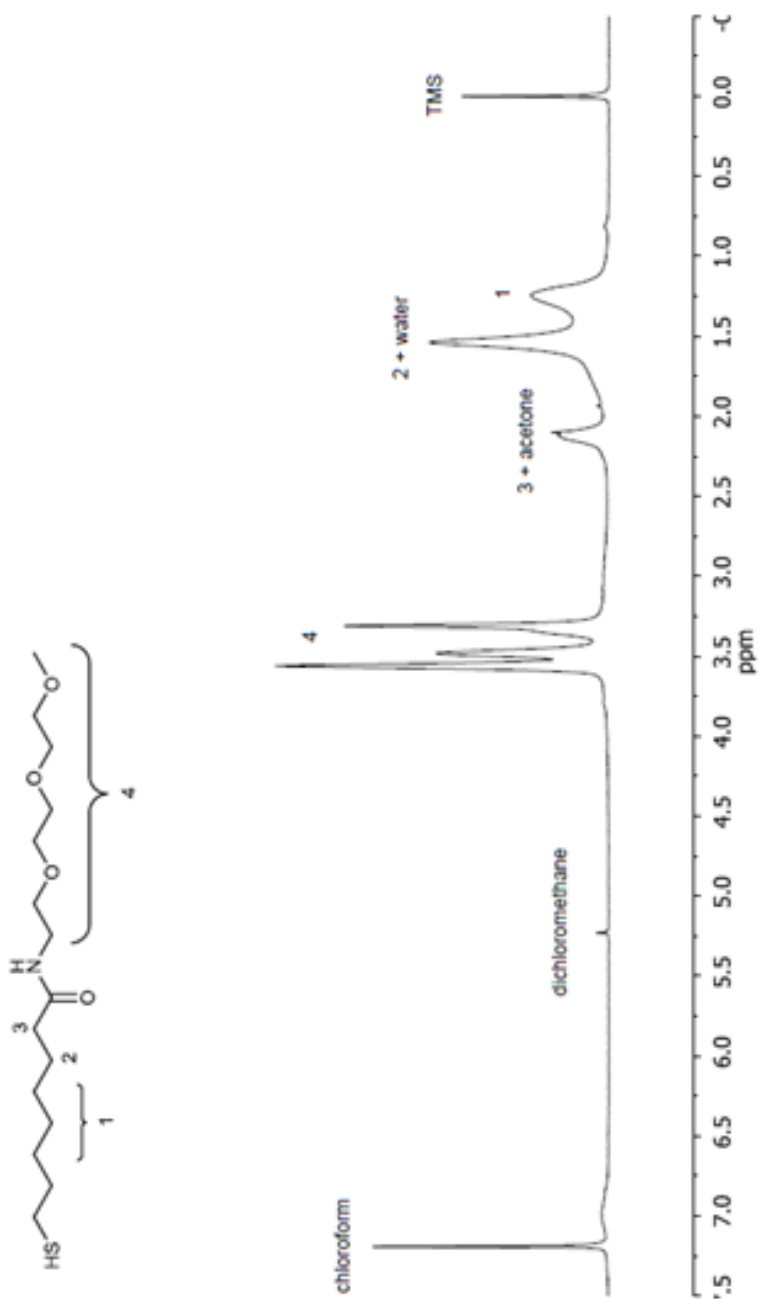


Fig. 46: TEG-GNPs $^1\text{H-NMR}$ spectra in CDCl_3 .

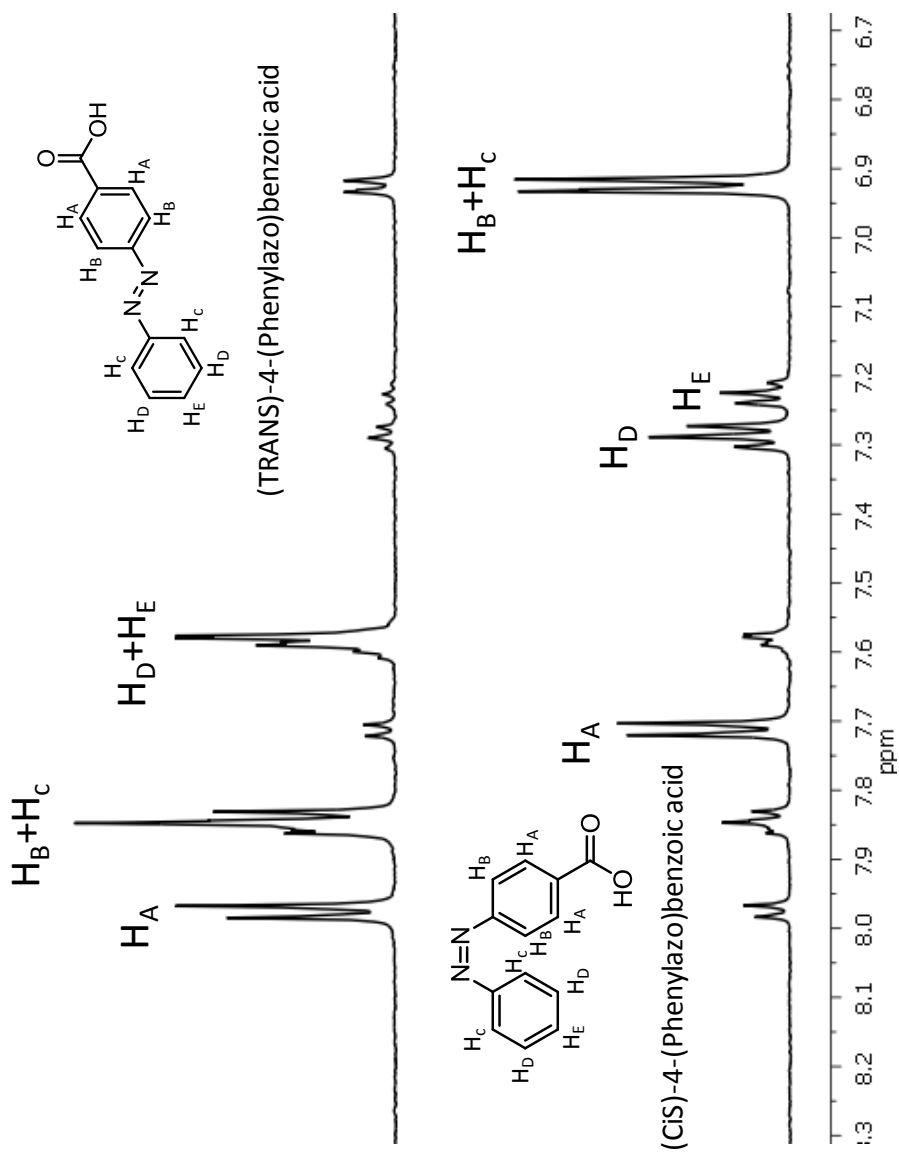


Fig. 47: 1H -NMR spectra of *trans* (top) and *cis* (bottom) 4-(Phenylazo)benzoic acid.

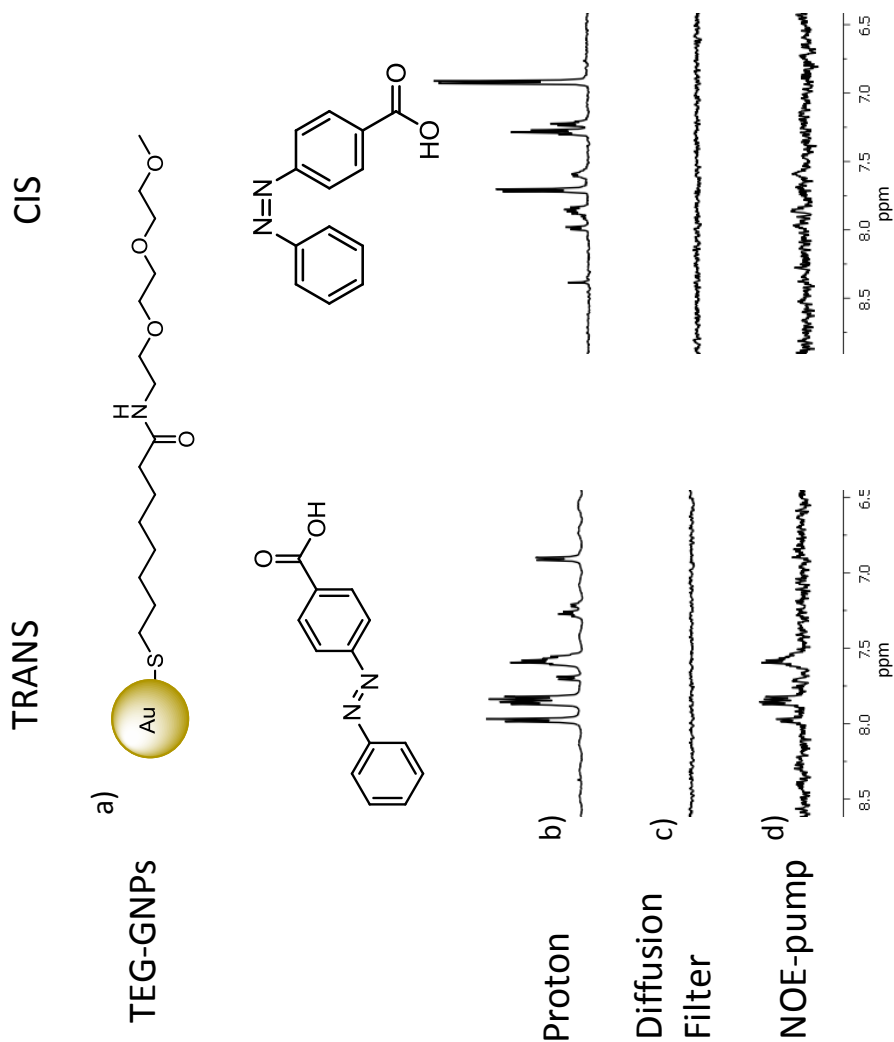


Fig. 48: a) scheme of TEG-GNPs (top) and trans-cis 4-(Phenylazo) benzoic acid (bottom) structures. b) $^1\text{H-NMR}$ spectra of 4-(Phenylazo)benzoic in presence of TEG-GNPs before (left) and after (right) 30 min of irradiation at 313 nm. c) $^1\text{H-NMR}$ spectra of the same solutions with the application of a diffusion filter. d) NOE pumping $^1\text{H-NMR}$ spectra of the same solutions.

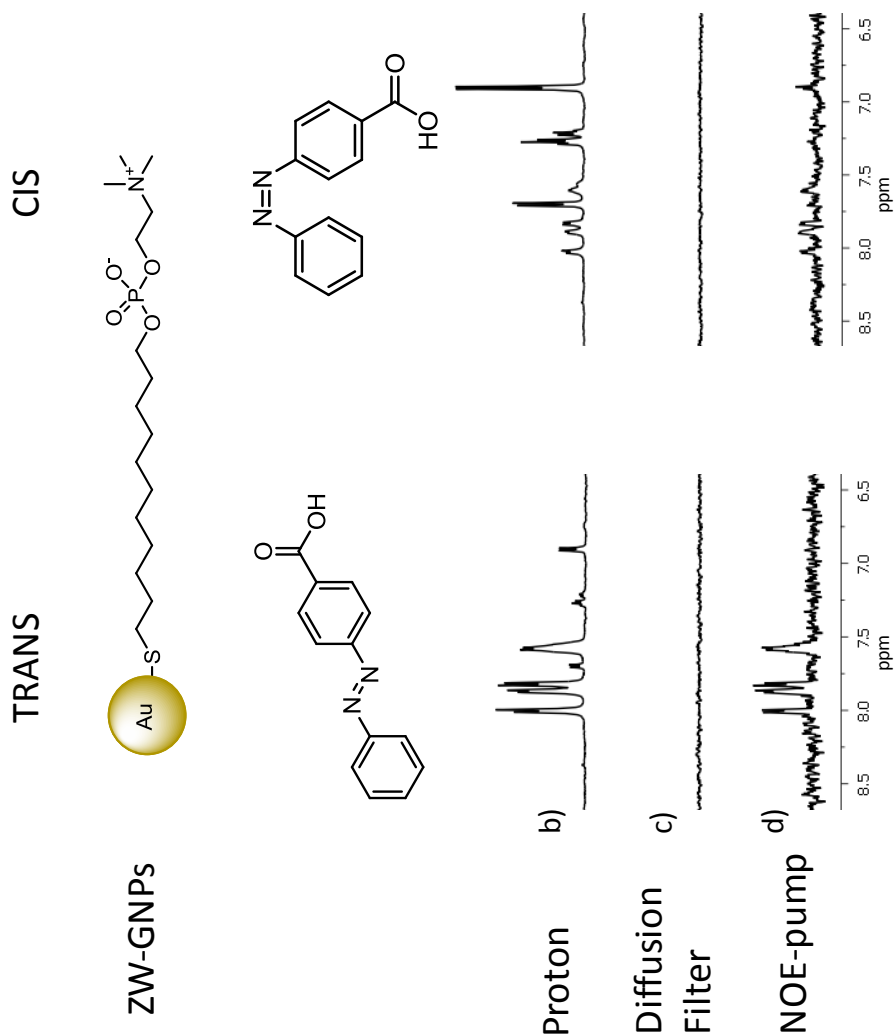


Fig. 49: a) scheme of ZW-GNPs (top) and trans-cis 4-(Phenylazo) benzoic acid (bottom) structures. b) ¹H-NMR spectra of 4-(Phenylazo)benzoic in presence of ZW-GNPs before (left) and after (right) 30 min of irradiation at 313 nm. c) ¹H-NMR spectra of the same solutions with the application of a diffusion filter. d) NOE pumping ¹H-NMR spectra of the same solutions.

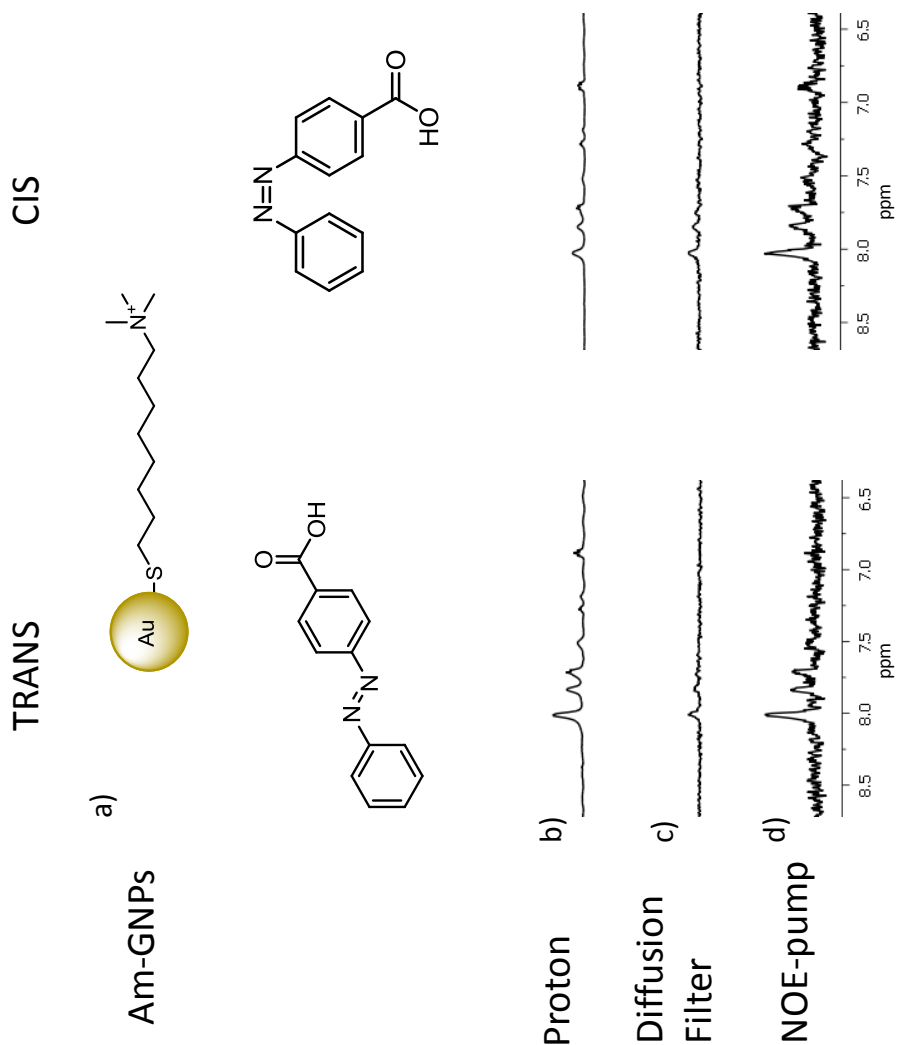


Fig. 50: a) scheme of Am-GNPs (top) and trans-cis 4-(Phenylazo) benzoic acid (bottom) structures. b) ¹H-NMR spectra of 4-(Phenylazo)benzoic in presence of Am-GNPs before (left) and after (right) 30 min of irradiation at 313 nm. c) ¹H-NMR spectra of the same solutions with the application of a diffusion filter. d) NOE pumping ¹H-NMR spectra of the same solutions.

NMR results in Fig. 48, Fig. 49 and Fig. 50 clearly underline a different affinity of T for the different monolayers. In the case of TEG-GNPs, T's simple proton NMR spectra is unaffected by the presence of the metallic nucleus. However the NOE pumping experiment reveals that exist a repartition equilibrium of the *trans* isomer inside the monolayer. The flat spectrum resulting from the application of the diffusion filter, indicates that this interaction is not sufficiently strong to modify T's diffusion coefficient. The simple proton spectra, performed after 30 minutes of irradiation, reveals that T reaches the photostationary point within this time (the relative intensities of the *cis/trans* peaks are the same observed for the photostationary point of T alone).

In the case of ZW-GNPs the situation is substantially unchanged except for slight differences observed in the NOE pumping spectra. Before the photoisomerization T's peaks are slightly higher and their traces can be observed also after the irradiation. These differences indicate a slightly higher affinity of T for ZW-GNPs' monolayer.

Regard Am-GNPs, the simple proton spectra line broadening is sufficient to reveal the strong association between T and the particles.^{146,147} Moreover, the *trans* isomer spectrum is still visible using the diffusion filter, before and even after the irradiation. This demonstrates that the interaction of the two components is so strong that the diffusion coefficient of the molecule becomes comparable to that of the particle. After 30 min of irradiation the system does not reach the photostationary point, accounting for a reduction of the PI QY of T ascribable to the strong interaction. The evaluation of the relative intensities of *cis/trans* peaks in the proton spectra indicate that only the $\approx 20\%$ of T interconverted into the *cis* isomer, while in normal condition the conversion is $\approx 80\%$. NOE pumping experiments confirmed the results obtained with the diffusion filter.

In all three cases as the *trans* form photoisomerizes in the *cis*, it exits from the monolayer because of the different affinity and repartition coefficient of the two isomers.

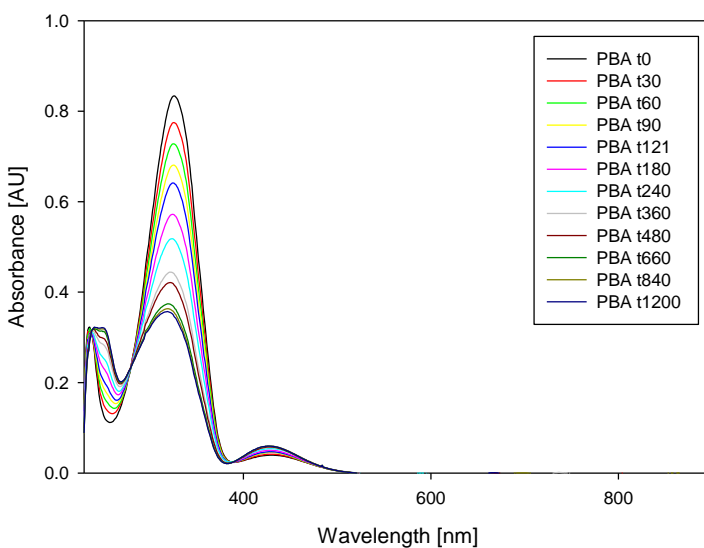


Fig. 51: Absorption spectra of 4-(Phenylazo)benzoic acid during photoisomerization.

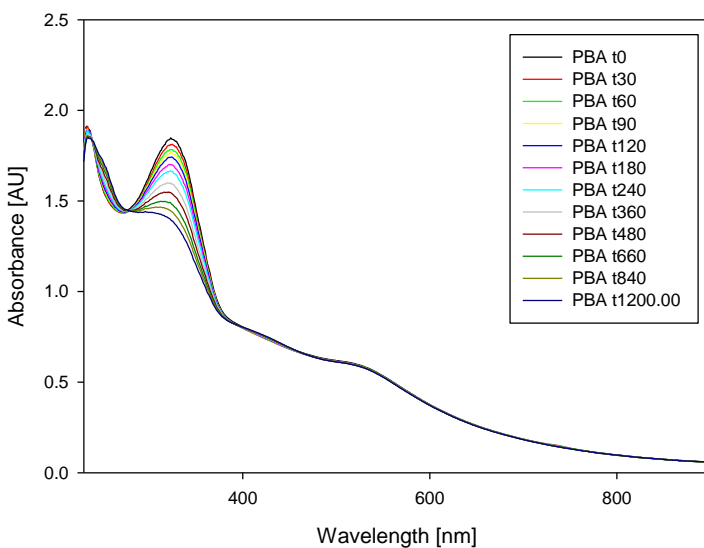


Fig. 52: Absorption spectra of 4-(Phenylazo)benzoic acid during photoisomerization in presence of TEG-GNP.

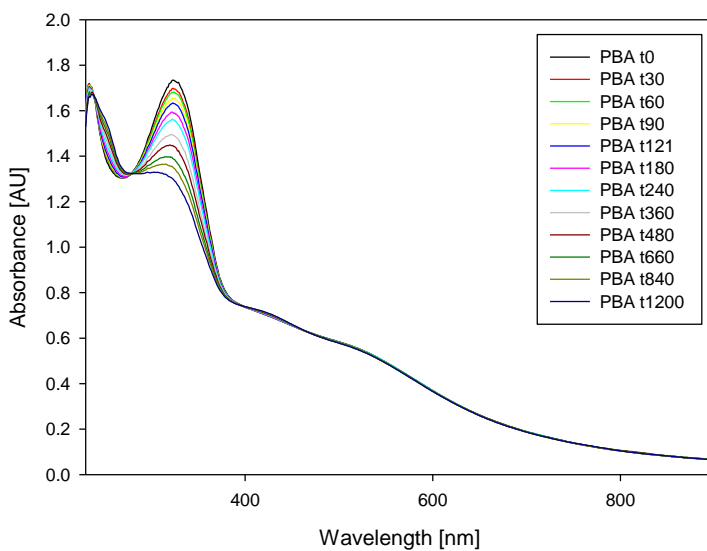


Fig. 53: Absorption spectra of 4-(Phenylazo)benzoic acid during photoisomerization in presence of ZW-GNP.

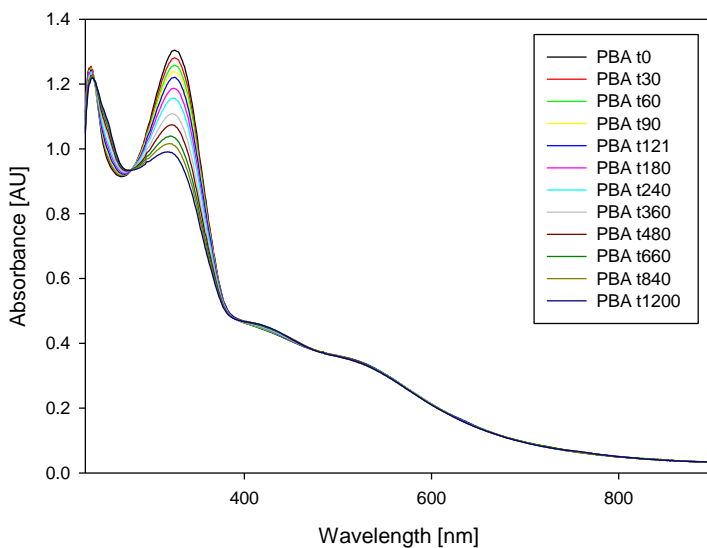


Fig. 54: Absorption spectra of 4-(Phenylazo)benzoic acid during photoisomerization in presence of Am-GNP.

The stronger affinity of T for Am functionalized GNPs compared to the other two, is probably due to the cooperation of hydrophobic and net charge interactions, which is absent in the other cases.

Once probed the interactions between the photoswitchable dye and the different nanoparticles, we measured the effect that these interactions have on the PI efficiency of T. NMR techniques require relatively high concentration so that samples were almost black solution with excessively high absorbance for spectrophotometric analysis. For this reason photochemical measures of PI QYs have been performed with concentrations of all species ten times lower than that used in NMR experiments.

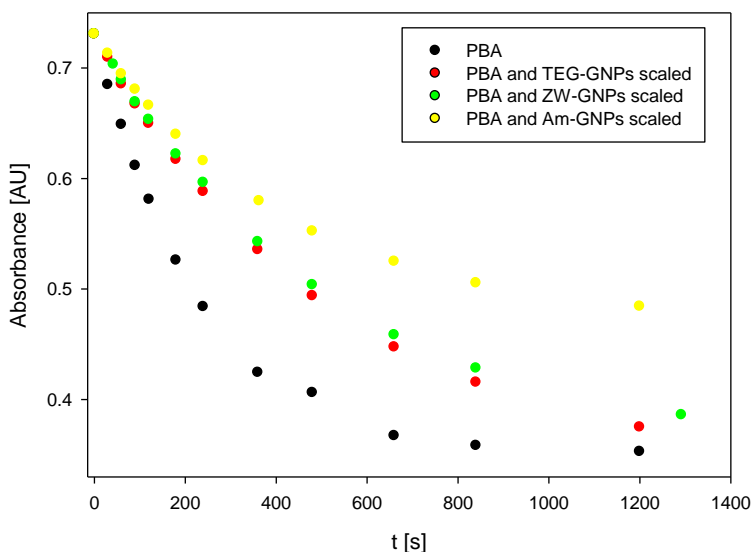


Fig. 55: Photoisomerization kinetics of 4-(Phenylazo)benzoic acid alone (black) and in presence of TEG-GNPs (red), ZW-GNPs (green) and Am-GNP (yellow). Points represent the solution absorbance at 326 nm in function of the irradiation time ($\lambda_{ecc} = 313$ nm). The last three spectra have been scaled to superimpose all the first absorbance values.

Solutions absorption spectra during the irradiation have been recorded and are shown from Fig. 51 to Fig. 54. Fig. 55 shows the apparent photoisomerization kinetics, affected by the optical filtering effect of the nanomaterials, scaled to superimpose their first absorbance value. We applied the conventional approach for the determination of PI QYs discussed in Section 2.4 confirming that it is not suitable for quantitative analysis in presence of nanomaterials (Fig. 56).

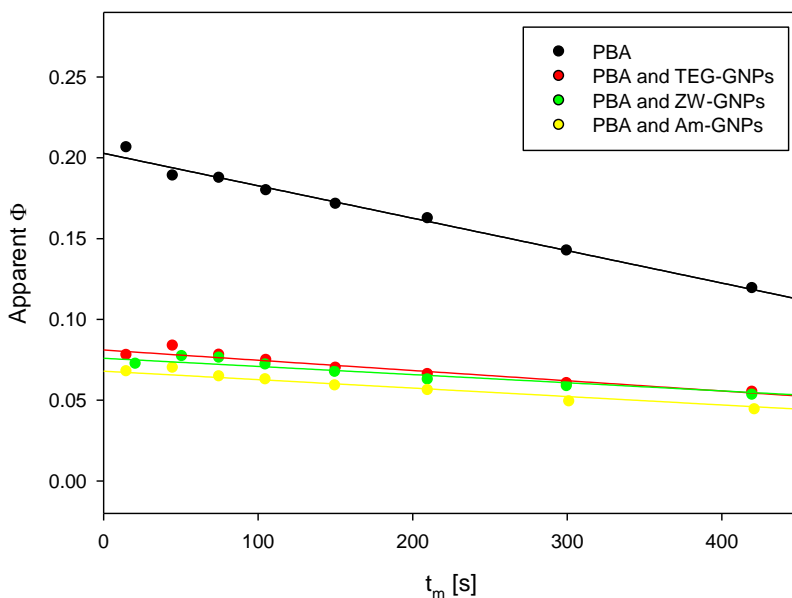


Fig. 56: Apparent photoisomerization QYs of 4-(Phenylazo)benzoic acid alone, (black) in presence of TEG-GNPs, (red) ZW-GNPs (green) and Am-GNP (yellow) in function of the irradiation time, calculated according to the conventional approach discussed in Section 2.4.

Data, analyzed according to such a model, show no significant differences between T's PI efficiency in presence of the different particles. Moreover they show as PI QYs decrease of about 2/3 in presence of every kind of particles.

	PBA	PBA and TEG-GNP	PBA and ZW-GNPs	PBA and Am-GNPs
Φ	0.20 ± 0.01	0.08 ± 0.01	0.08 ± 0.01	0.07 ± 0.01
r^2	0.99	0.98	0.96	0.98

Table 6: photoisomerization QYs (Φ) of 4-(Phenylazo)benzoic acid (PBA) alone, (black) in presence of TEG-GNPs, (red) ZW-GNPs (green) and Am-GNP (yellow), QYs have been calculated as the intercepts of the apparent QYs plot.

In order to take into account properly the nanomaterial optical contribution we applied the correction method discussed in Section 2.5 (Fig. 57).

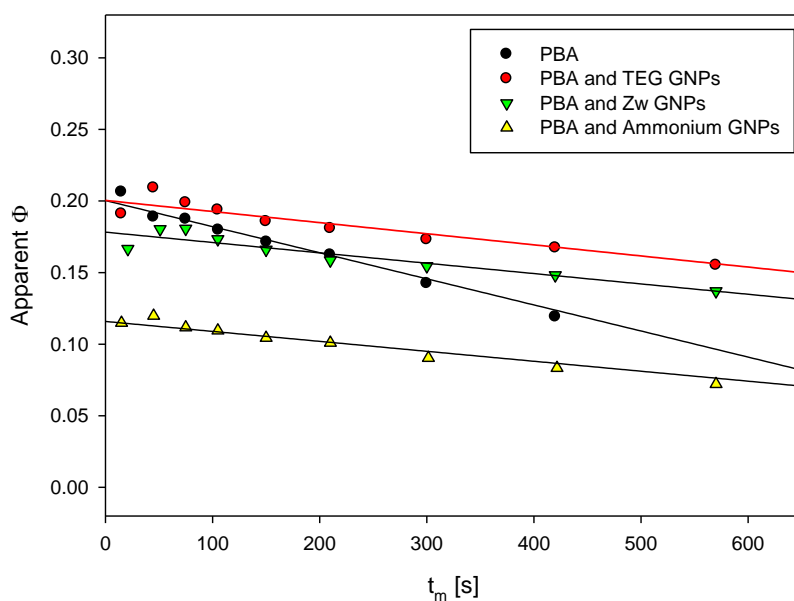


Fig. 57: corrected apparent photoisomerization QY of 4-(Phenylazo)benzoic acid alone, (black) in presence of TEG-GNPs, (red) ZW-GNPs (green) and Am-GNP (yellow), in function of the irradiation time.

	PBA	PBA and TEG-GNPs	PBA and ZW-GNPs	PBA and Am-GNPs
Φ	0.20 ± 0.01	0.20 ± 0.01	0.18 ± 0.01	0.011
r^2	0.99	0.98	0.96	0.98

Table 7: corrected photoisomerization QYs (Φ) of 4-(Phenylazo)benzoic acid (PBA) alone, (black) in presence of TEG-GNPs, (red) ZW-GNPs (green) and Am-GNP (yellow), QYs have been calculated as the intercepts of the corrected apparent QYs plot (Fig. 57).

After the correction, the apparent PI QYs plot change significantly, demonstrating that large part of the differences highlighted by the conventional approach are due to optical fostering effects rather than to chemical interactions (Fig. 56 vs. Fig. 57 and Table 6 vs. Table 7).

Corrected data show a decrease of T PI QY of the 0%, 10% and 45% in the presence of TEG, ZW and Am functionalized GNPs respectively (Table 7).

The unaltered PI efficiency in presence of TEG-GNPs is consistent with the very weak interaction previously measured, and the slight QY decrease, observed in presence of ZW-GNPs, is in accordance with the slightly higher affinity underlined by NOE pumping experiments. Also the reduction of the 45% of T PI efficiency observed in presence of Am-GNPs is in good agreement with the strong interaction measured by NMR.

For Am-GNPs, the slowing down effect on T PI exerted by this strongly interacting monolayer seems to be higher when measured by NMR if compared to spectrophotometry. In fact, photochemical measurements predict a T PI rate reduction of the $\approx 45\%$, while NMR measures reveal a reduction of at least the 75%. This discrepancy is probably due to the ten time higher concentrations used in NMR experiments, which is likely to promote a higher degree of association between the two components.

However a precise quantitative comparison of the results obtained with the two techniques cannot be performed, because of the intrinsic limitations of the two methods and the different concentrations employed.

3.5 Conclusions

In this work we proved that the conventional approach discussed in Section 2.4 is ineffective in measuring PI QYs variations caused by the interactions of dyes with nanomaterials. We confirmed that the unsuitability of this method it is due to the strong optical absorbance of the nanomaterial which significantly alters PI kinetics and QYs calculations. By applying the correction method discussed in Section 2.5 we have taken into account this optical contribution, proving that real effects on dyes PI efficiency can be observed in presence of differently functionalized particles. We found that the variation of PI QY was qualitatively proportional to the NMR measured affinity of the dye for the specific monolayer, even at one order of magnitude higher dilution. We proved that nanomaterials weakly interacting with a photoswitchable dye can have no effects on its PI, except for their optical filtering contribution. We also proved that the presence of strongly interacting nanomaterials can induce significant decreases in dyes PI QYs even halving them.

Considering the recent interest in the fabrication of photocontrollable nanodevices and machines, through the combination of photoswitchable dyes with nanomaterials, we developed a method to evaluate dyes PI efficiencies in presence of nanospecies. We proved that this is an effective method to evaluate photoactuator efficiency changes induced by their interaction with nanostructures. This has been demonstrated in the case of very weak, weak and strong non covalent interactions.

We hope our results will be helpful in the future design and efficiency evaluation of photocontrollable nanosystems.

4 Photoswitchable NIR emitting Gold nanoparticles

4.1 Introduction

Stimuli-responsive nanoparticles (NPs) are attracting great attention for their application in biology and medicine. Multifunctional NPs suitable as luminescent contrast agents for imaging^{148,149} as well as triggerable vectors for the delivery of therapeutic cargos can be engineered.¹⁵⁰ Light stimulation offers several advantages with respect to other controls since it is poorly invasive and it can be easily focussed on specific target area with sub-micrometric resolution. Moreover, light stimulation can be used to track the NPs themselves being, in particular, NIR emissive materials advantageous for *in-vivo* application.

Photo-isomerization of azobenzene (AB)¹⁰ has been widely exploited to control and tune the properties of materials.¹⁵¹ A variety of hybrid nano-system that conjugate the unique optical and electronic properties of gold nanoparticles (GNPs) to the photochemical activity of AB have been developed both for applicative and research purposes.^{17, 152} Nevertheless the possibility of switching the NIR luminescence of GNPs upon photo-isomerization of surface bound AB units has never been demonstrated before.¹⁵³

Here we report the photophysical and photochemical properties of a newly synthesized class of luminescent GNP stabilized with the AB containing thiolate *tA* (*tA*-GNPs) (Scheme 3) and we demonstrate that upon excitation of the ligand in its *trans* form sensitized NIR emission of the GNP is observed thanks to an efficient energy transfer (ET) process, a process never reported before.

Thanks to ET, the NIR luminescence of GNPs can be switched ON/OFF by alternating UV to blue irradiation. We also demonstrate that this ET process can be used to detect the isomerization state of the nanoparticles (NPs) by ratiometric detection of the NIR luminescence (upon dual excitation). Ratiometric detection offers several advantages with respect to single wavelength detection, including concentration independent response. Hence our results are very promising in view of the development of new materials for the photo-activated release of therapeutic cargos for biomedical applications. Exploiting this approach, in principle NIR signal can be used simultaneously to track the particles in the target tissues and to check, in real time the response of the NPs to light stimulation and hence their therapeutic activity.

4.2 Materials and experimental procedures

Azobenzene derivative functionalized GNPs have been synthesized by the research group of Professor F. Mancin, of the University of Padova. Materials, instrumentation and experimental procedures are described below and in Section 7. Irradiated GNPs concentration have been chosen in order have a ligand concentration of 2×10^{-4} M.

4.3 Results and discussion

TEM analysis of *tA* small nanoparticles (Fig. 58) yields an average particle diameter of 1.4 ± 0.6 nm. Formula for *tA*-GNPs, calculated on the basis of TEM diameter and TGA analysis (Fig. 59) is $\text{Au}_{85}\text{RS}_{36}$, in agreement with the $\text{Au}_{80}\text{RS}_{38}$ calculated by Murray and co-workers for nanoparticles with a diameter of 1,30 nm using a truncated octahedron shape⁸⁴.

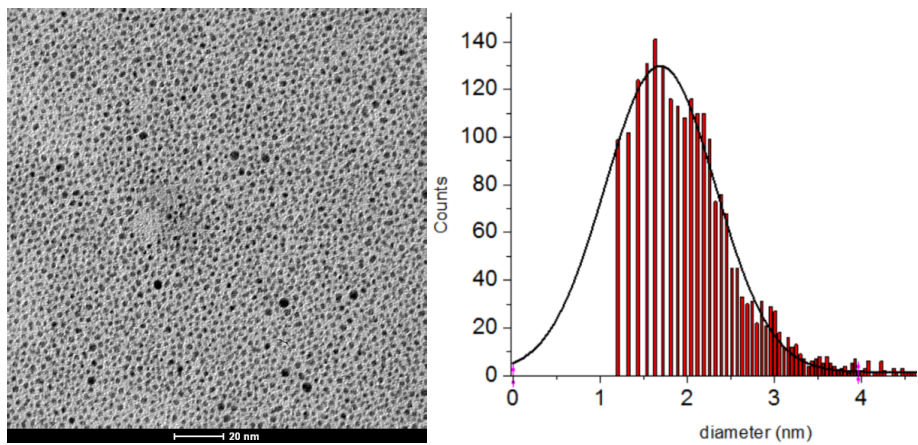


*Fig. 58: Sample TEM image of tA-GNPs and size distribution.
Average diameter = 1.4 nm ($\sigma = 0.6$ nm).*

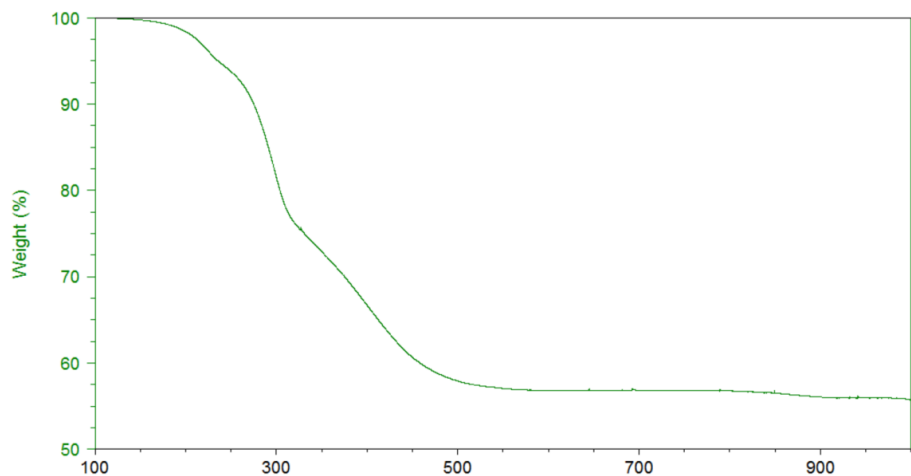


Fig. 59: TGA analysis of a sample of tA-GNPs under air atmosphere.

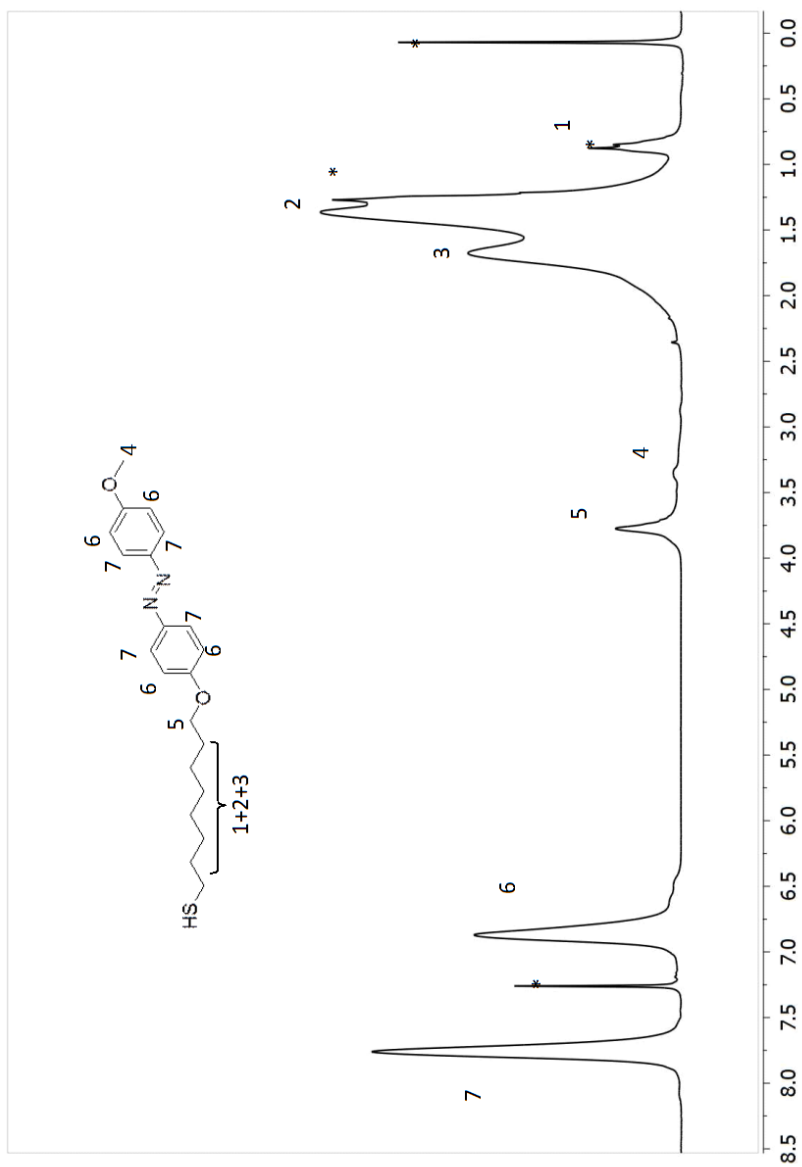


Fig. 60: ¹H-NMR (300 MHz) spectrum of the tA-GNPs in CDCl₃ (* indicates the residual solvents and impurities).

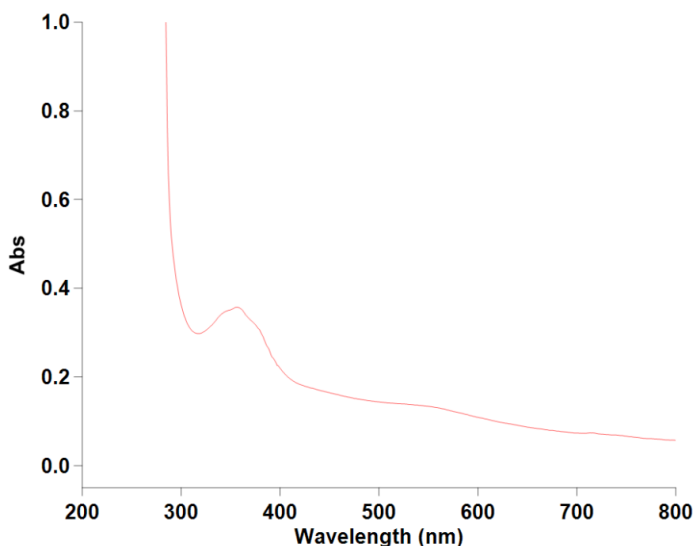
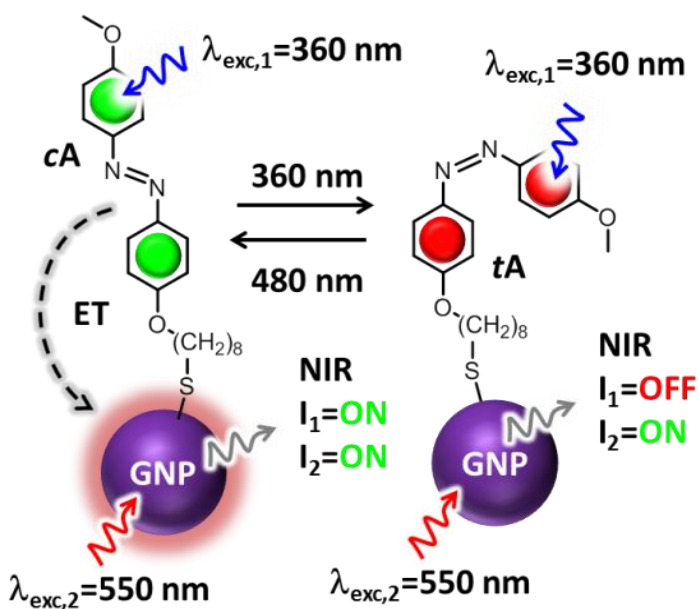


Fig. 61: UV spectrum of the *tA*-GNPs in toluene.

NMR analysis (Fig. 60) indicates monolayer formation (broadening of all signals), as confirmed by diffusion-filtered experiments (not shown).

The thermodynamically stable *trans* isomer of the A ligand (*tA*) shows the typical absorption band with maximum at 360 nm and $\epsilon = 2.7 \cdot 10^4 \text{ M}^{-1} \text{ cm}^{-1}$. Upon irradiation of a CHCl_3 solution of *tA* at 360 nm a gradual decrease of the absorbance at such a wavelength is observed as reported for similar molecules because of photo-isomerization. In particular when the photo-stationary state is reached the absorbance at 360 nm is decreased and it becomes about the 5% of the one measured before irradiation. This allowed us to conclude that almost complete $t \rightarrow c$ conversion occurs at the photo-stationary state (see below) and that the molar absorption coefficient of *cA* at 360 nm is negligible with respect to the one of *tA*.



Scheme 3: Chemical formula of the *trans* azobenzene tA and of its *cis* isomer cA bound to GNPs. When the ligands are in the *trans* form (left, tA-GNP, ON state) energy transfer from tA to the GNP leads to NIR emission upon ligands excitation. Energy transfer from cA covered NPs (right, cA-GNP, OFF state) is ineffective. The switching occurs upon irradiation with UV/Vis light.

The absorption spectra recorded at different irradiation times show two isosbestic points at 320 nm and 429 nm that demonstrated that only two species, namely tA and cA are present in solution and no side photo-products are formed upon irradiation. In particular the absorption spectrum at the photo-stationary state can be for simplicity attributed to cA: it shows two peaks at 314 nm and 448 nm ($\epsilon = 1.0 \times 10^4\text{ M}^{-1}\text{cm}^{-1}$ and $\epsilon = 3.0 \times 10^3\text{ M}^{-1}\text{cm}^{-1}$ respectively). The measured photo-isomerization quantum yield was $\Phi_{t-c} = 0.25$ in accordance with analogous AB derivatives. No fluorescence was observed either for tA (upon excitation 360 nm) or for cA ($\lambda_{exc} = 480\text{ nm}$).

The absorption spectrum of the thermodynamically stable *t*A-GNP shows in CHCl_3 the typical band at 360 nm of the chromophore *t*A and a contribution of the gold core which becomes dominant in the region above 550 nm (Fig. 62). Moreover the absorption spectrum of *t*A-GNP can be obtained as a linear combination of the spectrum of *t*A and of a reference sample of $\text{CH}_3(\text{CH}_2)_{11}\text{SH}$ stabilized GNP in the same solvent (Fig. 62). This indicates that both the electronic interactions between the *t*A units bound to the surface and their interaction with the gold core are weak and that selective excitation of the *t*A ligand at 360 nm is possible. Hence we investigated the effect of the binding to the GNP on the photo-isomerization $t \rightarrow c$ process by irradiating the *t*A-GNP at 360 nm in the same conditions used for the reference compound *t*A.

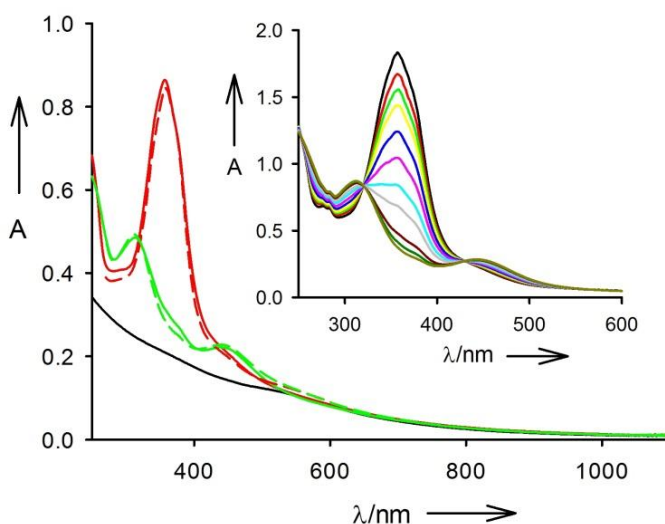


Fig. 62: Continuous lines: absorption spectrum of the thermodynamically stable *t*A-GNP in CHCl_3 (red) of the photo-isomerized NPs *c*A-GNP (green) and of reference $\text{CH}_3(\text{CH}_2)_{11}\text{SH}$ stabilized GNP (black) Dashed lines: linear combinations of the absorption spectrum of the reference GNP with those of the ligand *t*A. (red) and *c*A (green).

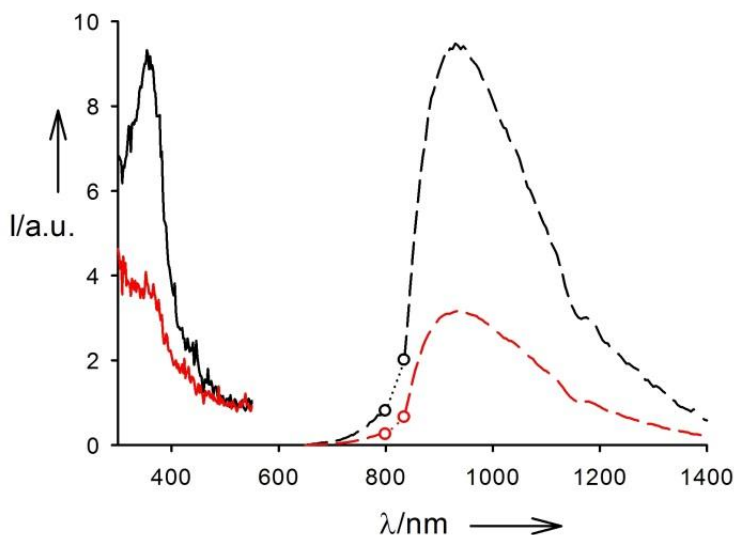


Fig. 63: Continuous lines: excitation spectrum of the thermodynamically stable *tA*-GNP in CHCl_3 (black) of the photo-isomerized NPs *cA*-GNP (red). Dashed lines: luminescence spectra ($\lambda_{\text{exc}}=360$ nm) of the thermodynamically stable *tA*-GNP in CHCl_3 (black) of the photo-isomerized NPs *cA*-GNP (red).

The absorption spectra recorded after increasing irradiations time intervals are shown in the inset of Fig. 62 where it is possible to observe that when the photo-stationary state is reached, the spectrum shows the peaks at 314 nm and 448 nm of the *cis* form of the ligand *cA* and that the same two isosbestic points at 319 nm and 430 nm observed during the photo-isomerization of the free ligand *tA* are maintained.

Moreover the absorption spectrum recorded at the photostationary state matches perfectly with the one expected in the case of the same degree of $t \rightarrow c$ conversion (>95%) observed for the ligand alone. The ligands at the photo-stationary state are hence almost completely in the *cis* form and the corresponding NPs will be indicated as *cA*-GNP. The photoisomerization quantum yield measured for *tA*-GNP was $\Phi_{t-c} = 0.23$. As far as luminescence is concerned a broad emission band in the NIR region is observed with maximum at about 930 nm upon excitation of

either *t*A-GNP or *c*A-GNP in CHCl₃. Moreover the emission spectral profile is independent on the excitation wavelength in the 300-600 nm range for both samples. In order to investigate the effect of the ligand photoisomerization on the NIR luminescence we compared the emission spectra of the same sample of NPs recorded first in the thermodynamically stable and then after irradiation in the photo-stationary state at different excitation wavelengths. The emission spectra recorded upon direct excitation of gold core at $\lambda_{\text{exc},2}=550$ nm, where neither *t*A or *c*A absorbs light are, within the experimental, error identical. Upon excitation at 360 nm, on the other hand a decrease of about 60% of the emission band is observed going from *t*A-GNP to *c*A-GNP as an effect of the *t* → *c* photoisomerization (Fig. 63). These observations allowed us to conclude that while the emission quantum yield of the Gold NP does not change because of the photo-isomerization, part of the excitation energy adsorbed by *t*A is transferred to the gold leading to sensitized emission. The occurrence of such a quite effective sensitization is confirmed by the excitation spectrum of the NIR emission shown in Fig. 63 where the band corresponding to the absorption of *t*A is clearly detectable in the *t*A-GNP. On the contrary the typical absorption band at 450 nm of the *cis* form *c*A is not detectable in the excitation spectrum of the photoisomerized NPs *c*A-GNP (Fig. 63) indicating that excitation energy transfer from *c*A to GNP is poorly efficient.

In order to detect the luminescence changes in real time during the photoisomerization process, we developed an experimental setup suitable for detecting simultaneously the light transmitted and emitted by the NPs samples during irradiation (Fig. 64). In Fig. 64 the changes of the absorbance and luminescence of *t*A-GNP during irradiation are plotted and compared with the changes of the absorbance of *t*A in the same conditions. The good overlap between the absorbance and luminescence plots for *t*A-GNP confirms the correlation between the photoisomerization process and the decrease of the luminescence intensity of the GNP. In particular both these plots could be fitted with an exponential decay with a decay constant of $k= 0.43 \pm 0.03 \text{ min}^{-1}$. Absorbance changes measured for the reference compound *t*A show the same kinetics as *t*A-GNP (Fig. 64)

with an almost identical decay constant $k = 0.42 \pm 0.03 \text{ min}^{-1}$. These results confirm that the rate of the $t \rightarrow c$ photo-isomerization process for tA bound to the GNP surface is identical to one measured for the free molecule in solution. Upon irradiation at 480 nm of cA -GNP $c \rightarrow t$ photo-isomerization occurs and when the photo-stationary state is reached about 70% of the NP bound cA is converted into tA .

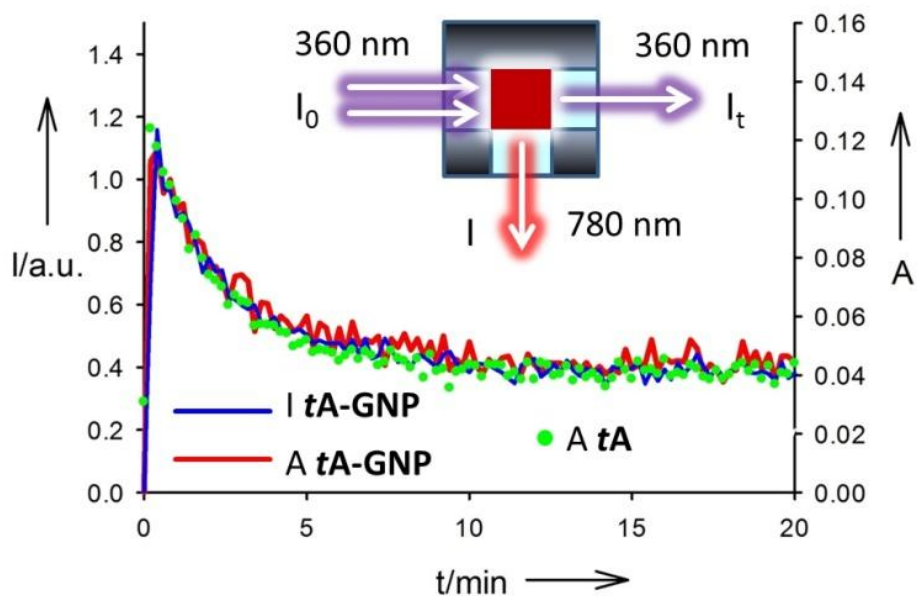


Fig. 64: Changes in the photophysical properties of tA -GNP during irradiation at 360 nm in $CHCl_3$. The setup used for the measurements is schematized in the inset. The fraction of irradiation light (I_0) transmitted by the sample I_t is used to measure the absorbance in real time ($A = -\log I_0/I_t$, red line). Luminescence at 780 nm is also measured in real time (I , blue line). The absorbance changes of a $CHCl_3$ solution of tA during irradiation at 360 nm were also measured (green dots).

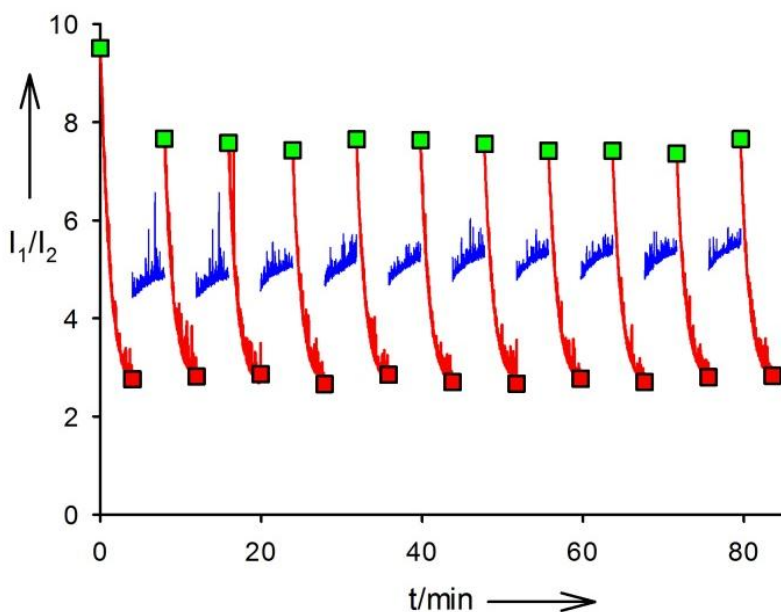


Fig. 65: NIR luminescence intensity ratio upon excitation at $\lambda_{exc,1}$ ($\lambda_{exc,1} = 360$ nm for the red tracks and $\lambda_{exc,1} = 450$ nm for the blue tracks, intensity I_1 is measured at 780 nm) and $\lambda_{exc,2}=550$ (intensity I_2 at 780 nm) of tA-GNP in $CHCl_3$. Squares show the emission intensity at the beginning (green) and at the end (red) of each irradiation at 360 nm ($t \rightarrow c$ photo-isomerization).

In order to demonstrate the possibility of using dual excitation to detect by luminescence the isomerization we perform a series of cycles by detecting the GNPs emission intensity upon excitation at $\lambda_{exc,1}=360$ nm and $\lambda_{exc,2}=550$ nm as I_1 and I_2 respectively. The ratiometric signal I_1/I_2 as a function of irradiation time is shown in figure 4 where each red tack show a $t \rightarrow c$ photo-isomerization cycles. Regeneration of the *trans* form was achieved by irradiation at 450 nm. As shown in Fig. 64, the NIR emission decreases upon irradiation (and hence excitation) at 360 nm. In particular starting from tA-GNP an intensity decrease of about 70% is observed in the first 240 s of irradiation because of the isomerization of tA and the consequent loss of the sensitized emission.

During the following 240 s irradiation (and excitation) at 450 nm the NIR emission intensity slightly increases and when irradiation (and excitation) wavelength is switched again to 360 nm a strong increase of the emission intensity with respect to the final value of the previous UV irradiation cycle is observed.

The NIR emission upon excitation at 360 nm in the ON states, which correspond to a high fraction of *tA* isomers on the GNP surface is shown in Fig. 64 as green square while the intensity in the OFF states (high fraction of *cA* isomers) is shown by the red squares.

4.4 Conclusions

In conclusion the NIR emission of the GNP can be switched ON/OFF by alternating UV/Vis irradiation thanks to the occurrence of an efficient ET process from *tA* to the GNP that generate a sensitized contribution which constitute most part of the total emission.

In conclusion we demonstrated that photo-isomerization of the azobenzene derivative *tA* bound to GNP occurs efficiently. Conversion of a high fraction (>95%) of *tA* into *cA* occurs in *tA*-GNP with a quantum yield almost identical to the one measured for *tA* in solution (upon irradiation at 360 nm). Regeneration of 70% of the *trans* form was achieved by irradiation at 450 nm. Photoluminescence measurements showed that *tA*-GNP emit in the NIR region upon direct excitation of the gold core ($\lambda_{\text{exc},2}=550$ nm) and that upon excitation of the *tA* ligand ($\lambda_{\text{exc},1}=360$ nm) an energy transfer process from the molecular ligand to the metal core occurs leading to sensitized NIR emission. Thanks to this process the ratio of the intensity of emission measured in the two different excitation conditions ($\lambda_{\text{exc},1}$ and $\lambda_{\text{exc},2}$) can be used to detect the isomerization state of the NPs. This unprecedented result is very promising in view of the development of new photo-responsive nanomaterials for theranostic.

5 Silica nanoparticles gathering luminescent glutathione protected Gold nanoclusters

5.1 Introduction

Luminescent GNCs have raised great interest in the last decades because of their potential applications in many fields as sensing, optoelectronic, energy storing, imaging and catalysis.⁷ They have been demonstrated to possess superior photochemical stability⁷⁷ compared to common organic fluorophores,¹⁵⁴ good emission QYs, long luminescence lifetimes,⁷⁷ interesting chiral and non-linear optical properties, large cross-section, tunable emissions (Fig. 6) and luminescence sensitivity to the environment.^{71,79} Due to the good biocompatibility of gold, and according to the recent literature, they are promising to combine low toxicity and interesting optical and electronic properties.

Also if their luminescence mechanism is not completely understood their suitability for *in vivo* and *in vitro* applications has been demonstrated in several precedent works. As already explained GNCs are smaller than kidneys glomerular filtration cut off and have been demonstrated to be cleared very rapidly from mice organisms through the renal pathway. For example, 2nm GSH coated luminescent GNCs have been shown to be cleared, from mice bodies, for more than the 50%, after the first 24h post injection.^{132,133} This is generally a highly desirable feature for nanoprobes designed for nanomedicine applications, however longer in-organism residence times would be desirable for long term applications.

GNCs stability in solution have been shown to be stable in the order of weeks and, among the others, Au₂₅SG₁₈ GNC have been shown to be one of the most resistant.^{155,38} Its encapsulation in larger solid matrices should however result in an improved resistance against external chemicals and quenching agents thus leading to a better a better stability and applicability.

The aim of this work is to include luminescent Au₂₅SG₁₈ clusters inside ≈20 nm PEGylated silica nanoparticles to develop a novel biocompatible contrast agent for live biomedical luminescence imaging. Grouping many LGNCs inside silica nanostructures may result in a probe with enhanced performance for several reasons. These kinds of SiO₂ NPs have been proven to be a not toxic easily functionalizable platform which can be excreted from the body as well but through hepatobiliary pathway.¹⁵⁶ As the renal filtration is the fastest excretion pathway, the larger size of included clusters prolong their residence time inside organisms and enhance the EPR effect in tumor targeting¹. These Silica particles are composed by a core of silica and a shell of PEG which contribute to prolong their *in-vivo* circulatory half-life¹. The grouping of many clusters units in larger structures is expected to result in a better contrast in both targeted luminescence and X-ray based imaging techniques, because of the presence of multiple detectable species per targeting unit.

For the encapsulation we have chosen a classical synthesis protocol for the production of biocompatible SiO₂ NPs whose *in-vivo* compatibility has already been proven.¹⁵⁶ The chemistry of these particles is well known and they can be easily further functionalized both on their surface^{156b,157} and in their core^{156, 158,159} using conventional protocols. For example, the surface can be functionalized with targeting or anchoring functions while inside the core, other molecules as drugs, phluorophores or contrast agents can be encapsulated.

In this work it has been developed a ligand exchange protocol for synthesizing luminescent Au₂₅(SG)₁₈ clusters and a protocol to include them inside silica nanostructures. It will be shown that this new composite material possesses interesting different physicochemical characteristic compared to its precursors, which confer them some advantages.

Moreover in-silica encapsulation has the unexpected effect of enhancing significantly the clusters luminescence QY. In order to test the applicability of the final probe for NIR luminescence imaging applications, Gold encapsulated clusters have been tested directly on mouse fibroblasts cells.

5.2 Materials

L-Cysteine $\geq 97\%$, Glutathione $\geq 87\%$, $\text{HAuCl}_4 \cdot 3\text{H}_2\text{O}$ ACS grade, NaOH pellets reagent grade $\geq 98\%$, Tris(2,2'-bipyridyl)dichlororuthenium(II) hexahydrate powder, Tetraethyl orthosilicate (TEOS) reagent grade 98%, Pluronic F127 and $\text{NaBH}_4 \geq 96\%$ purum p.a., were purchased from Sigma Aldrich. Cells were NIH/3T3 (ATCC® CRL-1658™) and cell culture medium was Dulbecco's Modified Eagle's Medium (DMEM) was (Gibco-Life Technologies Corporation).

5.3 Methods

The starting $\text{Au}_{25}\text{Cys}_{18}$ has been synthesized according to the protocol developed by Yuan, while the exchange and inclusion protocols are illustrated in the results and discussion section.²⁷ HRTEM images were acquired on a FEI Tecnai F20T TEM microscope at 200 kW on quantifoil grids. Emissions have been recorded using a NIR specific monochromator copuled with both a fastPMT and a nitrogen cooled Ge detector respectively for the visible and the IR regions. The response of the instrument have been calibrated for both detectors using a dedicated reference lamp. The NIR emission spectra obtained in this work are the combination of two spectra registered with the two different detectors and corrected considering their wavelength dependent responses. Fluorescence QYs have been calculated using Tris(2,2'-

bipyridyl)dichlororuthenium(II) hexahydrate as reference (QY = 2.8 %). For imaging experiments on mouse fibroblasts, 0,4 mL of a solution of nanoparticles $\text{Au}_{25}\text{SG}_{18}@\text{SiO}_2$ with absorbance at 480 nm $A(480) = 0,1$ have been sterilized by filtration (200 nm cut-off) and added to a cell culture in adhesion and in presence 1,6 mL of culture medium. Cells have been incubated for 24 hours and have been imaged on petri dishes in PBS after three washing cycle with 1 mL of PBS 1X. Images have been acquired using an Olympus IX 71 inverted microscope equipped with a Xenon lamp (450 W) for fluorescence excitation and a cooled EMCCD photonmax 512 CCD camera from Princeton instruments. Samples have been irradiated exciting at 480 nm and a cut-off filter at 700 nm has been used to exclude autofluorescence contributions to the emission.

NIH/3T3 (ATCC® CRL-1658™) Cells were cultured in Dulbecco's Modified Eagle's Medium (DMEM) (Gibco-Life Technologies Corporation) supplemented with 10% fetal bovine serum (FBS) Nord-America, 2mM L-glutamine and 50U/mL penicillin/streptomycin. Cells were kept in incubator at 37°C, 5% CO₂, 21% O₂ and were passed upon trypsin digestion every three or four days using a splitting ratio of 1:4 avoiding cells to reach full confluence.

5.4 Results and discussion

We used the protocol developed by Yuan²⁷ to synthesize $\text{Au}_{25}(\text{Cys})_{18}$ and then we exchange its ligand with glutathione to obtain a luminescent Au_{25} cluster. After the three hours reaction described in the Yuan protocol, 50 mL solution of $\text{Au}_{25}(\text{Cys})_{18}$ have been processed as follow. With no additional purification steps, the volume of the solution have been doubled by adding a GSH solution (30,7 mg/5ml) in NaOH 0,2M (the concentration of GSH in solution was 10 times higher than that of cysteine). In such conditions, the large excess of glutathione leded to the occurrence of two simultaneous reactions, the ligand exchange and the etching of the clusters. Due to the etching process, which occurs faster at

basic pH, the characteristic absorption spectra of Au₂₅ slowly disappeared until, after 177 minutes, no traces of Au₂₅ were detectable with UV/Vis spectroscopy. During the etching, clusters absorption spectrum remains unaltered, except for its overall intensity Fig. 66. This was due to the particular stability against etching of glutathione protected Au₂₅ GNCs reported also by the Tsukuda group.¹⁵⁵

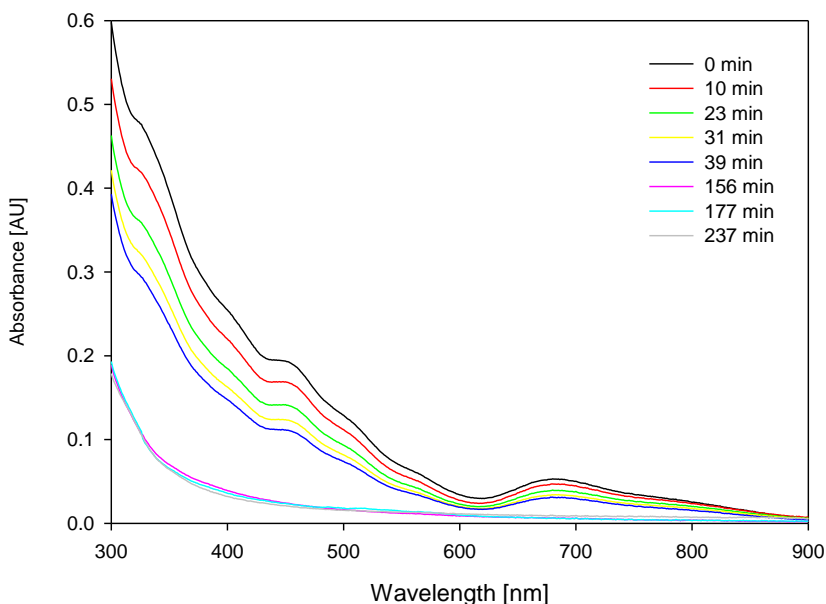


Fig. 66: Absorption spectra of Au₂₅(Cys)₁₈ at different times during ligand exchange and etching by an excess of glutathione at pH ≈ 12.

This higher stability results in the faster and complete etching of whichever other cluster originated from the Au₂₅ starting one.

In order to slow down the etching, after about 45s from the addition of the excess of GSH, the pH of the solution has been switched to 6,4 adding glacial HOAc (300microl on 2,5 mL of cluster solution). This solution was rapidly injected and induced hydrogen production due to the acid reaction with the NaBH₄ excess still present in solution.

Due to the presence of bubbles it was not possible to follow the absorption spectra of the system immediately after acidification. When the development of hydrogen ceased, after about 10 minutes, the volume of the solution have been triplicate adding methanol in order to precipitate the clusters.

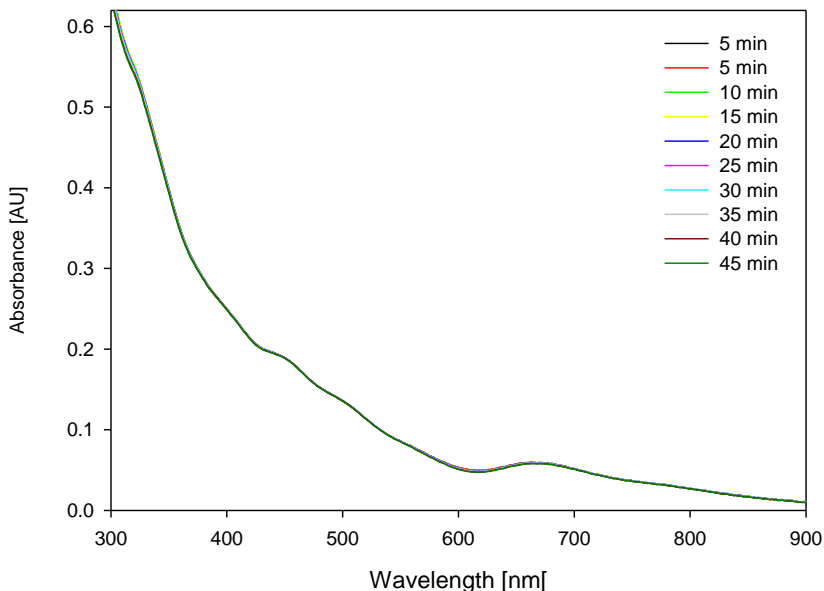


Fig. 67: Absorption spectra of $Au_{25}(Cys)_{18}$ at different times during ligand exchange and etching by an excess of glutathione at neutral pH.

The absorption feature of the solution before filtration were unchanged, accounting for the fact that the ratio between GSH/Cys molecules bonded to the cluster surface, immediately before the acidification, was sufficient for its stabilization in acid environments (while $Au_{25}(Cys)_{18}$ would have irreversibly precipitated in the same conditions).

The solution has been centrifuged at 2500 rpm and, after complete removal of the supernatant, they have been redispersed in pure methanol and centrifuged again at 2000 rpm. After the complete removal the

supernatant, clusters have been redissolved in 50 mL of a GSH solution in neutral deionized (MilliQ) water (30,5mg/5ml), and the volume have been then triplicate by adding neutral MilliQ water. In the same large excess of GSH, but at neutral pH, the etching process still happen, but proceed very slowly compared to the basic condition (Fig. 67). In both cases, the absorbance at 675nm decrease linearly in time (Fig. 68).

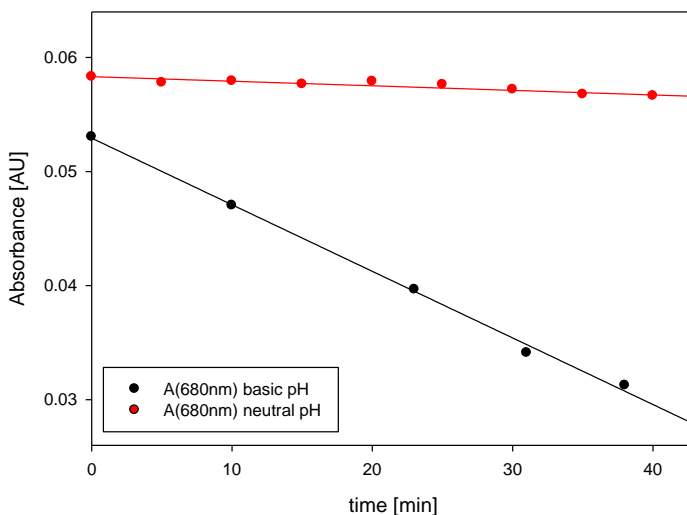


Fig. 68: Absorbance variation at 680 nm of $Au_{25}(Cys)_{18}$ during ligand exchange and etching by an excess of glutathione at pH ≈ 12 (black) and at neutral pH.

The solution has been left stirring for three hours to allow the conclusion of the ligand exchange.¹⁶⁰ $Au_{25}(Cys)_{18}$ is not emissive (Fig. 69) while $Au_{25}(Cys)_{18}$ has been shown to emit at 750 nm with QYs in the order of 10^{-3} . NIR emission intensity has been shown to be directly proportional to the number of polar ligands inserted on cluster surface during the exchange,⁸² thus it is possible to follow the exchange with spectrofluorimetry (Fig. 70). As the exchange preceded the luminescence intensity increased until it reached a plateau at the end of the exchange.

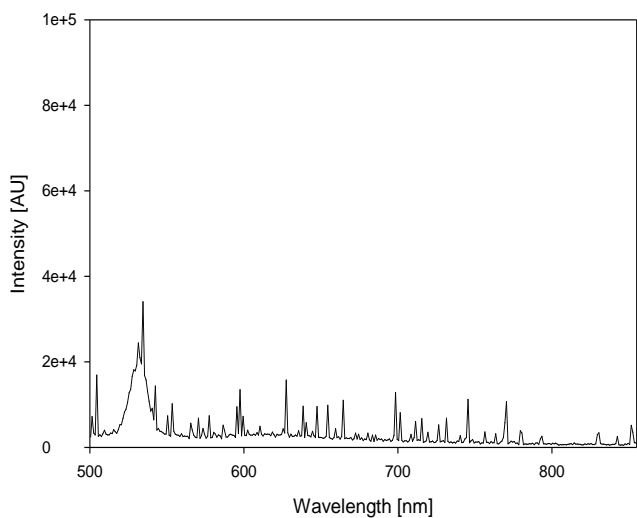


Fig. 69: luminescence spectrum of the non emissive $Au_{25}(Cys)_{18}$.

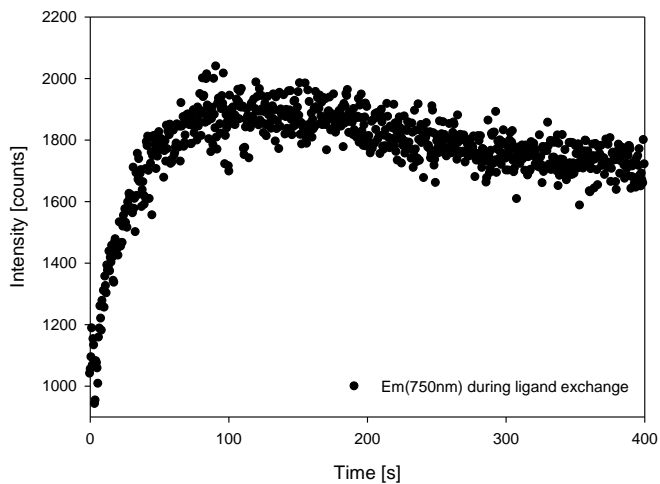


Fig. 70: Au_{25} luminescence intensity at 750 nm, upon excitation at 450 nm during the ligand exchange of between cysteine and glutathione at neutral pH.

In order to be sure, also if the exchange seemed complete after 300 s we decided to wait three hours as suggested by previous accurate NMR studies on thiols exchanges at neutral pH.¹⁶⁰ At the end of the exchange, the solution absorption spectrum remained unchanged, confirming the integrity of the clusters core, while the luminescence QY switched from $<10^{-5}$ to $1.2 \cdot 10^{-3}$ in accordance with the previous reported values for $\text{Au}_{25}(\text{SG})_{18}$.^{38,161,85} Also the emission wavelength and shape, (Fig. 71) together with the decay lifetimes coincided with the previous reports on $\text{Au}_{25}(\text{SG})_{18}$ (246 and 1200 ns⁸⁵) being well fitted by two components: $t_1 = 244 \pm 10$ ns (22.3%) and $t_2 = 1421 \pm 21$ ns (77.7%).

All of these observations indicate a complete ligand exchange.

After three hours the product has been precipitated by addition of methanol and filtered on a 450nm PTFE syringe filter. The filtrate has been repeatedly and rapidly washed with methanol and redissolved in HOAc 1M to obtain a solution with $A_{(675\text{nm})} = 0,4281$. 1,565 mL of this solution have been mixed with 1,565 mL of HOAc 1M containing 200mg of Pluronic F127. The mixture has been stirred in a 4mL vial at a speed comprised between 600 and 750 rpm at room temperature. After 15 minutes of stirring 175 microliters of TEOS have been rapidly injected in the solution maintaining the same stirring speed. The day after, the solution have been purified through dialysis against 3*6 L of distilled water before further characterizations. Dialysis was performed at room temperature under gentle stirring with regenerated cellulose dialysis tubing (Sigma, mol wt cut-off $>12\ 000$ Da, average diameter 33 mm).

An IR extended characterization of the photophysical properties of Au_{25} and silica included glutathione capped GNCs ($\text{GS-GNCs}@SiO_2\text{NPs}$) has been performed. After the inclusion reaction, the absorption spectrum of the cluster lost its characteristic absorption peaks but presented three very weak bands which didn't seem to be related to the previously existing ones. The NIR emission of the Au_{25} cluster is composed by two absorption bands, one centered at 710 nm and the other at 800 nm, in good accordance with the values measured by Wu et al.⁸⁵ and other previous reports (considering the correction for the detector response).

After the inclusion inside silica NPs, these two emissions are slightly shifted to 708 nm and 813 nm and the ratio between their intensities changes slightly. Although the emission shape remain substantially the same, interestingly GNCs emission QY, increased from 1.2×10^{-3} to 9.2×10^{-3} after the inclusion.

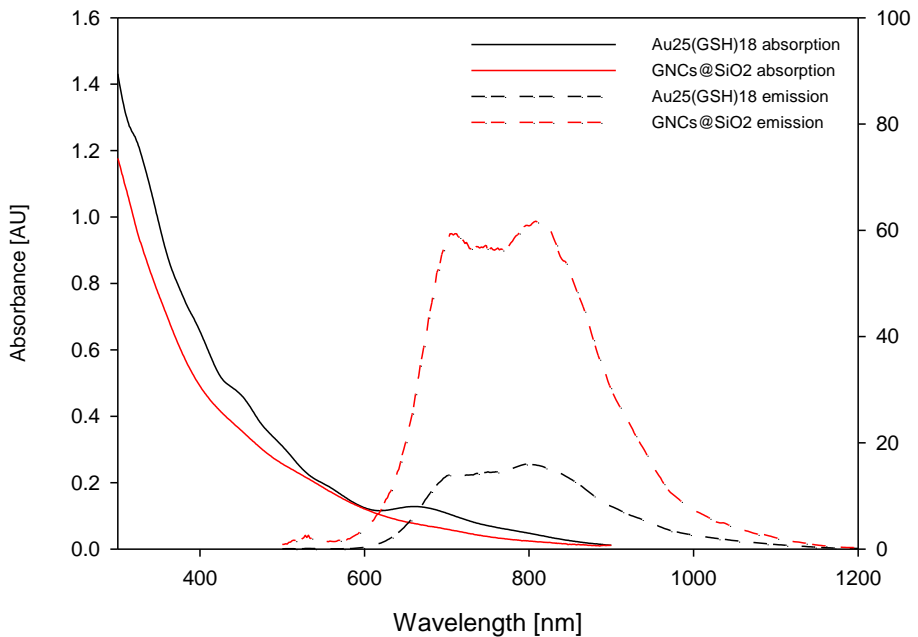


Fig. 71: Absorption (solid lines) and emission (dashed lines) spectra of $Au_{25}(SG)_{18}$ (black) and GS-GNCs@SiO₂NPs (red).

The lifetime of the emission at 750 nm, measured exciting at 405 nm, is a multiesponential and again it can be well fitted by two lifetimes $t_1 = 247 \pm 10$ ns (21.5%) and $t_2 = 1460 \pm 22$ ns (78.5%). These two measured lifetimes are in discrete accordance with the two ones measured by us and Wu et al for $Au_{25}(SG)_{18}$. (246 and 1200 ns).⁸⁵

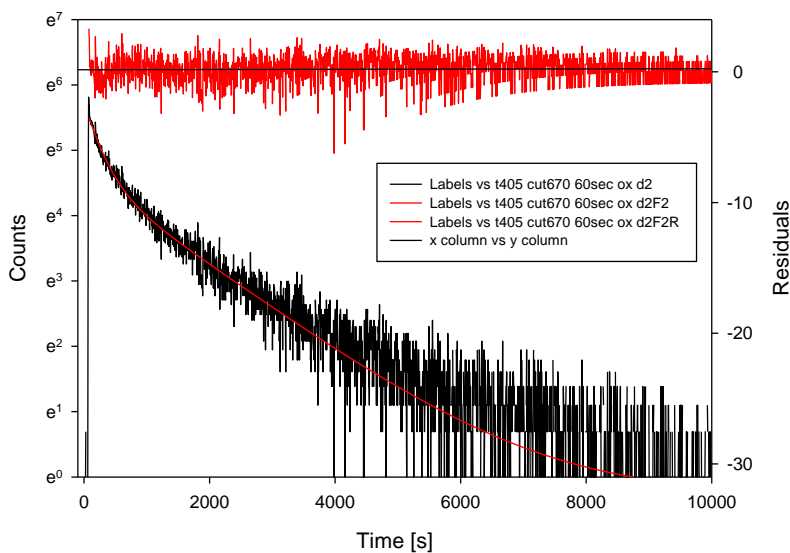


Fig. 72: Luminescence lifetime decay of GS-GNCs@SiO₂NPs (black) and fitting residuals (red). $\lambda_{irr} = 405$ nm.

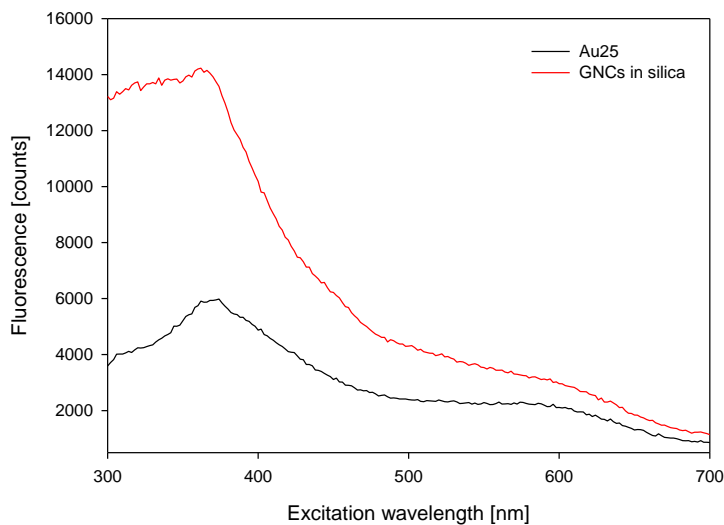


Fig. 73: excitation spectra of Au₂₅(SG)₁₈ (black) and GS-GNCs@SiO₂NPs (red).

After the inclusion also the excitation spectra shape remain unaltered, except for a slightly higher emission intensity for UV excitations wavelengths in the silica included clusters. In literature there are some discrepancies in the reported excitation spectra of $\text{Au}_{25}(\text{SG})_{18}$,^{38,161} however the one we acquired is almost identical to the one observed by the Tsukuda group after PAGE fractionation.³⁸ This observation indicate an high purity of the product. It has been investigated if the grouping of different clusters in larger particles leads to changes in their emission anisotropy but we found zero anisotropy for included clusters as for freely dissoveld ones (Fig. 74).

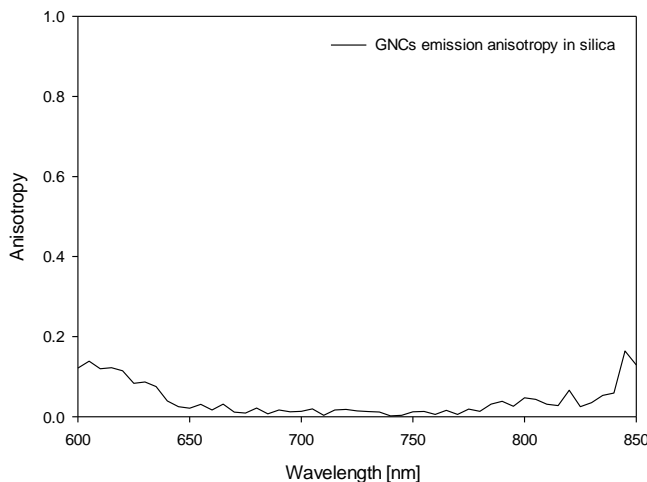


Fig. 74: GS-GNCs@SiO₂NPs emission anisotropy exciting at 450 nm.

$\text{Au}_{25}(\text{SG})_{18}$, GS-GNCs@SiO₂NPs, and SiO₂ NPs in absence of GNCs have been analyzed by HRTEM and STEM-HAADF and results are shown respectively from Fig. 75 to Fig. 77, from Fig. 78 to Fig. 80 and from Fig. 82 to Fig. 84. DLS characterization of GS-GNCs@SiO₂NPs and SiO₂ NPs in absence of GNCs is shown respectively in Fig. 85 and Fig. 86, while Fig. 81 shows the EDS analysis performed on GS-GNCs@SiO₂NPs.

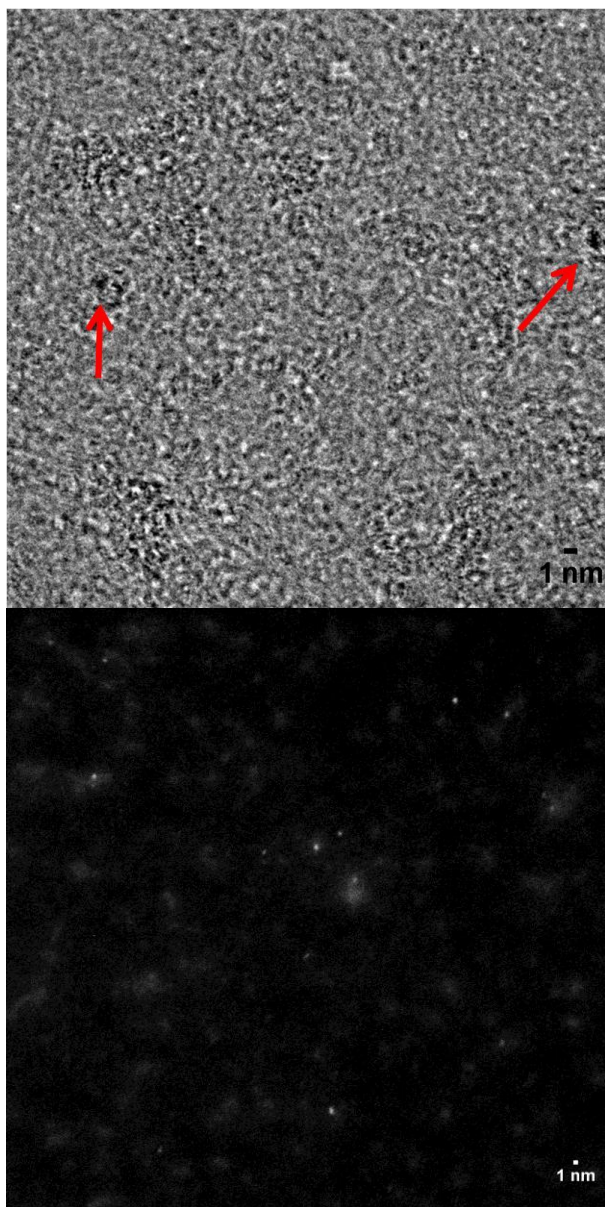


Fig. 75: HRTEM image of $Au_{25}(SG)_{18}$ (top) and STEM-HAADF micrographs of the same sample.

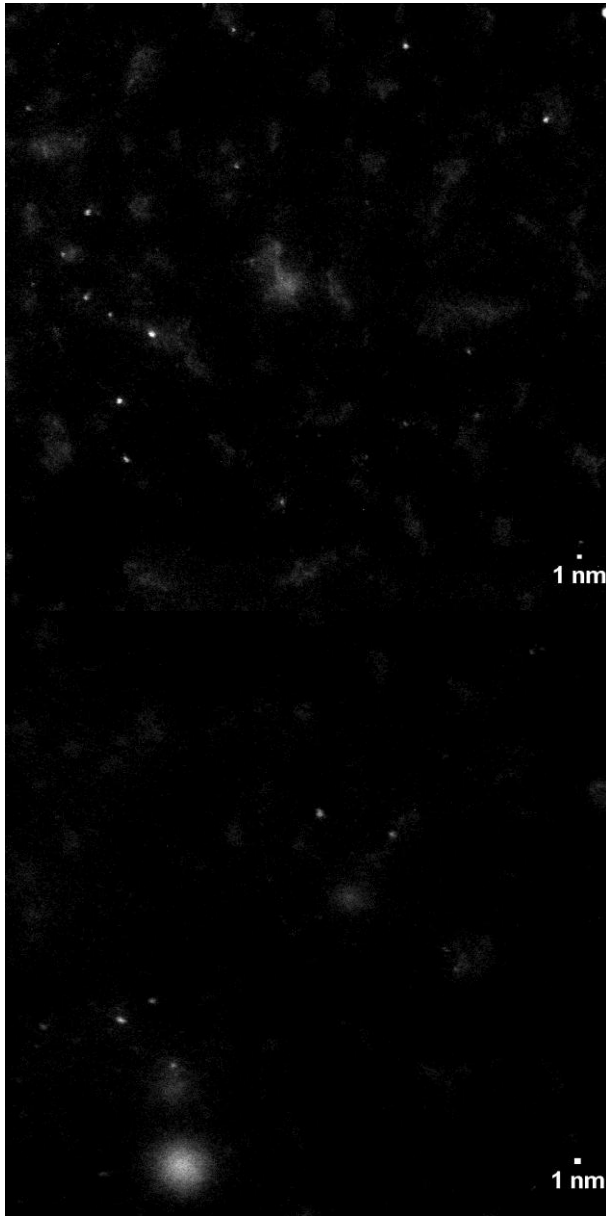


Fig. 76: STEM-HAADF micrographs of Au₂₅(SG)₁₈.

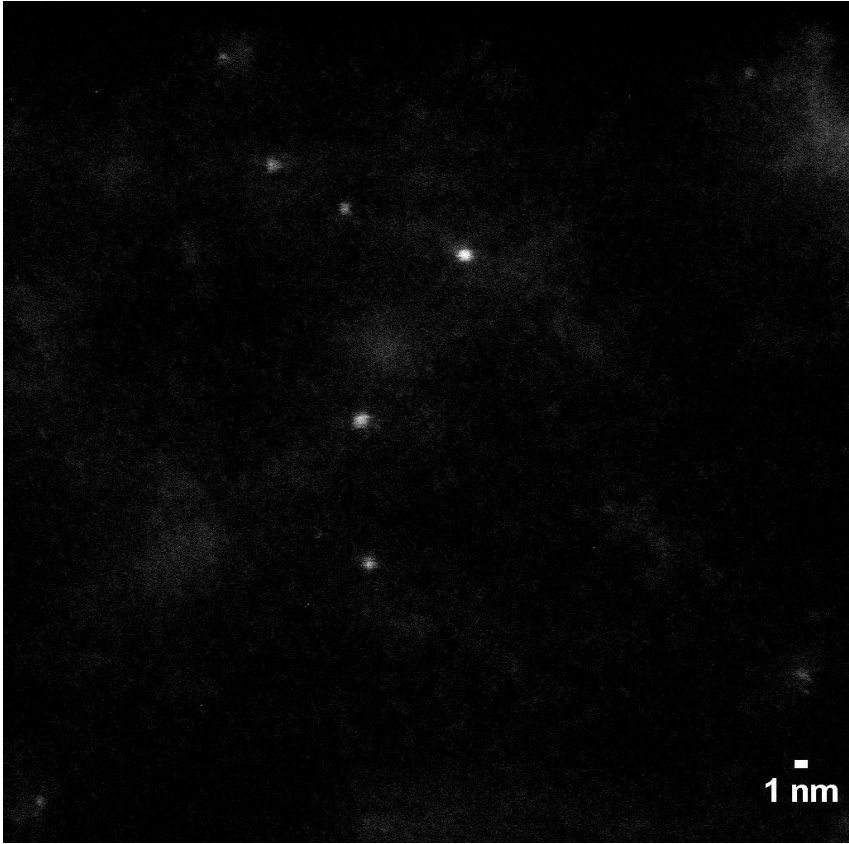


Fig. 77: STEM-HAADF micrographs of $Au_{25}(SG)_{18}$.

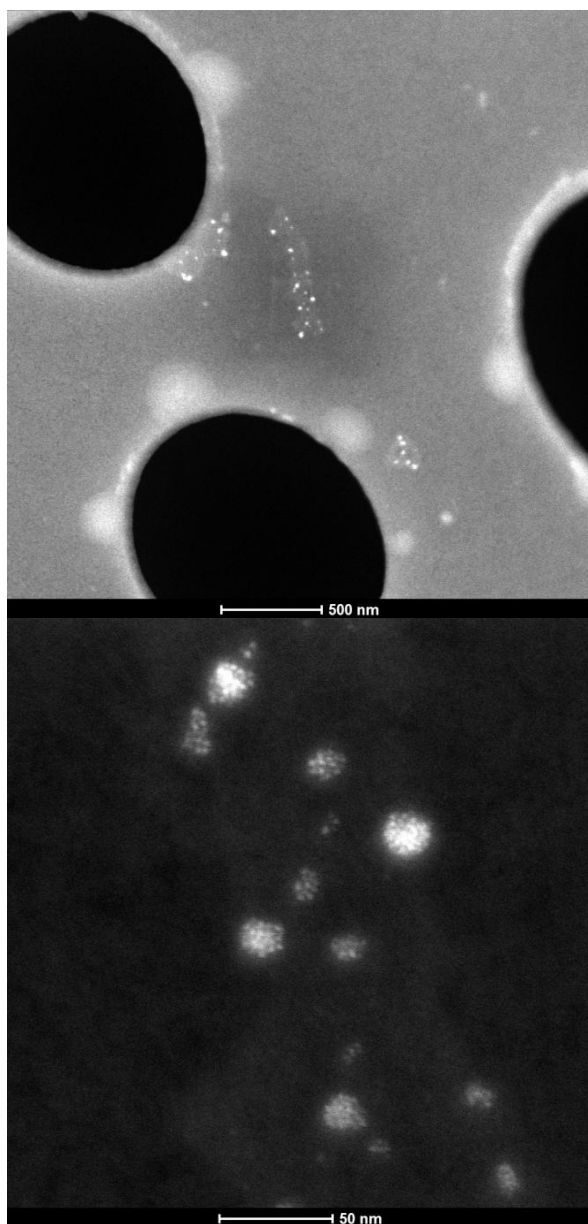


Fig. 78: STEM-HAADF micrographs of GS-GNCs@SiO₂NPs.

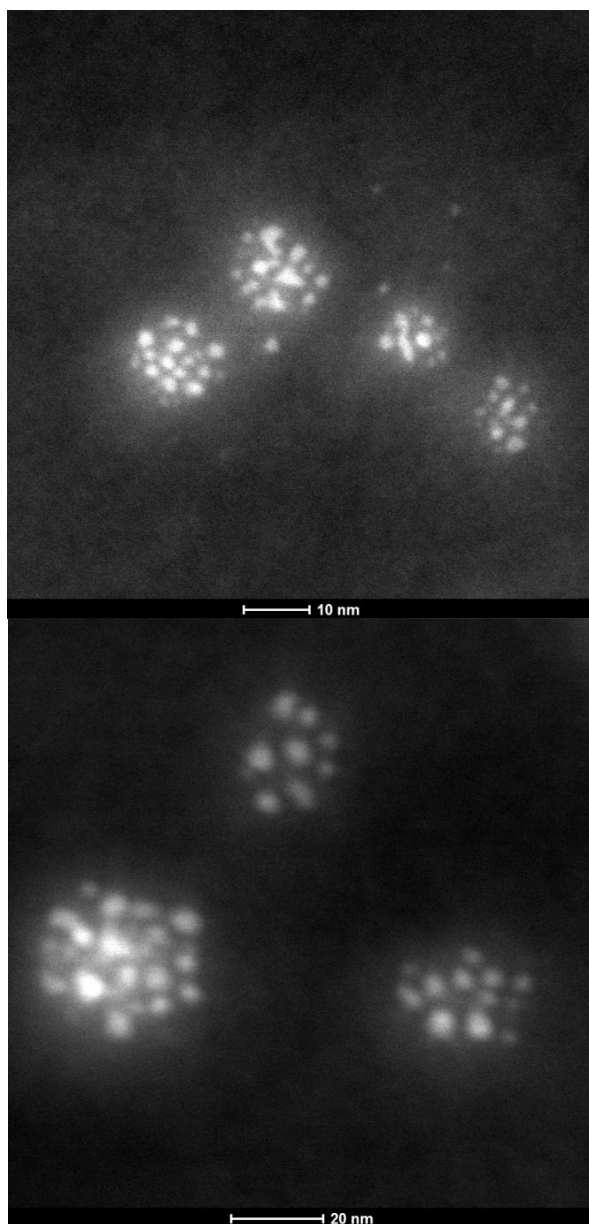
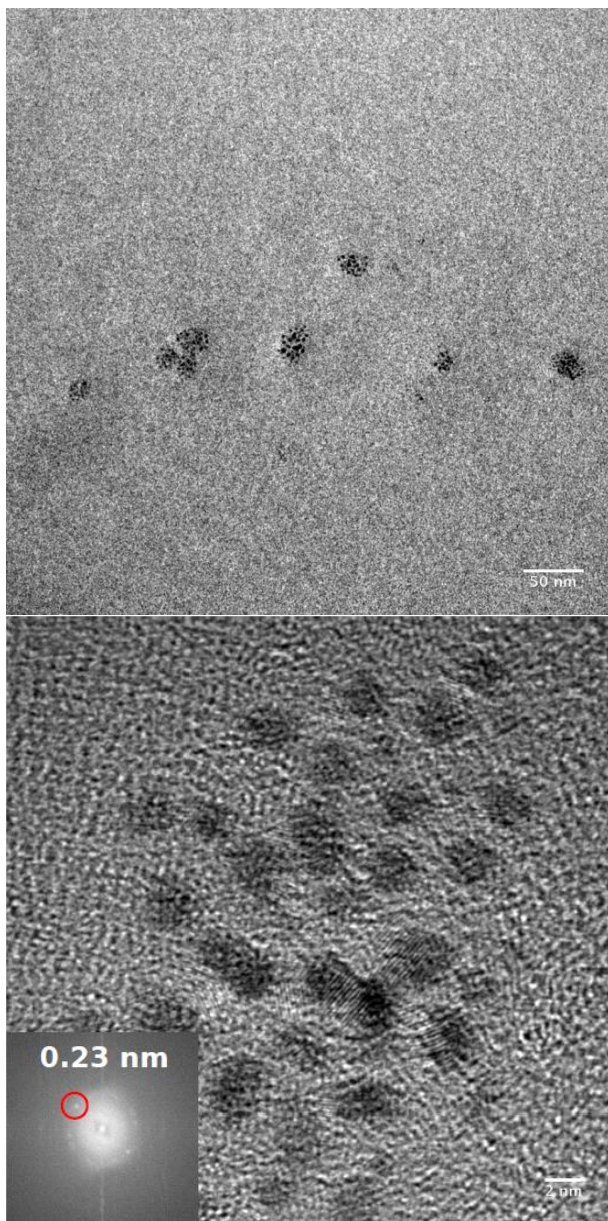


Fig. 79: STEM-HAADF micrographs of GS-GNCs@SiO₂NPs.



*Fig. 80: HRTEM images of GS-GNCs@SiO₂NPs (top), higher magnification image of included GNCs (bottom).
Gold crystalline lattice spacing = 0.23 nm (inset).*

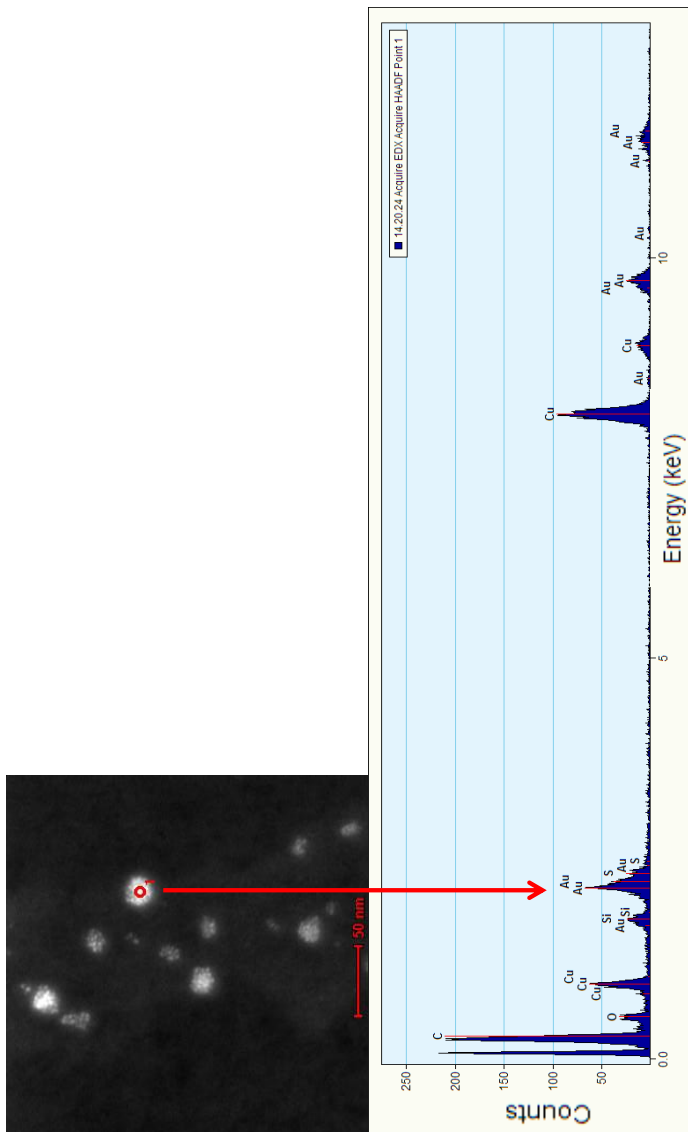


Fig. 81: EDS analysis performed on GS-GNCs@SiO₂NPs in correspondence of the packed bright spots.

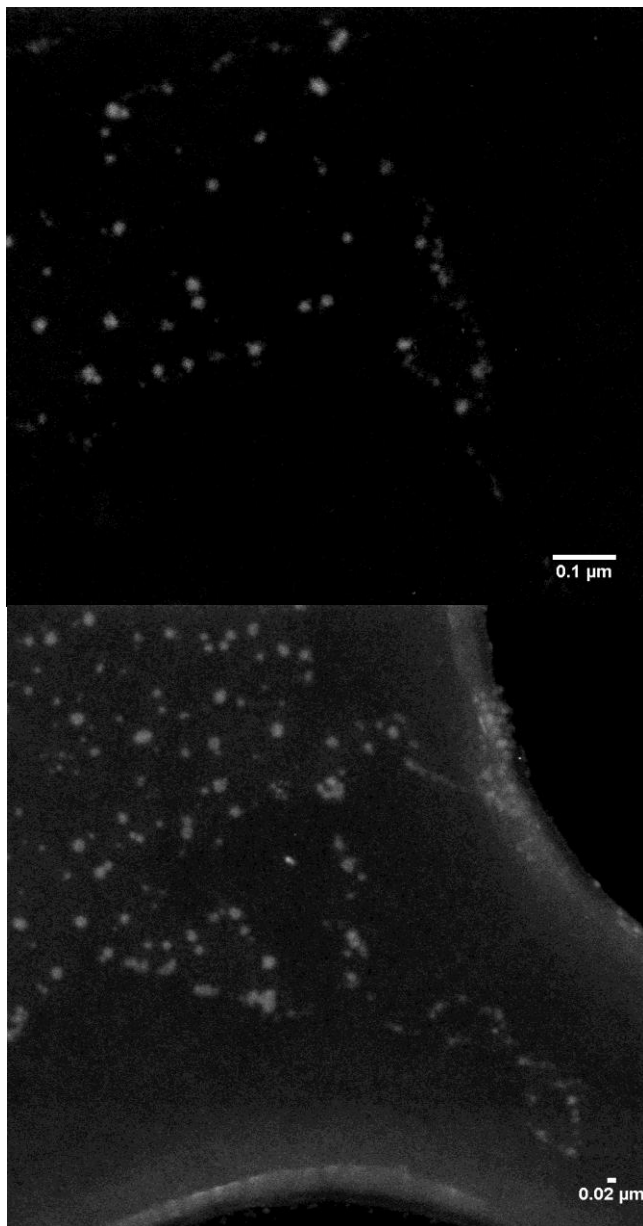


Fig. 82: STEM-HAADF micrographs of SiO₂NPs in absence of GNC.

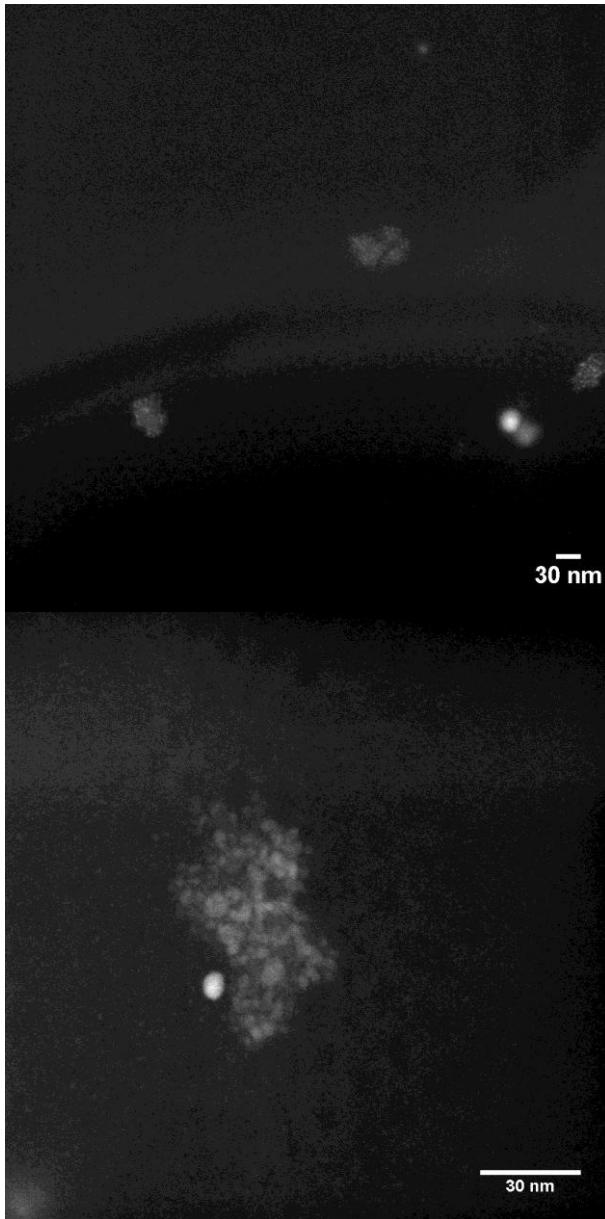


Fig. 83: STEM-HAADF micrographs of SiO₂NPs in absence of GNCs.

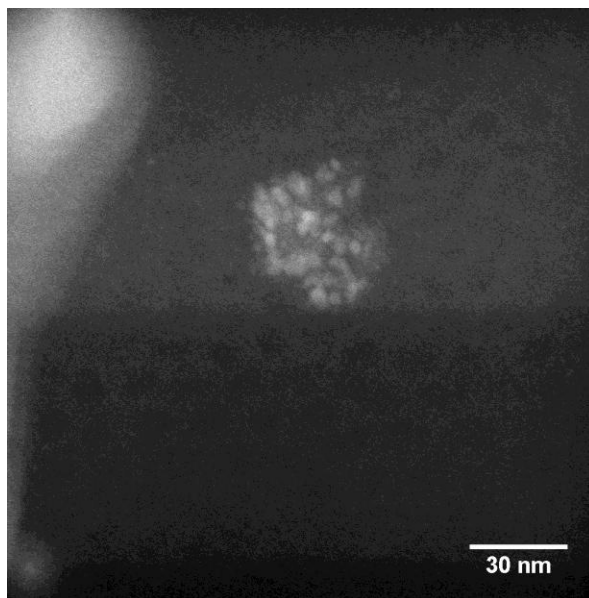


Fig. 84: STEM-HAADF micrographs of SiO₂NPs in absence of GNCs.

DLS measurements showed a mean diameter (md) of 16.3 nm with a PDI of 0.2 for GNCs loaded SiO₂ NPs, while they showed md= 17,2 nm and PDI= 0.16 for SiO₂ NPs control samples.

TEM characterization of Au₂₅SG₁₈ GNCs alone is in good accordance with the previous reports (mean diameter of 1 ± 0.2 nm)^{162 163} and clearly, they appear on the grid as randomly distributed. After the inclusion reaction, GNCs appear in TEM images only as tightly packed in almost spherical structures with diameters between 7 and 30 nm, which have size distribution and morphologies similar to the reference sample with SiO₂ NPs in absence of GNCs. EDX analysis confirmed the packed structures to be composed of gold and also detected the presence of sulphur due to the presence of GSH.

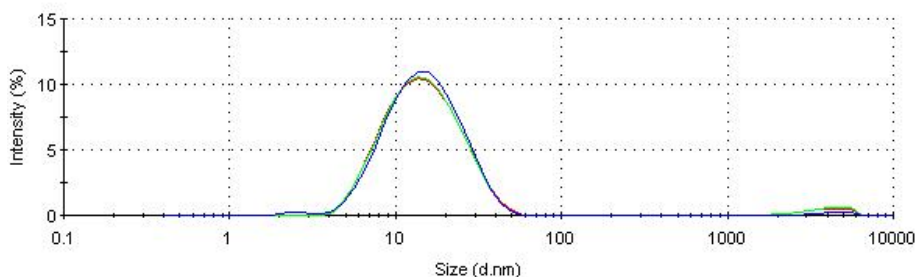


Fig. 85: DLS measured hydrodynamic radius of GS-GNCs@SiO₂NPs. Mean diameter: 16.3 nm, PDI: 0.2 and width: 8 nm.

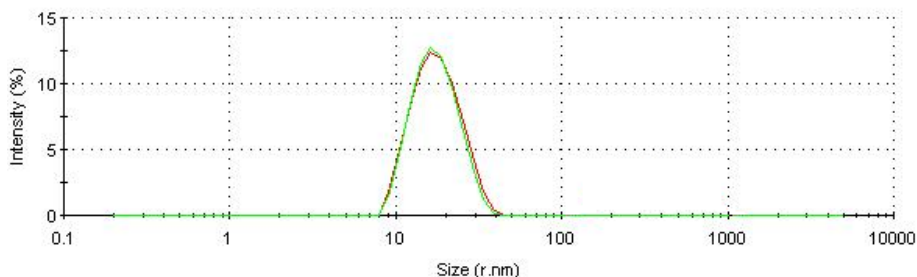


Fig. 86: DLS measure of the hydrodynamic radius of SiO₂NPs in absence of GNCs. Mean diameter: 17,2 nm PDI: 0.16 width: 5.4 nm.

The apparent included GNCs mean diameter observable in HRTEM images and STEM-HAADF micrographs was 2 nm. Almost no GNCs have been found outside the packed structures and there was no trace of empty SiO₂ NPs. Most of the GNCs were also retained by the dialysis tube during silica NPs purification while a very small portion of freely dissolved GNCs, escaped from the membrane. All of these observations allowed us to conclude that all GNCs that remain in the purified final product are encapsulated inside the silica nanostructures.

The absence of a strong DLS signal in correspondence of hundreds of nanometers account the fact that the slightly brighter spots surrounding groups of silica NPs are due to drying phenomena, and not to the presence of large silica flakes which would also result in a turbid solution. We think that to understand if the included clusters are still Au₂₅ is an almost impossible challenge for the following reasons. Some evidences suggested that the included GNCs may still have been Gold 25. The excitation and the emission spectra, as the emission lifetime decay profile, were almost identical before and after the inclusion reaction. However the absorption spectra lost its characteristic discrete transitions after the in-silica inclusion, suggesting the generation of different gold cluster species. Maybe, such a loss of the absorption spectral features could also be attributed to the different chemical environment surrounding the clusters or to their obligated dense packing which may determine electronic interactions and bands broadening. Other evidences account for the fact that included clusters are different species from the Au₂₅ starting one. TEM images apparently show clusters with sizes larger than the Au₂₅ one but this could also result from the prospective superposition of different Au₂₅ clusters. However, while Au₂₅ have been determined to have an icosahedric structure, some of the bigger clusters show interference bands which indicate a crystalline lattice spacing of 0,23 nm, which coincide with bulky gold crystalline structure. In any case the 200kV electron beam has enough energy to quickly melt both GNCs and SiO₂ NPs, so that the formation of bigger particles is likely to be generated by the electron beam during the measure. It has also to be considered that emissions composed by two bands, similar to that observed in the present work, have been proven to be generated also by GNCs which are not strictly Au₂₅¹⁶⁴. In the case of the included clusters, because of the loss of the typical absorption fingerprint of their precursor, it is not possible to understand if they still retain the Au₂₅ structure.

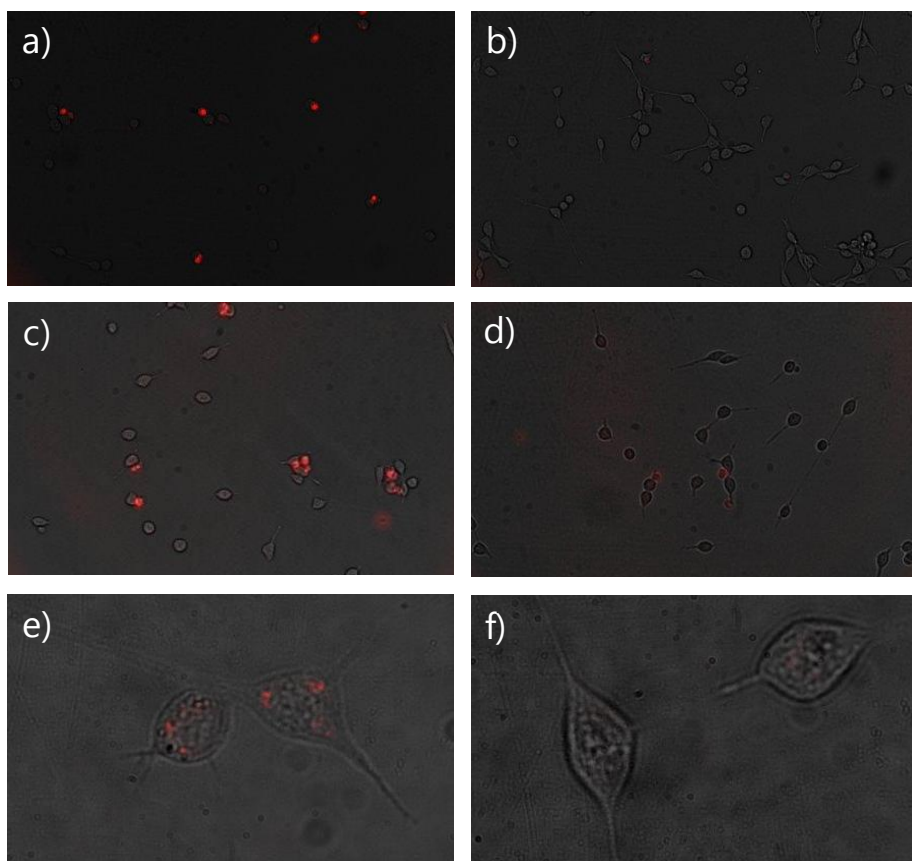


Fig. 87: All images are superimpositions of a transmission image (in black and white) and a luminescence image (in red). Images a), c) and e) show NIR luminescence cell images of mouse fibroblast cells (NIH/3T3) incubated for 24 in presence of GS-GNCs@SiO₂NPs, while b), d) and f) show NIR luminescence imaging of control samples. a), b), c) and d) have been acquired using 10 X magnification while e) and f) using 60 X. Luminescence images have been acquired exciting at 480 nm, with a cut-off filter at 700 nm and observing at $\lambda > 700$ nm.

24h incubation of the final product in a mouse fibroblast culture resulted in a selective uptake of the probe from some cells. We didn't investigated the biological reasons and meaning of this selective uptake, however it was clear that the uptaken particles possessed optical properties that allowed the visualization of live cells by luminescence imaging. In accordance with previous report on similar silica NPs,^{156a} higher magnification of GS-GNCs@SiO₂NPs uptaking cells revealed that these nanoparticles are mainly localized inside endosomes distributed in the cytoplasm. Images have been acquired with a cut-off filter at 700 nm to exclude autofluorescence and emission has thus been acquired at $\lambda > 700$ nm in the therapeutic windows.

5.5 Conclusions

In this work we developed a fast method to prepare highly luminescent Au₂₅SG₁₈ GNCs, via ligand exchange, from the non emissive Au₂₅Cys₁₈. We developed a protocol for the inclusion of Au₂₅SG₁₈ GNCs inside reasonably well monodispersed PEGylated silica nanoparticles. This inclusion protocol generate in-silica trapped GNCs with the same emission properties of their Au₂₅SG₁₈ precursor but with a:

- ≈ 8 folds enhanced emission QY compared to Au₂₅SG₁₈ QY measured in this study and in ref.³⁸
- ≈ 5 folds enhanced emission QY compared to Au₂₅SG₁₈ QY measured in ref.¹⁶¹ and ⁸⁵.

We found that in-silica inclusion enhance Au₂₅SG₁₈ emission quantum yield which is already one of the most emitting GNCs. Cluster encapsulation in solid matrix should also protect them from the external environment, conferring them major stability and reducing luminescence quenching due to the interaction with external agents. The kind of silica nanoparticles we used for the inclusion have been shown to be highly biocompatible *in-vivo* and to be

cleared from mice organisms through epathobiliary pathway.^{156b,158} Despite small GNCs have been shown to be rapidly cleared from mice through renal pathway, the higher hydrodynamic radius of included clusters, superior to the kidneys glomerular filtration cut-of, confer them longer persistence inside the organism, overcoming the limitations of the first specie, in the case of longer term applications. Larger sizes also improve their EPR (enhanced permeability and retention) effect, conferring them a better applicability as markers for tumoral tissues.¹ At the same time, the PEG layer surrounding these NPs prolong their circulatory half-life expanding the time range to perform their functions.¹ The gathering of many luminescent GNCs inside silica NPs enhance their brightness in addition to their QY, allowing to achieve a better contrast in NIR fluorescence imaging applications.

Despite GNCs have lower luminescence QYs compared to other organic fluorophores, they are characterized by a superior photostability which, in some cases, is even superior to that of Cd/Se quantum dots.⁷⁷ Their three order of magnitude longer emission lifetime, compared to common fluorophores, makes GNCs better candidates also for gated imaging.⁷⁷

We demonstrated that our sub-50 nm GS-GNCs@SiO₂NPs with emission QY close to one percent can be successfully applied in live cell luminescence imaging. Moreover, compared to free GNCs, the nanoprobe we developed possesses different physicochemical features which may probably be exploited for cells luminescence imaging or X-ray based *in-vivo* whole body imaging.

We hope our fast exchange and encapsulation protocol will open new ways and possibilities for GNCs practical applications.

6 Conclusions

In this work it has been given an overview of the most recent advances in the synthesis, characterization and bio-medical application of luminescent Gold nanospecies. The combination of photoactuators and nanostructures has been proven to result in an apparent reduction of dyes PI QYs, due to the nanomaterials absorbance contribution, also in absence of actual interactions between the two components. It has been proposed a simple approach to take into consideration this contribution and to perform quantitative measurements of dyes PI efficiencies variations in presence of nanoparticles. The PI QY reduction has been found to be qualitatively proportional to the magnitude of the interaction between the dye and the particles measured by NMR. Strong interaction between particles monolayer ad absorbed AB derivatives have been proven to result in significant decreases of the dye PI QY. It has been shown that photoisomerization effectively determines a change in the repartition of the AB derivative between particle monolayer and solution, confirming that photoisomerization reaction can probably be exploited for light triggered drug release. These results provided valuable tools and methodologies which improved the state of the art in the quantitative study of light triggered processes in nanoparticles based systems.

For the first time it has been proven that GNPs luminescence can be switched on and off thanks to the photoisomerization of an azobenzene derivative covalently bound on the Gold surface. This has been proven to happen thanks to an efficient energy transfer between the *trans* AB derivative and the GNPs which leads to a sensitized NIR emission whose intensity can be tuned by photoisomerization. These unprecedented results are promising for the development of Gold based light responsive nanoparticles for theranostics.

Finally, starting from $\text{Au}_{25}(\text{Cys})_{18}$, it has been successfully developed a complex probe for luminescence based imaging composed by NIR

emitting GNCs encapsulated inside mesoporous PEGylated silica NPs. This probe has been demonstrated to present some improved luminescence features compared to its precursors and it has been shown to possess good optical properties for cells luminescence imaging applications.

7 Experimental section

7.1 Synthesis of 8-(4-((4-methoxyphenyl)diazenyl)phenoxy)octyl-thiol

Azobenzyl-thiol derivative (5) has been prepared by the research group of Professor F. Mancin according to Scheme 4.

7.1.1 Synthesis of 4-((4-methoxyphenyl)diazenyl)phenol

(2): 830 mg (6.7 mmol) of *p*-anisidine are dissolved in 15 mL of milliQ water, the solution is cooled to 0° C in an ice bath and 2 mL of concentrated HCl are added dropwise. Subsequently, 465 mg of NaNO₂ (6.7 mmol) are added and the reaction is stirred for 1 h. After this time, 470 mg of phenol (5.0 mmol) dissolved in 10 mL of a 2.5 M NaOH solution in water are added. The mixture is stirred for 10 minutes, and then the white precipitate is filtered, obtaining 590 mg (yield 39 %) of product.

¹H- NMR (250 MHz, CDCl₃) δ: 7.89 (dd, 4H, ArH), 6.98 (dd, 4H, ArH), 3.89 (s, 3H, CH₃O).

7.1.2 Synthesis 1-(4-((8-bromooctyl)oxy)phenyl)-2-(4-methoxyphenyl)diazene

(3): 7.0 g of 1,8-dibromooctane (25.7 mmol) and 3.5 g of K_2CO_3 (25.7 mmol) are dissolved in 150 mL of a THF:DMF 3:1 mixture, 590 mg of **2** (2.6 mmol) are then added and the mixture is left under stirring at room temperature overnight. The solvent is then removed by evaporation at reduced pressure and the reaction crude is redissolved in CH_2Cl_2 . The organic phase is then washed with water (3 × 100 mL), dried over Na_2SO_4 and the solvent is removed by evaporation at reduced pressure. The crude product is purified by flash chromatography (silica gel CH_2Cl_2/n -hexane, 1:1, $R_f = 0.8$), obtaining 550 mg (60 % yield) of product.

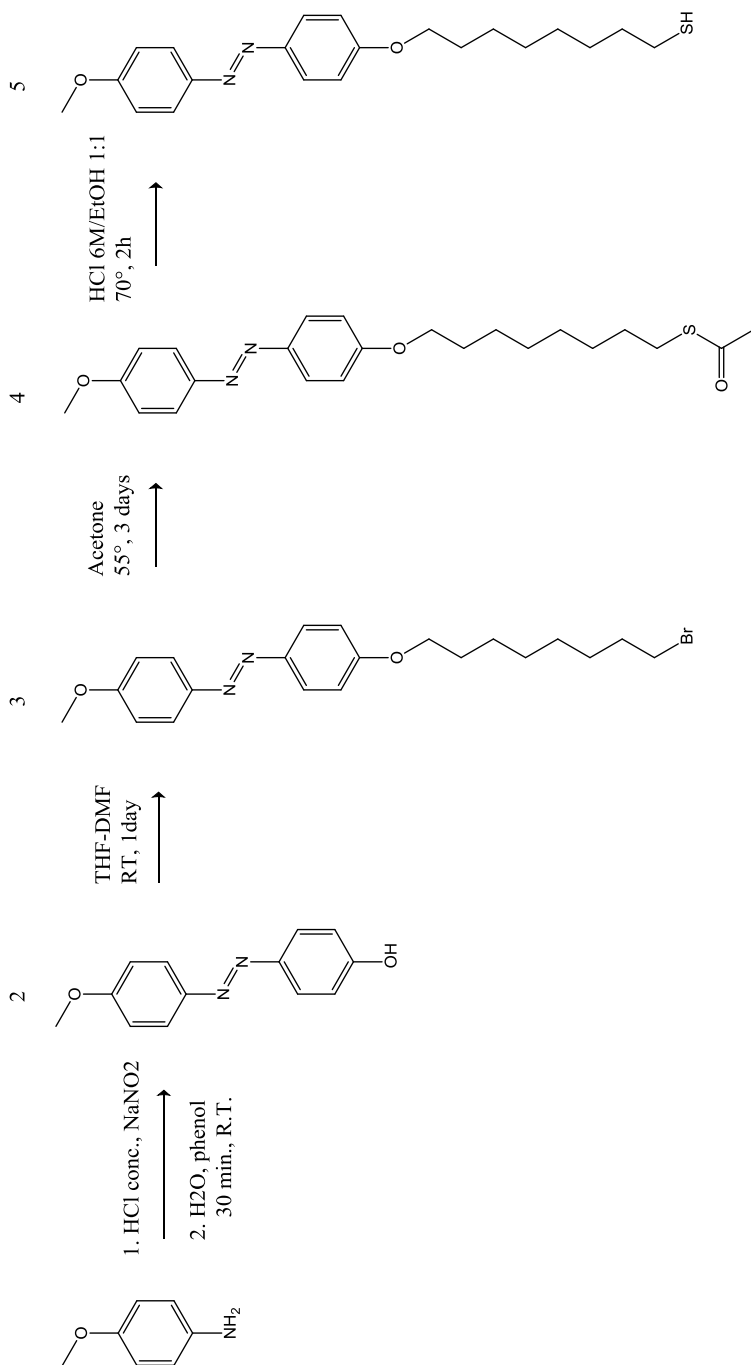
1H - NMR (250 MHz , $CDCl_3$) δ : 7.87 (dd , 4H , ArH) , 6.99 (m, 4H, ArH), 4.03 (t, 2H, CH_2O) , 3.89 (s, 3H , CH_3O), 3.41 (t, 2H, CH_2Br), 1.59 (m, 6H, CH_2).

7.1.3 Synthesis of 8-(4-((4-methoxyphenyl)diazenyl)phenoxy)octylthiol

(5): 550 mg of **3** (1.3 mmol) and 200 mg of potassium thioacetate (1.7 mmol) are dissolved in 50 mL of acetone. The reaction mixture is stirred at reflux under N_2 atmosphere for 48 hours. The solvent is then removed by evaporation at reduced pressure and the residue is purified by flash chromatography (silica gel, CH_2Cl_2/n -hexane 1:1, $R_f = 0.5$) obtaining 438 mg (73 % of yield) of product.

1H -NMR (250 MHz , $CDCl_3$) δ : 7.87 (m, 4H, ArH) , 6.98 (m, 4H, ArH), 4.01 (t , 2H, CH_2O), 3.87 (s, 3H , CH_3O), 2.86 (t , 2H, CH_2S), 2.32 (s, 3H , $CH_2C=O$), 1.54 (m, 6H, CH_2).

Deprotection in acid environment (EtOH:HCl 6M, 1:1) at 70 °C for 2 hours leads to deprotected azobenzyl derivative **5**.



Scheme 4: Synthesis of 8-(4-((4-methoxyphenyl)diazenyl)phenoxy)octyl-thiol (5).

7.2 Synthesis of azobenzene derivative functionalized GNPs (*tA-GNPs*)

Monolayer protected gold nanoparticles (AuNPs) were prepared according to a previously reported two-step procedure,¹⁶⁵ All the glassware used in the AuNPs preparation was washed with aqua regia and rinsed with distilled water. H₂AuCl₄ is strongly hygroscopic and was weighted within a dry-box.

A solution of H₂AuCl₄·3H₂O (100 mg, 0.254 mmol) in water (4 mL) was extracted with a solution of tetraoctylammonium bromide (5 g, 9.14 mmol) in N₂ purged toluene (250 mL). To the resulting reddish-orange organic solution, dioctylamine (3.36 g, 13.92 mmol) is added (the amount of dioctylamine was calculated in order to obtain 2 nm nanoparticles). The mixture is vigorously stirred under N₂ for 30 min. During this period of time the color of the mixture fades. A solution of NaBH₄ (93.0 mg, 2.46 mmol) in H₂O (1 mL) is then rapidly added. The color of the solution turns rapidly to black due to nanoparticles formation. After 2 hours of stirring, the aqueous layer is removed. To the above nanoparticle solution, the thiol (0.254 mmol) dissolved in 3 mL of isopropanol is rapidly added. The reaction mixture is evaporated and the resulting crude is dissolved in CH₂Cl₂ and purified by gel permeation chromatography with Biorad Bio-Beads S-X1 resin.

7.3 Instrumentations and techniques

UV/Vis absorption spectra have been acquired with a double beam spectrophotometer UV/Vis Perkin Elmer Lambda-45. Luminescence spectra and anisotropy measure were performed with an Edinburgh Analytical Instruments FLS920, equipped with a time-correlated single-photon counting device for luminescence lifetimes measurements, a nitrogen cooled EO-817S Germanium Detector system with a Ge PIN diode detector for IR emission spectra acquisitions and Glan-Thompson polarizers for anisotropy determinations.

Dynamic Light Scattering (DLS) measurements have been performed using a Malvern Instruments DLS ZetaSizer Nano-ZS.

^1H NMR spectra were recorded using a Bruker AV III 500 spectrometer operating at 500 MHz.

In the case of azobenzyl-thiol derivative functionalized GNPs, NMR spectra were recorded using a Bruker AV300 spectrometer operating at 300 MHz for ^1H .

Thermogravimetric analysis (TGA) was run on 1-2 mg nanoparticle samples using a Q5000 IR model TA instrument from 30 to 1000 °C under a continuous air flow.

HRTEM images and STEM-HAADF micrographs were recorded on a FEI Tecnai F20T TEM equipped with a Schottky field emitter a Gatan MSC794 CCD camera, Fischione High Annular Dark Field STEM detector and Double tilt specimen holder. Elemental analysis measures were performed with an EDAX EDS X-ray spectrometer PV9761 with Super Ultra thin window. Measures were performed at 200kV on quantifoil grids.

In the case of the nanoparticles synthesized by the F. Mancin group, TEM images were recorded on a Jeol 300 PX electron microscope.

Luminescence microscopy has been performed using an Olympus IX 71 inverted microscope equipped with a Xenon lamp (450 W) for luminescence excitation, equipped with a cut-off filter at 700 nm and a Electron Multiplying Charge Coupled Device EMCCD Camera (Princeton Instruments, Photon Max 512) sensible in the visible and the IR ranges. Excitation have been performed at 480 nm while observation was at $\lambda > 700$ nm until the limit of the camera detector. Cells images are the superimposition of luminescence and transmission images; emission is in red while transmission images are in black and white.

Acknowledgements

We are grateful for the ERC-Starting Grant MOSAIC financial support.

My Thanks to Beatrice Rivalta for the encouragement, Eugenio Bottura for the practical support, my family for the patience and Sara Bonacchi, Damiano Genovese, Massimo Sgarzi, Enrico Rampazzo, Luca Ravotto, Luca petrizza, Raffello Mazzaro, Vittorio Morandi, Sara Springhetti, Arbel Artzy-Schnirman, Stefania Rapino, Matteo Calvaresi, Professors Marco Montalti, Fabrizio Mancin, Francesco Zerbetto, Molly Stevens, Sergio Bertazzo, Paolo Ferratini and Orazio Sturniolo for their fundamental teachings.

References

1. Dreaden, E. C.; Alkilany, A. M.; Huang, X.; Murphy, C. J.; El-Sayed, M. A., The golden age: gold nanoparticles for biomedicine. *Chemical Society Reviews* **2012**, *41* (7), 2740-2779.
2. *Bull Hist Chem.* **2009**, *34* (2), 105-16.
3. M., F., The Bakerian Lecture: Experimental Relations of Gold (and Other Metals) to Light. *Philosophical Transactions of the Royal Society of London* *147*, 145-181.
4. Suryanarayana, C.; Koch, C. C., Nanocrystalline materials – Current research and future directions. *Hyperfine Interactions* *130* (1), 5-44.
5. Toumey, C., The literature of promises. *Nat Nano* **2008**, *3* (4), 180-181.
6. Johnston, R., Atomic and Molecular Clusters.
7. (a) Ke, C.-Y.; Wu, Y.-T.; Tseng, W.-L., Fluorescein-5-isothiocyanate-conjugated protein-directed synthesis of gold nanoclusters for fluorescent ratiometric sensing of an enzyme-substrate system. *Biosensors & Bioelectronics* **2015**, *69*, 46-53; (b) Hakkinen, H., Atomic and electronic structure of gold clusters: understanding flakes, cages and superatoms from simple concepts. *Chemical Society Reviews* **2008**, *37* (9), 1847-1859; (c) Khlebtsov, N.; Dykman, L., Biodistribution and toxicity of engineered gold nanoparticles: a review of in vitro and in vivo studies. *Chemical Society Reviews* **2011**, *40* (3), 1647-1671; (d) Tao, Y.; Li, M.; Ren, J.; Qu, X., Metal nanoclusters: novel probes for diagnostic and therapeutic applications. *Chemical Society Reviews* **2015**.
8. Barrett, C. J.; Mamiya, J.-i.; Yager, K. G.; Ikeda, T., Photo-mechanical effects in azobenzene-containing soft materials. *Soft Matter* **2007**, *3* (10), 1249-1261.
9. Hartley, G. S.; Le Fevre, R. J. W., 119. The dipole moments of cis- and trans-azobenzenes and of some related compounds. *Journal of the Chemical Society (Resumed)* **1939**, (0), 531-535.

10. Bandara, H. M. D.; Burdette, S. C., Photoisomerization in different classes of azobenzene. *Chemical Society Reviews* **2012**, *41* (5), 1809-1825.
11. Beharry, A. A.; Woolley, G. A., Azobenzene photoswitches for biomolecules. *Chemical Society Reviews* **2011**, *40* (8), 4422-4437.
12. Abendroth, J. M.; Bushuyev, O. S.; Weiss, P. S.; Barrett, C. J., Controlling Motion at the Nanoscale: Rise of the Molecular Machines. *ACS Nano* **2015**, *9* (8), 7746-7768.
13. Browne, W. R.; Feringa, B. L., Making molecular machines work. *Nat Nano* **2006**, *1* (1), 25-35.
14. Chambers, J. J.; Kramer, R. H., Light-Activated Ion Channels for Remote Control of Neural Activity. *Methods in cell biology* **2008**, *90*, 217-232.
15. Yuan, Q.; Zhang, Y.; Chen, T.; Lu, D.; Zhao, Z.; Zhang, X.; Li, Z.; Yan, C.-H.; Tan, W., Photon-Manipulated Drug Release from a Mesoporous Nanocontainer Controlled by Azobenzene-Modified Nucleic Acid. *ACS Nano* **2012**, *6* (7), 6337-6344.
16. Varnavski, O.; Ramakrishna, G.; Kim, J.; Lee, D.; Goodson, T., Critical Size for the Observation of Quantum Confinement in Optically Excited Gold Clusters. *Journal of the American Chemical Society* **2010**, *132* (1), 16-17.
17. Philip, R.; Chantharasupawong, P.; Qian, H.; Jin, R.; Thomas, J., Evolution of Nonlinear Optical Properties: From Gold Atomic Clusters to Plasmonic Nanocrystals. *Nano Letters* **2012**, *12* (9), 4661-4667.
18. Natarajan, G.; Mathew, A.; Negishi, Y.; Whetten, R. L.; Pradeep, T., A Unified Framework for Understanding the Structure and Modifications of Atomically Precise Monolayer Protected Gold Clusters. *The Journal of Physical Chemistry C* **2015**, *119* (49), 27768-27785.
19. Markus, R.; Schwentner, N., Photoinduced Aggregation and Dissociation of Ag and Au Clusters in Rare Gas Matrices. In *Physics and Chemistry of Small Clusters*, Jena, P.; Rao, B. K.; Khanna, S. N., Eds. Springer US: 1987; pp 611-616.
20. Fedrigo, S.; Harbich, W.; Buttet, J., Optical response of Ag₂, Ag₃, Au₂, and Au₃ in argon matrices. *The Journal of Chemical Physics* **1993**, *99* (8), 5712-5717.

21. Yang, X.; Yang, M.; Pang, B.; Vara, M.; Xia, Y., Gold Nanomaterials at Work in Biomedicine. *Chemical Reviews* **2015**, *115* (19), 10410-10488.
22. Schooss, D.; Weis, P.; Hampe, O.; Kappes, M. M., Determining the size-dependent structure of ligand-free gold-cluster ions. *Philosophical Transactions of the Royal Society of London A: Mathematical, Physical and Engineering Sciences* **2010**, *368* (1915), 1211-1243.
23. Zhang, X.; Chibli, H.; Mielke, R.; Nadeau, J., Ultrasmall Gold-Doxorubicin Conjugates Rapidly Kill Apoptosis-Resistant Cancer Cells. *Bioconjugate Chemistry* **2011**, *22* (2), 235-243.
24. Poon, W.; Heinmiller, A.; Zhang, X.; Nadeau, J. L., Determination of biodistribution of ultrasmall, near-infrared emitting gold nanoparticles by photoacoustic and fluorescence imaging. *Journal of Biomedical Optics* **2015**, *20* (6).
25. Nair, L. V.; Nazeer, S. S.; Jayasree, R. S.; Ajayaghosh, A., Fluorescence Imaging Assisted Photo dynamic Therapy Using Photosensitizer-Linked Gold Quantum Clusters. *ACS Nano* **2015**, *9* (6), 5825-5832.
26. Zhu, M.; Lanni, E.; Garg, N.; Bier, M. E.; Jin, R., Kinetically controlled, high-yield synthesis of Au-25 clusters. *Journal of the American Chemical Society* **2008**, *130* (4), 1138-+.
27. Yuan, X.; Zhang, B.; Luo, Z.; Yao, Q.; Leong, D. T.; Yan, N.; Xie, J., Balancing the Rate of Cluster Growth and Etching for Gram- Scale Synthesis of Thiolate- Protected Au₂₅ Nanoclusters with Atomic Precision. *Angewandte Chemie-International Edition* **2014**, *53* (18), 4623-4627.
28. Alvarez, M. M.; Khoury, J. T.; Schaaff, T. G.; Shafigullin, M.; Vezmar, I.; Whetten, R. L., Critical sizes in the growth of Au clusters. *Chemical Physics Letters* **1997**, *266* (1-2), 91-98.
29. Negishi, Y.; Takasugi, Y.; Sato, S.; Yao, H.; Kimura, K.; Tsukuda, T., Kinetic Stabilization of Growing Gold Clusters by Passivation with Thiolates. *The Journal of Physical Chemistry B* **2006**, *110* (25), 12218-12221.
30. Xu, S.; Yang, H.; Zhao, K.; Li, J.; Mei, L.; Xie, Y.; Deng, A., Simple and rapid preparation of orange-yellow fluorescent gold nanoclusters using

DL-homocysteine as a reducing/stabilizing reagent and their application in cancer cell imaging. *Rsc Advances* **2015**, 5 (15), 11343-11348.

31. Sun, C.; Yang, H.; Yuan, Y.; Tian, X.; Wang, L.; Guo, Y.; Xu, L.; Lei, J.; Gao, N.; Anderson, G. J.; Liang, X.-J.; Chen, C.; Zhao, Y.; Nie, G., Controlling Assembly of Paired Gold Clusters within Apoferritin Nanoreactor for in Vivo Kidney Targeting and Biomedical Imaging. *Journal of the American Chemical Society* **2011**, 133 (22), 8617-8624.

32. Zhang, H.; Liu, Q.; Wang, T.; Yun, Z.; Li, G.; Liu, J.; Jiang, G., Facile preparation of glutathione-stabilized gold nanoclusters for selective determination of chromium (III) and chromium (VI) in environmental water samples. *Analytica Chimica Acta* **2013**, 770, 140-146.

33. Palmal, S.; Basiruddin, S. K.; Maity, A. R.; Ray, S. C.; Jana, N. R., Thiol-Directed Synthesis of Highly Fluorescent Gold Clusters and Their Conversion into Stable Imaging Nanoprobes. *Chemistry – A European Journal* **2013**, 19 (3), 943-949.

34. Aldeek, F.; Muhammed, M. A. H.; Palui, G.; Zhan, N.; Mattoussi, H., Growth of Highly Fluorescent Polyethylene Glycol- and Zwitterion-Functionalized Gold Nanoclusters. *ACS Nano* **2013**, 7 (3), 2509-2521.

35. Wu, Z.; Chen, J.; Jin, R., One-Pot Synthesis of Au-25(SG)(18) 2- and 4-nm Gold Nanoparticles and Comparison of Their Size-Dependent Properties. *Advanced Functional Materials* **2011**, 21 (1), 177-183.

36. Schaaff, T. G.; Knight, G.; Shafiqullin, M. N.; Borkman, R. F.; Whetten, R. L., Isolation and Selected Properties of a 10.4 kDa Gold:Glutathione Cluster Compound. *The Journal of Physical Chemistry B* **1998**, 102 (52), 10643-10646.

37. Negishi, Y.; Takasugi, Y.; Sato, S.; Yao, H.; Kimura, K.; Tsukuda, T., Magic-Numbered Aun Clusters Protected by Glutathione Monolayers (n = 18, 21, 25, 28, 32, 39): Isolation and Spectroscopic Characterization. *Journal of the American Chemical Society* **2004**, 126 (21), 6518-6519.

38. Negishi, Y.; Nobusada, K.; Tsukuda, T., Glutathione-protected gold clusters revisited: Bridging the gap between gold(I)-thiolate complexes and thiolate-protected gold nanocrystals. *Journal of the American Chemical Society* **2005**, 127 (14), 5261-5270.

39. Xie, J.; Zheng, Y.; Ying, J. Y., Protein-Directed Synthesis of Highly Fluorescent Gold Nanoclusters. *Journal of the American Chemical Society* **2009**, *131* (3), 888-+.
40. Zhang, W.; Ye, J.; Zhang, Y.; Li, Q.; Dong, X.; Jiang, H.; Wang, X., One-step facile synthesis of fluorescent gold nanoclusters for rapid bio-imaging of cancer cells and small animals. *Rsc Advances* **2015**, *5* (78), 63821-63826.
41. Le Guével, X.; Hötzer, B.; Jung, G.; Hollemeyer, K.; Trouillet, V.; Schneider, M., Formation of Fluorescent Metal (Au, Ag) Nanoclusters Capped in Bovine Serum Albumin Followed by Fluorescence and Spectroscopy. *The Journal of Physical Chemistry C* **2011**, *115* (22), 10955-10963.
42. Volden, S.; Lystvet, S. M.; Halskau, O.; Glomm, W. R., Generally applicable procedure for in situ formation of fluorescent protein-gold nanoconstructs. *RSC Advances* **2012**, *2* (31), 11704-11711.
43. Liu, C.-L.; Wu, H.-T.; Hsiao, Y.-H.; Lai, C.-W.; Shih, C.-W.; Peng, Y.-K.; Tang, K.-C.; Chang, H.-W.; Chien, Y.-C.; Hsiao, J.-K.; Cheng, J.-T.; Chou, P.-T., Insulin-Directed Synthesis of Fluorescent Gold Nanoclusters: Preservation of Insulin Bioactivity and Versatility in Cell Imaging. *Angewandte Chemie International Edition* **2011**, *50* (31), 7056-7060.
44. Wei, H.; Wang, Z.; Yang, L.; Tian, S.; Hou, C.; Lu, Y., Lysozyme-stabilized gold fluorescent cluster: Synthesis and application as Hg²⁺ sensor. *Analyst* **2010**, *135* (6), 1406-1410.
45. Chen, W.-Y.; Lin, J.-Y.; Chen, W.-J.; Luo, L.; Wei-Guang Diao, E.; Chen, Y.-C., Functional gold nanoclusters as antimicrobial agents for antibiotic-resistant bacteria. *Nanomedicine* **2010**, *5* (5), 755-764.
46. Chen, T.-H.; Tseng, W.-L., (Lysozyme Type VI)-Stabilized Au₈ Clusters: Synthesis Mechanism and Application for Sensing of Glutathione in a Single Drop of Blood. *Small* **2012**, *8* (12), 1912-1919.
47. Wang, Y.; Chen, J.-T.; Yan, X.-P., Fabrication of Transferrin Functionalized Gold Nanoclusters/Graphene Oxide Nanocomposite for Turn-On Near-Infrared Fluorescent Bioimaging of Cancer Cells and Small Animals. *Analytical Chemistry* **2013**, *85* (4), 2529-2535.

48. West, A. L.; Griep, M. H.; Cole, D. P.; Karna, S. P., DNase 1 Retains Endodeoxyribonuclease Activity Following Gold Nanocluster Synthesis. *Analytical Chemistry* **2014**, *86* (15), 7377-7382.
49. Kong, Y.; Chen, J.; Gao, F.; Brydson, R.; Johnson, B.; Heath, G.; Zhang, Y.; Wu, L.; Zhou, D., Near-infrared fluorescent ribonuclease-A-encapsulated gold nanoclusters: preparation, characterization, cancer targeting and imaging. *Nanoscale* **2013**, *5* (3), 1009-1017.
50. Kawasaki, H.; Hamaguchi, K.; Osaka, I.; Arakawa, R., ph-Dependent Synthesis of Pepsin-Mediated Gold Nanoclusters with Blue Green and Red Fluorescent Emission. *Advanced Functional Materials* **2011**, *21* (18), 3508-3515.
51. Zhang, X.-D.; Chen, J.; Luo, Z.; Wu, D.; Shen, X.; Song, S.-S.; Sun, Y.-M.; Liu, P.-X.; Zhao, J.; Huo, S.; Fan, S.; Fan, F.; Liang, X.-J.; Xie, J., Enhanced Tumor Accumulation of Sub-2 nm Gold Nanoclusters for Cancer Radiation Therapy. *Advanced Healthcare Materials* **2014**, *3* (1), 133-141.
52. Wei, H.; Wang, Z.; Zhang, J.; House, S.; Gao, Y.-G.; Yang, L.; Robinson, H.; Tan, L. H.; Xing, H.; Hou, C.; Robertson, I. M.; Zuo, J.-M.; Lu, Y., Time-dependent, protein-directed growth of gold nanoparticles within a single crystal of lysozyme. *Nat Nano* **2011**, *6* (2), 93-97.
53. Chaudhari, K.; Xavier, P. L.; Pradeep, T., Understanding the Evolution of Luminescent Gold Quantum Clusters in Protein Templates. *ACS Nano* **2011**, *5* (11), 8816-8827.
54. Wen, F.; Dong, Y.; Feng, L.; Wang, S.; Zhang, S.; Zhang, X., Horseradish Peroxidase Functionalized Fluorescent Gold Nanoclusters for Hydrogen Peroxide Sensing. *Analytical Chemistry* **2011**, *83* (4), 1193-1196.
55. de la Rica, R.; Chow, L. W.; Horejs, C.-M.; Mazo, M.; Chiappini, C.; Pashuck, E. T.; Bitton, R.; Stevens, M. M., A designer peptide as a template for growing Au nanoclusters. *Chemical Communications* **2014**, *50* (73), 10648-10650.
56. Zheng, J.; Petty, J. T.; Dickson, R. M., High Quantum Yield Blue Emission from Water-Soluble Au₈ Nanodots. *Journal of the American Chemical Society* **2003**, *125* (26), 7780-7781.
57. Lee, W. I.; Bae, Y.; Bard, A. J., Strong Blue Photoluminescence and ECL from OH-Terminated PAMAM Dendrimers in the Absence of Gold

Nanoparticles. *Journal of the American Chemical Society* **2004**, *126* (27), 8358-8359.

58. Wang, D.; Imae, T., Fluorescence Emission from Dendrimers and Its pH Dependence. *Journal of the American Chemical Society* **2004**, *126* (41), 13204-13205.

59. Tran, M. L.; Zvyagin, A. V.; Plakhotnik, T., Synthesis and spectroscopic observation of dendrimer-encapsulated gold nanoclusters. *Chemical Communications* **2006**, (22), 2400-2401.

60. Zheng, J.; Zhang, C.; Dickson, R. M., Highly Fluorescent, Water-Soluble, Size-Tunable Gold Quantum Dots. *Physical Review Letters* **2004**, *93* (7), 077402.

61. Zheng, J.; Nicovich, P. R.; Dickson, R. M., Highly Fluorescent Noble-Metal Quantum Dots. *Annual Review of Physical Chemistry* **2007**, *58* (1), 409-431.

62. Bronstein, L. M.; Shifrina, Z. B., Dendrimers as Encapsulating, Stabilizing, or Directing Agents for Inorganic Nanoparticles. *Chemical Reviews* **2011**, *111* (9), 5301-5344.

63. Santiago González, B.; Rodríguez, M. J.; Blanco, C.; Rivas, J.; López-Quintela, M. A.; Martinho, J. M. G., One Step Synthesis of the Smallest Photoluminescent and Paramagnetic PVP-Protected Gold Atomic Clusters. *Nano Letters* **2010**, *10* (10), 4217-4221.

64. Duan, H.; Nie, S., Etching Colloidal Gold Nanocrystals with Hyperbranched and Multivalent Polymers: A New Route to Fluorescent and Water-Soluble Atomic Clusters. *Journal of the American Chemical Society* **2007**, *129* (9), 2412-2413.

65. Schaeffer, N.; Tan, B.; Dickinson, C.; Rosseinsky, M. J.; Laromaine, A.; McComb, D. W.; Stevens, M. M.; Wang, Y.; Petit, L.; Barentin, C.; Spiller, D. G.; Cooper, A. I.; Levy, R., Fluorescent or not? Size-dependent fluorescence switching for polymer-stabilized gold clusters in the 1.1-1.7 nm size range. *Chemical Communications* **2008**, (34), 3986-3988.

66. Hussain, I.; Graham, S.; Wang, Z.; Tan, B.; Sherrington, D. C.; Rannard, S. P.; Cooper, A. I.; Brust, M., Size-Controlled Synthesis of Near-Monodisperse Gold Nanoparticles in the 1–4 nm Range Using Polymeric

Stabilizers. *Journal of the American Chemical Society* **2005**, *127* (47), 16398-16399.

67. Wang, Z.; Tan, B.; Hussain, I.; Schaeffer, N.; Wyatt, M. F.; Brust, M.; Cooper, A. I., Design of Polymeric Stabilizers for Size-Controlled Synthesis of Monodisperse Gold Nanoparticles in Water. *Langmuir* **2007**, *23* (2), 885-895.

68. Guiying, L.; Yong, S.; Fei, W.; Shujuan, X.; Jian, P.; Lingling, L., DNA-hosted fluorescent gold nanoclusters: sequence-dependent formation. *Nanotechnology* **2013**, *24* (1), 015503.

69. Kennedy, T. A. C.; MacLean, J. L.; Liu, J. W., Blue emitting gold nanoclusters templated by poly-cytosine DNA at low pH and poly-adenine DNA at neutral pH. *Chemical Communications* **2012**, *48* (54), 6845-6847.

70. Liu, J., DNA-stabilized, fluorescent, metal nanoclusters for biosensor development. *TrAC Trends in Analytical Chemistry* **2014**, *58*, 99-111.

71. Qu, X.; Li, Y.; Li, L.; Wang, Y.; Liang, J.; Liang, J., Fluorescent Gold Nanoclusters: Synthesis and Recent Biological Application. *Journal of Nanomaterials* **2015**, *2015*, 23.

72. Lopez, A.; Liu, J., DNA-templated fluorescent gold nanoclusters reduced by Good's buffer: from blue-emitting seeds to red and near infrared emitters. *Canadian Journal of Chemistry* **2015**, *93* (6), 615-620.

73. Chakraborty, S.; Babanova, S.; Rocha, R. C.; Desireddy, A.; Artyushkova, K.; Boncella, A. E.; Atanassov, P.; Martinez, J. S., A Hybrid DNA-Templated Gold Nanocluster For Enhanced Enzymatic Reduction of Oxygen. *Journal of the American Chemical Society* **2015**, *137* (36), 11678-11687.

74. Bian, P.; Zhou, J.; Liu, Y.; Ma, Z., One-step fabrication of intense red fluorescent gold nanoclusters and their application in cancer cell imaging. *Nanoscale* **2013**, *5* (13), 6161-6166.

75. Wang, J.; Ye, J.; Jiang, H.; Gao, S.; Ge, W.; Chen, Y.; Liu, C.; Amatore, C.; Wang, X., Simultaneous and multisite tumor rapid-target bioimaging through in vivo biosynthesis of fluorescent gold nanoclusters. *Rsc Advances* **2014**, *4* (71), 37790-37795.

76. Wang, L.; Li, Y.-F.; Zhou, L.; Liu, Y.; Meng, L.; Zhang, K.; Wu, X.; Zhang, L.; Li, B.; Chen, C., Characterization of gold nanorods in vivo by integrated analytical techniques: their uptake, retention, and chemical forms. *Anal Bioanal Chem* **2010**, 396 (3), 1105-1114.
77. Xu, S.; Liu, P.; Song, Q.; Wang, L.; Luo, X., One-pot synthesis of biofunctional and near-infrared fluorescent gold nanodots and their application in Pb²⁺ sensing and tumor cell imaging. *Rsc Advances* **2015**, 5 (5), 3152-3156.
78. Heaven, M. W.; Dass, A.; White, P. S.; Holt, K. M.; Murray, R. W., Crystal Structure of the Gold Nanoparticle [N(C₈H₁₇)₄][Au₂₅(SCH₂CH₂Ph)₁₈]. *Journal of the American Chemical Society* **2008**, 130 (12), 3754-3755.
79. Chen, L.-Y.; Wang, C.-W.; Yuan, Z.; Chang, H.-T., Fluorescent Gold Nanoclusters: Recent Advances in Sensing and Imaging. *Analytical Chemistry* **2015**, 87 (1), 216-229.
80. Pyykko, P., Theoretical chemistry of gold. III. *Chemical Society Reviews* **2008**, 37 (9), 1967-1997.
81. de Heer, W. A., The physics of simple metal clusters: experimental aspects and simple models. *Reviews of Modern Physics* **1993**, 65 (3), 611-676.
82. Wang, G.; Guo, R.; Kalyuzhny, G.; Choi, J.-P.; Murray, R. W., NIR Luminescence Intensities Increase Linearly with Proportion of Polar Thiolate Ligands in Protecting Monolayers of Au₃₈ and Au₁₄₀ Quantum Dots. *The Journal of Physical Chemistry B* **2006**, 110 (41), 20282-20289.
83. Crawford, S. E.; Andolina, C. M.; Smith, A. M.; Marbella, L. E.; Johnston, K. A.; Straney, P. J.; Hartmann, M. J.; Millstone, J. E., Ligand-Mediated "Turn On," High Quantum Yield Near-Infrared Emission in Small Gold Nanoparticles. *Journal of the American Chemical Society* **2015**, 137 (45), 14423-14429.
84. Wang, G.; Huang, T.; Murray, R. W.; Menard, L.; Nuzzo, R. G., Near-IR Luminescence of Monolayer-Protected Metal Clusters. *Journal of the American Chemical Society* **2005**, 127 (3), 812-813.
85. Wu, Z.; Jin, R., On the Ligand's Role in the Fluorescence of Gold Nanoclusters. *Nano Letters* **2010**, 10 (7), 2568-2573.

86. Zhou, C.; Sun, C.; Yu, M.; Qin, Y.; Wang, J.; Kim, M.; Zheng, J., Luminescent Gold Nanoparticles with Mixed Valence States Generated from Dissociation of Polymeric Au(I) Thiolates. *The Journal of Physical Chemistry C* **2010**, *114* (17), 7727-7732.
87. Li, L.; Li, Z.; Zhang, H.; Zhang, S.; Majeed, I.; Tan, B., Effect of polymer ligand structures on fluorescence of gold clusters prepared by photoreduction. *Nanoscale* **2013**, *5* (5), 1986-1992.
88. Devadas, M. S.; Kim, J.; Sinn, E.; Lee, D.; Goodson, T.; Ramakrishna, G., Unique Ultrafast Visible Luminescence in Monolayer-Protected Au₂₅ Clusters. *The Journal of Physical Chemistry C* **2010**, *114* (51), 22417-22423.
89. Wen, X.; Yu, P.; Toh, Y.-R.; Hsu, A.-C.; Lee, Y.-C.; Tang, J., Fluorescence Dynamics in BSA-Protected Au₂₅ Nanoclusters. *The Journal of Physical Chemistry C* **2012**, *116* (35), 19032-19038.
90. Forward, J. M.; Bohmann, D.; Fackler, J. P.; Staples, R. J., Luminescence Studies of Gold(I) Thiolate Complexes. *Inorganic Chemistry* **1995**, *34* (25), 6330-6336.
91. Cha, S.-H.; Kim, J.-U.; Kim, K.-H.; Lee, J.-C., Preparation and Photoluminescent Properties of Gold(I)-Alkanethiolate Complexes Having Highly Ordered Supramolecular Structures. *Chemistry of Materials* **2007**, *19* (25), 6297-6303.
92. Luo, Z.; Yuan, X.; Yu, Y.; Zhang, Q.; Leong, D. T.; Lee, J. Y.; Xie, J., From Aggregation-Induced Emission of Au(I)-Thiolate Complexes to Ultrabright Au(0)@Au(I)-Thiolate Core-Shell Nanoclusters. *Journal of the American Chemical Society* **2012**, *134* (40), 16662-16670.
93. Montalti, M.; Battistelli, G.; Cantelli, A.; Genovese, D., Photo-tunable multicolour fluorescence imaging based on self-assembled fluorogenic nanoparticles. *Chemical Communications* **2014**, *50* (40), 5326-5329.
94. Yau, S. H.; Varnavski, O.; Gilbertson, J. D.; Chandler, B.; Ramakrishna, G.; Goodson, T., Ultrafast Optical Study of Small Gold Monolayer Protected Clusters: A Closer Look at Emission. *The Journal of Physical Chemistry C* **2010**, *114* (38), 15979-15985.
95. Yau, S. H.; Varnavski, O.; Goodson, T., An ultrafast look at Au nanoclusters. *Accounts of Chemical Research* **2013**, *46* (7), 1506-1516.

96. Zheng, J.; Zhou, C.; Yu, M.; Liu, J., Different sized luminescent gold nanoparticles. *Nanoscale* **2012**, *4* (14), 4073-4083.
97. Wen, X.; Yu, P.; Toh, Y.-R.; Tang, J., Structure-Related Dual Fluorescent Bands in BSA-Protected Au₂₅ Nanoclusters. *The Journal of Physical Chemistry C* **2012**, *116* (21), 11830-11836.
98. Taylor, K. J.; Pettiette-Hall, C. L.; Cheshnovsky, O.; Smalley, R. E., Ultraviolet photoelectron spectra of coinage metal clusters. *The Journal of Chemical Physics* **1992**, *96* (4), 3319-3329.
99. Katakuse, I.; Ichihara, T.; Fujita, Y.; Matsuo, T.; Sakurai, T.; Matsuda, H., Mass distributions of copper, silver and gold clusters and electronic shell structure. *International Journal of Mass Spectrometry and Ion Processes* **1985**, *67* (2), 229-236.
100. Tsunoyama, H.; Tsukuda, T., Magic Numbers of Gold Clusters Stabilized by PVP. *Journal of the American Chemical Society* **2009**, *131* (51), 18216-18217.
101. Knight, W. D.; Clemenger, K.; de Heer, W. A.; Saunders, W. A.; Chou, M. Y.; Cohen, M. L., Electronic Shell Structure and Abundances of Sodium Clusters. *Physical Review Letters* **1984**, *52* (24), 2141-2143.
102. Alonso, D. J. A., *Structure and Properties of Atomic Nanoclusters*. 2nd edition ed.; World scientific, Imperial College Press: 2011.
103. Di A. Kiejna, K. F. W., *Metal Surface Electron Physics* Elsevier: 1996.
104. McQuarrie, D. A., *Quantum Chemistry*. Second edition ed.; University Science Books: 2008.
105. Dong, R.; Chen, X.; Zhao, H.; Wang, X.; Shu, H.; Ding, Z.; Wei, L., Towards ultra small noble metal nanoparticles: testing Jellium model for ligand protected copper and silver M13 core nanoparticles. *Physical Chemistry Chemical Physics* **2011**, *13* (8), 3274-3280.
106. Walter, M.; Akola, J.; Lopez-Acevedo, O.; Jadzinsky, P. D.; Calero, G.; Ackerson, C. J.; Whetten, R. L.; Grönbeck, H.; Häkkinen, H., A unified view of ligand-protected gold clusters as superatom complexes. *Proceedings of the National Academy of Sciences* **2008**, *105* (27), 9157-9162.
107. Häkkinen, H., The gold-sulfur interface at the nanoscale. *Nat. Chem.* **2012**, *4* (6), 443-455.

108. Pyykkö, P., Theoretical chemistry of gold. II. *Inorganica Chimica Acta* **2005**, 358 (14), 4113-4130.
109. Pyykkö, P., Theoretical Chemistry of Gold. *Angewandte Chemie International Edition* **2004**, 43 (34), 4412-4456.
110. Häkkinen, H.; Walter, M.; Grönbeck, H., Divide and Protect: Capping Gold Nanoclusters with Molecular Gold–Thiolate Rings. *The Journal of Physical Chemistry B* **2006**, 110 (20), 9927-9931.
111. Martin, M. N.; Li, D.; Dass, A.; Eah, S.-K., Ultrafast, 2 min synthesis of monolayer-protected gold nanoclusters ($d < 2$ nm). *Nanoscale* **2012**, 4 (14), 4091-4094.
112. Shichibu, Y.; Negishi, Y.; Watanabe, T.; Chaki, N. K.; Kawaguchi, H.; Tsukuda, T., Biicosahedral Gold Clusters $[\text{Au}_{25}(\text{PPh}_3)_{10}(\text{SCnH}_{2n+1})_5\text{Cl}_2]^{2+}$ ($n = 2-18$): A Stepping Stone to Cluster-Assembled Materials. *The Journal of Physical Chemistry C* **2007**, 111 (22), 7845-7847.
113. Nishigaki, J.-i.; Yamazoe, S.; Kohara, S.; Fujiwara, A.; Kurashige, W.; Negishi, Y.; Tsukuda, T., A twisted bi-icosahedral Au_{25} cluster enclosed by bulky arenethiolates. *Chemical Communications* **2014**, 50 (7), 839-841.
114. Nobusada, K.; Iwasa, T., Oligomeric Gold Clusters with Vertex-Sharing Bi- and Triicosahedral Structures. *The Journal of Physical Chemistry C* **2007**, 111 (39), 14279-14282.
115. Lin, Z.; Kanters, R. P. F.; Mingos, D. M. P., Closed-shell electronic requirements for condensed clusters of the group 11 elements. *Inorganic Chemistry* **1991**, 30 (1), 91-95.
116. Cheng, L.; Yuan, Y.; Zhang, X.; Yang, J., Superatom Networks in Thiolate-Protected Gold Nanoparticles. *Angewandte Chemie International Edition* **2013**, 52 (34), 9035-9039.
117. Cheng, L.; Yang, J., Communication: New insight into electronic shells of metal clusters: Analogues of simple molecules. *The Journal of Chemical Physics* **2013**, 138 (14), 141101.
118. Cheng, L.; Ren, C.; Zhang, X.; Yang, J., New insight into the electronic shell of $\text{Au}_{38}(\text{SR})_{24}$: a superatomic molecule. *Nanoscale* **2013**, 5 (4), 1475-1478.

119. Qian, H.; Eckenhoff, W. T.; Zhu, Y.; Pintauer, T.; Jin, R., Total Structure Determination of Thiolate-Protected Au₃₈ Nanoparticles. *Journal of the American Chemical Society* **2010**, *132* (24), 8280-8281.
120. Kumara, C.; Gagnon, K. J.; Dass, A., X-ray Crystal Structure of Au_{38-x}Ag_x(SCH₂CH₂Ph)₂₄ Alloy Nanomolecules. *The Journal of Physical Chemistry Letters* **2015**, *6* (7), 1223-1228.
121. Kumar, S.; Jin, R., Water-soluble Au-25(Capt)(18) nanoclusters: synthesis, thermal stability, and optical properties. *Nanoscale* **2012**, *4* (14), 4222-4227.
122. Yan, L.; Cheng, L.; Yang, J., Tetrahedral Au₁₇₊: A Superatomic Molecule with a Au₁₃ FCC Core. *The Journal of Physical Chemistry C* **2015**, *119* (40), 23274-23278.
123. Negishi, Y.; Chaki, N. K.; Shichibu, Y.; Whetten, R. L.; Tsukuda, T., Origin of magic stability of thiolated gold clusters: A case study on Au-25(SC₆H₁₃)(18). *Journal of the American Chemical Society* **2007**, *129* (37), 11322-+.
124. Tian, S.; Li, Y.-Z.; Li, M.-B.; Yuan, J.; Yang, J.; Wu, Z.; Jin, R., Structural isomerism in gold nanoparticles revealed by X-ray crystallography. *Nat Commun* **2015**, *6*.
125. Oh, E.; Fatemi, F. K.; Currie, M.; Delehanty, J. B.; Pons, T.; Fragola, A.; Leveque-Fort, S.; Goswami, R.; Susumu, K.; Huston, A. L.; Medintz, I. L., PEGylated Luminescent Gold Nanoclusters: Synthesis, Characterization, Bioconjugation, and Application to One- and Two-Photon Cellular Imaging. *Particle & Particle Systems Characterization* **2013**, *30* (5), 453-466.
126. Zhang, Z.; Xu, L.; Li, H.; Kong, J., Wavelength-tunable luminescent gold nanoparticles generated by cooperation ligand exchange and their potential application in cellular imaging. *Rsc Advances* **2013**, *3* (1), 59-63.
127. Zhang, C.; Zhou, Z.; Qian, Q.; Gao, G.; Li, C.; Feng, L.; Wang, Q.; Cui, D., Glutathione-capped fluorescent gold nanoclusters for dual-modal fluorescence/X-ray computed tomography imaging. *Journal of Materials Chemistry B* **2013**, *1* (38), 5045-5053.
128. Wang, Y.; Xu, C.; Zhai, J.; Gao, F.; Liu, R.; Gao, L.; Zhao, Y.; Chai, Z.; Gao, X., Label-Free Au Cluster Used for in Vivo 2D and 3D Computed

Tomography of Murine Kidneys. *Analytical Chemistry* **2015**, 87 (1), 343-345.

129. Chen, D.; Luo, Z.; Li, N.; Lee, J. Y.; Xie, J.; Lu, J., Amphiphilic Polymeric Nanocarriers with Luminescent Gold Nanoclusters for Concurrent Bioimaging and Controlled Drug Release. *Advanced Functional Materials* **2013**, 23 (35), 4324-4331.

130. Khlebtsov, B.; Tuchina, E.; Tuchin, V.; Khlebtsov, N., Multifunctional Au nanoclusters for targeted bioimaging and enhanced photodynamic inactivation of *Staphylococcus aureus*. *Rsc Advances* **2015**, 5 (76), 61639-61649.

131. Zhang, P.; Yang, X. X.; Wang, Y.; Zhao, N. W.; Xiong, Z. H.; Huang, C. Z., Rapid synthesis of highly luminescent and stable Au₂₀ nanoclusters for active tumor-targeted imaging in vitro and in vivo. *Nanoscale* **2014**, 6 (4), 2261-2269.

132. Zhou, C.; Long, M.; Qin, Y.; Sun, X.; Zheng, J., Luminescent Gold Nanoparticles with Efficient Renal Clearance. *Angewandte Chemie International Edition* **2011**, 50 (14), 3168-3172.

133. Zhou, C.; Yang, S.; Liu, J.; Yu, M.; Zheng, J., Luminescent gold nanoparticles: A new class of nanoprobe for biomedical imaging. *Experimental Biology and Medicine* **2013**, 238 (11), 1199-1209.

134. Liu, J.; Yu, M.; Zhou, C.; Yang, S.; Ning, X.; Zheng, J., Passive Tumor Targeting of Renal-Clearable Luminescent Gold Nanoparticles: Long Tumor Retention and Fast Normal Tissue Clearance. *Journal of the American Chemical Society* **2013**, 135 (13), 4978-4981.

135. Palafox-Hernandez, J. P.; Lim, C.-K.; Tang, Z.; Drew, K. L. M.; Hughes, Z. E.; Li, Y.; Swihart, M. T.; Prasad, P. N.; Knecht, M. R.; Walsh, T. R., Optical Actuation of Inorganic/Organic Interfaces: Comparing Peptide-Azobenzene Ligand Reconfiguration on Gold and Silver Nanoparticles. *ACS Applied Materials & Interfaces* **2016**, 8 (1), 1050-1060.

136. Song, H.; Jing, C.; Ma, W.; Xie, T.; Long, Y.-T., Reversible photoisomerization of azobenzene molecules on a single gold nanoparticle surface. *Chemical Communications* **2016**, 52 (14), 2984-2987.

137. Yoon, J.-H. Y., Sang-Woon; , Observation of Isomerization of an Azobenzene Derivative

in Gold Nanoparticle Aggregates Using SERS. *Bulletin of the Korean Chemical Society* **30** (12), 2877-2878.

138. Yuan, Q.; Zhang, Y.; Chen, Y.; Wang, R.; Du, C.; Yasun, E.; Tan, W., Using silver nanowire antennas to enhance the conversion efficiency of photoresponsive DNA nanomotors. *Proceedings of the National Academy of Sciences* **2011**, *108* (23), 9331-9336.

139. Hernandez, Y.; Nicolosi, V.; Lotya, M.; Blighe, F. M.; Sun, Z.; De, S.; McGovern, I. T.; Holland, B.; Byrne, M.; Gun'Ko, Y. K.; Boland, J. J.; Niraj, P.; Duesberg, G.; Krishnamurthy, S.; Goodhue, R.; Hutchison, J.; Scardaci, V.; Ferrari, A. C.; Coleman, J. N., High-yield production of graphene by liquid-phase exfoliation of graphite. *Nat Nano* **2008**, *3* (9), 563-568.

140. Perrone, B.; Springhetti, S.; Ramadori, F.; Rastrelli, F.; Mancin, F., "NMR Chemosensing" Using Monolayer-Protected Nanoparticles as Receptors. *Journal of the American Chemical Society* **2013**, *135* (32), 11768-11771.

141. Salvia, M.-V.; Ramadori, F.; Springhetti, S.; Diez-Castellnou, M.; Perrone, B.; Rastrelli, F.; Mancin, F., Nanoparticle-Assisted NMR Detection of Organic Anions: From Chemosensing to Chromatography. *Journal of the American Chemical Society* **2015**, *137* (2), 886-892.

142. Zollinger, H., *Color Chemistry: Syntheses, Properties, and Applications of Organic Dyes and Pigments*. John Wiley & Sons: 2003.

143. Fisher, E., Ferri-oxalate actinometry. *EPA Newsletters* **1984**, *21*, 33-34.

144. L. Moggi, A. J., M. T. Gandolfi, *Manuale del fotochimico. Tecniche e metodologie*. 2006.

145. Chen, A.; Shapiro, M. J., NOE Pumping: A Novel NMR Technique for Identification of Compounds with Binding Affinity to Macromolecules. *Journal of the American Chemical Society* **1998**, *120* (39), 10258-10259.

146. Hostetler, M. J.; Wingate, J. E.; Zhong, C.-J.; Harris, J. E.; Vachet, R. W.; Clark, M. R.; Londono, J. D.; Green, S. J.; Stokes, J. J.; Wignall, G. D.; Glish, G. L.; Porter, M. D.; Evans, N. D.; Murray, R. W., Alkanethiolate Gold Cluster Molecules with Core Diameters from 1.5 to 5.2 nm: Core and Monolayer Properties as a Function of Core Size. *Langmuir* **1998**, *14* (1), 17-30.

147. Liu, X.; Yu, M.; Kim, H.; Mamei, M.; Stellacci, F., Determination of monolayer-protected gold nanoparticle ligand–shell morphology using NMR. *Nat Commun* **2012**, *3*, 1182.
148. (a) Aradhya, S. V.; Venkataraman, L., Single-molecule junctions beyond electronic transport. *Nat. Nanotechnol.* **2013**, *8* (6), 399-410; (b) Wu, Y.; Xie, Y.; Zhang, Q.; Tian, H.; Zhu, W.; Li, A. D. Q., Quantitative Photoswitching in Bis(dithiazole)ethene Enables Modulation of Light for Encoding Optical Signals. *Angewandte Chemie-International Edition* **2014**, *53* (8), 2090-2094.
149. Tian, Z.; Li, A. D. Q., Photoswitching-Enabled Novel Optical Imaging: Innovative Solutions for Real-World Challenges in Fluorescence Detections. *Accounts of Chemical Research* **2013**, *46* (2), 269-279.
150. (a) Lehner, R.; Wang, X.; Wolf, M.; Hunziker, P., Designing switchable nanosystems for medical application. *Journal of Controlled Release* **2012**, *161* (2), 307-316; (b) Stoffelen, C.; Voskuhl, J.; Jonkheijm, P.; Huskens, J., Dual Stimuli- Responsive Self- Assembled Supramolecular Nanoparticles. *Angewandte Chemie-International Edition* **2014**, *53* (13), 3400-3404.
151. (a) Feng, W.; Luo, W.; Feng, Y., Photo-responsive carbon nanomaterials functionalized by azobenzene moieties: structures, properties and application. *Nanoscale* **2012**, *4* (20), 6118-6134; (b) Jochum, F. D.; Theato, P., Temperature- and light-responsive smart polymer materials. *Chemical Society Reviews* **2013**, *42* (17), 7468-7483; (c) Lin, W.-P.; Liu, S.-J.; Gong, T.; Zhao, Q.; Huang, W., Polymer-Based Resistive Memory Materials and Devices. *Advanced Materials* **2014**, *26* (4), 570-606.
152. (a) Joshi, G. K.; Blodgett, K. N.; Muhoberac, B. B.; Johnson, M. A.; Smith, K. A.; Sardar, R., Ultrasensitive Photoreversible Molecular Sensors of Azobenzene-Functionalized Plasmonic Nanoantennas. *Nano Letters* **2014**, *14* (2), 532-540; (b) Hallett-Tapley, G. L.; D'Alfonso, C.; Pacioni, N. L.; McTiernan, C. D.; Gonzalez-Bejar, M.; Lanzalunga, O.; Alarcon, E. I.; Scaiano, J. C., Gold nanoparticle catalysis of the cis-trans isomerization of azobenzene. *Chemical Communications* **2013**, *49* (86), 10073-10075; (c) Valley, D. T.; Onstott, M.; Malyk, S.; Benderskii, A. V., Steric Hindrance of

Photoswitching in Self-Assembled Mono layers of Azobenzene and Alkane Thiols. *Langmuir* **2013**, 29 (37), 11623-11631.

153. Negishi, Y.; Kamimura, U.; Ide, M.; Hirayama, M., A photoresponsive Au-25 nanocluster protected by azobenzene derivative thiolates. *Nanoscale* **2012**, 4 (14), 4263-4268.

154. (a) Zheng, Q.; Juette, M. F.; Jockusch, S.; Wasserman, M. R.; Zhou, Z.; Altman, R. B.; Blanchard, S. C., Ultra-stable organic fluorophores for single-molecule research. *Chem. Soc. Rev.* **2014**, 43 (4), 1044-1056; (b) Stennett, E. M. S.; Ciuba, M. A.; Levitus, M., Photophysical processes in single molecule organic fluorescent probes. *Chem. Soc. Rev.* **2014**, 43 (4), 1057-1075; (c) Bonacchi, S.; Rampazzo, E.; Montalti, M.; Prodi, L.; Zaccheroni, N.; Mancin, F.; Teolato, P., Amplified fluorescence response of chemosensors grafted onto silica nanoparticles. *Langmuir* **2008**, 24 (15), 8387-8392; (d) Genovese, D.; Bonacchi, S.; Juris, R.; Montalti, M.; Prodi, L.; Rampazzo, E.; Zaccheroni, N., Prevention of Self-Quenching in Fluorescent Silica Nanoparticles by Efficient Energy Transfer. *Angewandte Chemie-International Edition* **2013**, 52 (23), 5965-5968; (e) Montalti, M.; Dolci, L. S.; Prodi, L.; Zaccheroni, N.; Stuart, M. C. A.; van Bommel, K. J. C.; Friggeri, A., Energy transfer from a fluorescent hydrogel to a hosted fluorophore. *Langmuir* **2006**, 22 (5), 2299-2303; (f) Rampazzo, E.; Bonacchi, S.; Juris, R.; Montalti, M.; Genovese, D.; Zaccheroni, N.; Prodi, L.; Rambaldi, D. C.; Zattoni, A.; Reschiglian, P., Energy Transfer from Silica Core-Surfactant Shell Nanoparticles to Hosted Molecular Fluorophores. *J. Phys. Chem. B* **2010**, 114 (45), 14605-14613.

155. Shichibu, Y.; Negishi, Y.; Tsunoyama, H.; Kanehara, M.; Teranishi, T.; Tsukuda, T., Extremely high stability of glutathionate-protected Au-25 clusters against core etching. *Small* **2007**, 3 (5), 835-839.

156. (a) Rampazzo, E.; Voltan, R.; Petrizza, L.; Zaccheroni, N.; Prodi, L.; Casciano, F.; Zauli, G.; Secchiero, P., Proper design of silica nanoparticles combines high brightness, lack of cytotoxicity and efficient cell endocytosis. *Nanoscale* **2013**, 5 (17), 7897-7905; (b) Helle, M.; Rampazzo, E.; Monchanin, M.; Marchal, F.; Guillemain, F.; Bonacchi, S.; Salis, F.; Prodi, L.; Bezdetsnaya, L., Surface Chemistry Architecture of Silica Nanoparticles

Determine the Efficiency of in Vivo Fluorescence Lymph Node Mapping. *Acs Nano* **2013**, 7 (10), 8645-8657.

157. Soster, M.; Juris, R.; Bonacchi, S.; Genovese, D.; Montalti, M.; Rampazzo, E.; Zaccheroni, N.; Garagnani, P.; Bussolino, F.; Prodi, L.; Marchio, S., Targeted dual-color silica nanoparticles provide univocal identification of micrometastases in preclinical models of colorectal cancer. *International Journal of Nanomedicine* **2012**, 7, 4797-807.

158. Biffi, S.; Petrizza, L.; Rampazzo, E.; Voltan, R.; Sgarzi, M.; Garrovo, C.; Prodi, L.; Andolfi, L.; Agnoletto, C.; Zauli, G.; Secchiero, P., Multiple dyedoped NIR-emitting silica nanoparticles for both flow cytometry and in vivo imaging. *RSC Advances* **2014**, 4 (35), 18278-18285.

159. Rampazzo, E.; Boschi, F.; Bonacchi, S.; Juris, R.; Montalti, M.; Zaccheroni, N.; Prodi, L.; Calderan, L.; Rossi, B.; Becchi, S.; Sbarbati, A., Multicolor core/shell silica nanoparticles for in vivo and ex vivo imaging. *Nanoscale* **2012**, 4 (3), 824-830.

160. Shibu, E. S.; Muhammed, M. A. H.; Tsukuda, T.; Pradeep, T., Ligand Exchange of Au₂₅SG18 Leading to Functionalized Gold Clusters: Spectroscopy, Kinetics, and Luminescence. *The Journal of Physical Chemistry C* **2008**, 112 (32), 12168-12176.

161. Muhammed, M. A. H.; Shaw, A. K.; Pal, S. K.; Pradeep, T., Quantum Clusters of Gold Exhibiting FRET. *The Journal of Physical Chemistry C* **2008**, 112 (37), 14324-14330.

162. Liu, Y.; Tsunoyama, H.; Akita, T.; Xie, S.; Tsukuda, T., Aerobic Oxidation of Cyclohexane Catalyzed by Size-Controlled Au Clusters on Hydroxyapatite: Size Effect in the Sub-2 nm Regime. *ACS Catalysis* **2011**, 1 (1), 2-6.

163. Han, Y.; He, D. S.; Liu, Y.; Xie, S.; Tsukuda, T.; Li, Z. Y., Size and Shape of Nanoclusters: Single-Shot Imaging Approach. *Small (Weinheim an Der Bergstrasse, Germany)* **2012**, 8 (15), 2361-2364.

164. Guevel, X. L.; Tagit, O.; Rodriguez, C. E.; Trouillet, V.; Pernia Leal, M.; Hildebrandt, N., Ligand effect on the size, valence state and red/near infrared photoluminescence of bidentate thiol gold nanoclusters. *Nanoscale* **2014**, 6 (14), 8091-8099.

165. Manea, F.; Bindoli, C.; Polizzi, S.; Lay, L.; Scrimin, P., Expeditious Synthesis of Water-Soluble, Monolayer-Protected Gold Nanoparticles of Controlled Size and Monolayer Composition. *Langmuir* **2008**, *24* (8), 4120-4124.

List of Publications

- *Chem. Commun.* 2014,50, 5326-5329.
- *WIREs Nanomed Nanobiotechnol.* 2016, 8, 139–150.
- *CHEM. SOC. REV.* 2015,44, 4853-4921.
- *Nanoscale.* 2016, DOI: 10.1039/C6NR02193J.